APPLIED COMPUTATIONAL ELECTROMAGNETICS SOCIETY JOURNAL

July 2023
Vol. 38 No. 7
ISSN 1054-4887

The ACES Journal is abstracted in INSPEC, in Engineering Index, DTIC, Science Citation Index Expanded, the Research Alert, and to Current Contents/Engineering, Computing & Technology.

The illustrations on the front cover have been obtained from the ARC research group at the Department of Electrical Engineering, Colorado School of Mines

Published, sold and distributed by: River Publishers, Alsbjergvej 10, 9260 Gistrup, Denmark

THE APPLIED COMPUTATIONAL ELECTROMAGNETICS SOCIETY
http://aces-society.org

EDITORS-IN-CHIEF

Atef Elsherbeni
Colorado School of Mines, EE Dept.
Golden, CO 80401, USA

Sami Barmada
University of Pisa, ESE Dept.
56122 Pisa, Italy

ASSOCIATE EDITORS

Maokun Li
Tsinghua University
Beijing 100084, China

Mauro Parise
University Campus Bio-Medico of Rome
00128 Rome, Italy

Yingsong Li
Harbin Engineering University
Harbin 150001, China

Riyadh Mansoor
Al-Muthanna University
Samawa, Al-Muthanna, Iraq

Lijun Jiang
University of Hong Kong, EEE Dept.
Hong, Kong

Shinishiro Ohnuki
Nihon University
Tokyo, Japan

Kubilay Sertel
The Ohio State University
Columbus, OH 43210, USA

Giulio Antonini
University of L Aquila
67040 L Aquila, Italy

Antonio Musolino
University of Pisa
56126 Pisa, Italy

Abdul A. Arkadan
Colorado School of Mines, EE Dept.
Golden, CO 80401, USA

Salvatore Campione
Sandia National Laboratories
Albuquerque, NM 87185, USA

Ibrahim Mahariq
American University of the Middle East
Kuwait and University of
Turkish Aeronautical Association
Turkey

Wei-Chung Weng
National Chi Nan University, EE Dept.
Puli, Nantou 54561, Taiwan

Alessandro Formisano
Seconda Universita di Napoli
81031 CE, Italy

Piotr Gas
AGH University of Science and Technology
30-059 Krakow, Poland

Long Li
Xidian University
Shaanxa, 710071, China

Steve J. Weiss
US Army Research Laboratoy
Adelphi Laboratory Center (RDRL-SER-M)
Adelphi, MD 20783, USA

Jiming Song
Iowa State University, ECE Dept.
Ames, IA 50011, USA

Toni Bjorninen
Tampere University
Tampere, 33100, Finland

Santanu Kumar Behera
National Institute of Technology
Rourkela-769008, India

Daniele Romano
University of L Aquila
67100 L Aquila, Italy

Alireza Baghai-Wadji
University of Cape Town
Cape Town, 7701, South Africa

Marco Arjona López
La Laguna Institute of Technology
Torreon, Coahuila 27266, Mexico

Kaikai Xu
University of Electronic Science
and Technology of China
China

Paolo Mezzanotte
University of Perugia
I-06125 Perugia, Italy

Luca Di Rienzo
Politecnico di Milano
20133 Milano, Italy

Lei Zhao
Jiangsu Normal University
Jiangsu 221116, China

Sima Noghanian
Commscope
Sunnyvale, CA 94089, USA

Nunzia Fontana
University of Pisa
56122 Pisa, Italy

Stefano Selleri
DINFO - University of Florence
50139 Florence, Italy

Yu Mao Wu
Fudan University
Shanghai 200433, China

Fatih Kaburcuk
Sivas Cumhuriyet University
Sivas 58140, Turkey

Huseyin Savci
Istanbul Medipol University
34810 Beykoz, Istanbul

Zhixiang Huang
Anhui University
China

Amin Kargar Behbahani
Florida International University
Miami, FL 33174, USA

Laila Marzall
University of Colorado, Boulder
Boulder, CO 80309, USA

EDITORIAL ASSISTANTS

Matthew J. Inman
University of Mississippi, EE Dept.
University, MS 38677, USA

Shanell Lopez
Colorado School of Mines, EE Dept.
Golden, CO 80401, USA

EMERITUS EDITORS-IN-CHIEF

Duncan C. Baker
EE Dept. U. of Pretoria
0002 Pretoria, South Africa

Allen Glisson
University of Mississippi, EE Dept.
University, MS 38677, USA

Ahmed Kishk
Concordia University, ECS Dept.
Montreal, QC H3G 1M8, Canada

Robert M. Bevensee
Box 812
Alamo, CA 94507-0516

Ozlem Kilic
Catholic University of America
Washington, DC 20064, USA

David E. Stein
USAF Scientific Advisory Board
Washington, DC 20330, USA

EMERITUS ASSOCIATE EDITORS

Yasushi Kanai
Niigata Inst. of Technology
Kashiwazaki, Japan

Mohamed Abouzahra
MIT Lincoln Laboratory
Lexington, MA, USA

Alexander Yakovlev
University of Mississippi, EE Dept.
University, MS 38677, USA

Levent Gurel
Bilkent University
Ankara, Turkey

Sami Barmada
University of Pisa, ESE Dept.
56122 Pisa, Italy

Ozlem Kilic
Catholic University of America
Washington, DC 20064, USA

Erdem Topsakal
Mississippi State University, EE Dept.
Mississippi State, MS 39762, USA

Alistair Duffy
De Montfort University
Leicester, UK

Fan Yang
Tsinghua University, EE Dept.
Beijing 100084, China

Rocco Rizzo
University of Pisa
56123 Pisa, Italy

Atif Shamim
King Abdullah University of Science and
Technology (KAUST)
Thuwal 23955, Saudi Arabia

William O'Keefe Coburn
US Army Research Laboratory
Adelphi, MD 20783, USA

Mohammed Hadi
Kuwait University, EE Dept.
Safat, Kuwait

Amedeo Capozzoli
Univerita di Naoli Federico II, DIETI
I-80125 Napoli, Italy

Wenxing Li
Harbin Engineering University
Harbin 150001, China

Qiang Ren
Beihang University
Beijing 100191, China

EMERITUS EDITORIAL ASSISTANTS

Khaleb ElMaghoub
Trimble Navigation/MIT
Boston, MA 02125, USA

Kyle Patel
Colorado School of Mines, EE Dept.
Golden, CO 80401, USA

Christina Bonnigton
University of Mississippi, EE Dept.
University, MS 38677, USA

Anne Graham
University of Mississippi, EE Dept.
University, MS 38677, USA

Madison Lee
Colorado School of Mines, EE Dept.
Golen, CO 80401, USA

Allison Tanner
Colorado School of Mines, EE Dept.
Golden, CO 80401, USA

Mohamed Al Sharkawy
Arab Academy for Science and Technology, ECE Dept.
Alexandria, Egypt

JULY 2023 REVIEWERS

Behrokh Beiranvand
Bhattacharya
Merit Cisneros-Gonzalez
Arkaprovo Das
Piotr Gas
Michał Herbko
Taha Imeci
Amir Jafargholi
Mikko Kokkonen
Brian LaRocca
Guanghui Liu
Enrique Melgoza
Durga Prasad Mishra
Mahdi Oliaei
Shi Pu
Jalil Rashed
Kannadhasan S.
Manthan Shah
Tianhong Tan
Marsellas Waller
Steven Weiss
Qun Wu
Kaikai Xu
Salah I. Yahya
Mostafa Yargholi

THE APPLIED COMPUTATIONAL ELECTROMAGNETICS SOCIETY JOURNAL

Vol. 38 No. 7 July 2023

TABLE OF CONTENTS

Investigation and Analysis of Electromagnetic Interference for PWM Encoder of Urban Rail Train
Yang Yang, Feng Zhu, Yuxuan Wang, and Chengpan Yang 466

Failure Mechanism Analysis of the Stochastic Galerkin Method in EMC Simulation Considering Geometric Randomness
Jinjun Bai, Bing Hu, and Yixuan Wan 475

Antenna Synthesis by Levin's Method using Reproducing Kernel Functions
Goker Sener 482

Analysis and Design of Broadband OAM Array Antenna
Yunqi Zhang, Shiliu Zhao, Xuping Li, and Leying Wang 489

A Miniaturized UWB Bandpass Filter Employing Multi-Stub-Loaded Short-Circuited Stepped Impedance Ring Resonator
Guangyong Wei, Yunxiu Wang, Jie Liu, and Haiping Li 496

Edge Hole Effect on Isolation of UWB MIMO RDRA for 5G Outdoor Applications
Tamer G. Abouelnaga and Esmat A. Abdallah 503

Nanoarray of Vivaldi Rectenna for Infrared-energy Harvesting
Wided Amara, Abdelaziz Alzahrani, Ameni Mersani, Donia Oueslati,
Ahmed Elsharabasy, Bandar Hakim, Hatem Rmili, and Atef Elsherbeni 513

THz Microstrip Antenna for Terabit Wireless Local Area Networks
V. Koushick, C. Divya, M. Vinoth, E. A. Mohamed Ali, and M. Sugadev 522

Balanced Filtering Power Divider based on Odd-mode Hybrid Microstrip and Slotline Spoof Surface Plasmon Polaritons
Yi Song and Anxue Zhang 532

Residual Flux Measurement of Single-phase Transformers based on Equivalent Resistance
Qingkun Wang, Yuzhan Ren, Youhua Wang, Chengcheng Liu, and Shipu Wu 539

© 2023, The Applied Computational Electromagnetics Society

Investigation and Analysis of Electromagnetic Interference for PWM Encoder of Urban Rail Train

Yang Yang[1,2], Feng Zhu[1*], Yuxuan Wang[1], and Chengpan Yang[1]

[1]School of Electrical Engineering
Southwest Jiaotong University, Chengdu, 610031, China
280899254@qq.com, zhufeng@swjtu.edu.cn, 864940620@qq.com, yangcook@foxmail.com

[2]Department of Mechanical and Information Engineering
Sichuan College of Architectural Technology, Deyang, 618000, China

***Abstract* –** Electromagnetic compatibility (EMC) is an important factor in ensuring the safe operation of the sensitive electronic equipment on urban rail trains. The pulse width modulation (PWM) encoder of an urban rail train exported from China to Brazil is sometimes affected by electromagnetic interference (EMI), which causes the train to fail to run properly. To solve this problem, the EMC test is performed on the PWM encoder to identify the coupling path and the type of interference source. The EMI coupling model and the vehicle-catenary-rail model are established by using an electromagnetic transients program (EMTP) to analyze the mechanism of interference coupling. It is shown that the unbalanced voltage of the train body caused by the backflow of the grounding current is the root cause of the interference of the PWM encoder. The maximum voltage coupled to the internal port of the PWM encoder is about 1894 V, which is sufficient to burn out the encoder. A measure to suppress the interference by installing thyristor surge suppressors (TSS) P0300SC is proposed, which effectively solves the EMI problem of the PWM encoder.

***Index Terms* –** Coupling path, electromagnetic interference (EMI), EMI suppression, pulse width modulation (PWM) encoder, urban rail train.

I. INTRODUCTION

With the advancement of rail transit, the electromagnetic environment is becoming increasingly intricate, and the variety of on-board electronic equipment has expanded significantly. As a crucial component of the train, the dependable operation of on-board control and communication devices such as pulse width modulation (PWM) encoders are paramount to ensuring safe and reliable operation [1, 2].

The PWM encoder is used to control traction and braking of the train, and its internal circuit is shown in Fig. 1 [3]. The optical coupler converts the analog signal, which is input from the driver's control handle into high and low levels accurately. When the optical coupler output is high , the metal-oxide-semiconductor field-effect transistors (MOSFETs) T_1 and T_3 are in a conducting state, so the PWM encoder outputs a low level. Conversely, when the optical coupler output is low, T_1 and T_3 cut off and the encoder outputs a high level. The optical coupler controls the conduction and cut-off time of each MOSFET, generating pulse signals with different duty ratios ranging from 10% to 90%. These signals are then fed into the control unit to achieve traction and braking of the train. Due to the differences in train grounding methods and in circuit structures and rail quality in different countries, import/export trains, particularly on-board equipment such as PWM encoders, may be affected by electromagnetic interference (EMI). Therefore, it is of great significance to investigate the EMI caused by changes in train operating environments and to study the solutions.

Currently, some experiences and achievements have been accumulated in the investigation and solution of EMI for train on-board equipment. The authors in [2, 4] analyzed the failure of the speed sensor caused by the overvoltage of the train body and the pantograph-catenary contact-loss arc. They proposed measures to address this issue by changing the grounding system. Moreover, when the pantograph was raised or lowered, the on-board balise transmission module (BTM) is subjected to EMI from the arc, resulting in traction blockade. This fault was resolved by improving the BTM's immunity as described in [5], and further research on the BTM's electromagnetic sensitivity is presented in [6]. Reference [7, 8] proposed optimizing wiring and applying cascode level shifter to solve EMI problems related to abnormal LCD displays in the passenger information system. However, there is a lack of research on the EMC of train PWM encoders.

Submitted On: July 4, 2022
Accepted On: September 22, 2023

https://doi.org/10.13052/2023.ACES.J.380701

1054-4887 © ACES

The train EMC problem is mainly related to the railway pantograph-catenary system and grounding system. In terms of research on the interference source model, Guardado et al. [9] improved two black boxes of pantograph-catenary arc models: the Cassie model [10] and the Mayr model [11]. Wei et al. [12] established a grounding reflux model for high-speed electric multiple units (EMUs) with scattered protection grounding, aiming to reduce the voltage of train body and the grounding current. In [13, 14], the vehicle-catenary and vehicle-catenary-viaduct models were respectively built to investigate the train body overvoltage in case of EMU passing neutral section device. The above scholars mainly studied the pantograph-catenary system and the grounding system of high-speed EMU, but there is a lack of research on the EMC of urban rail trains.

There is a problem of PWM encoder burnout during operation in urban rail trains exported from China to Brazil, which have a power supply of 2400 kW and run on DC 3000 V. The specific components that have burned out include resistors R_{e5} and R_{e6}, as well as MOSFETs T_2 and T_3, which are shown in Fig. 1. At present, the interference source, coupling path, coupling mechanism, and solution to this problem have not been studied. In order to solve these problems, we carry out EMC tests and propose a vehicle-catenary-rail coupling model based on EMTP to study the EMI of the PWM encoder.

The remainder of the paper is organized as follows. Section II investigates the interference coupling path of the PWM encoder and the types of interference sources through the EMC test. The coupling model is established in Section III to analyze the interference coupling mechanism. The coupling model is verified, and EMI suppression measures are proposed from the perspective of protecting sensitive equipment in Section IV. Section V is the conclusion.

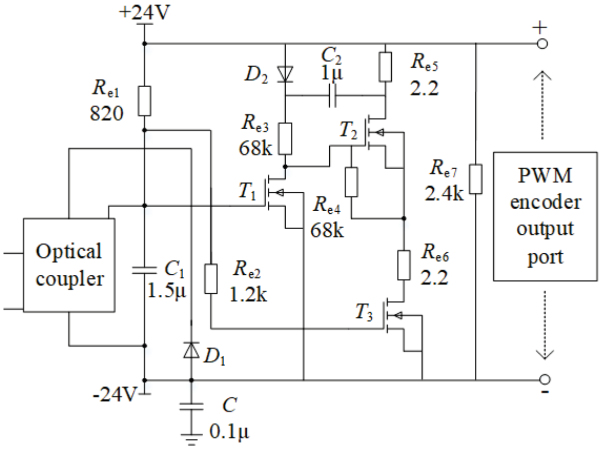

Fig. 1. Internal circuit of PWM encoder.

II. INVESTIGATION OF COUPLING PATH AND INTERFERENCE SOURCE

The three elements of electromagnetic interference include interference source, coupling path, and sensitive equipment. In this section, according to the standard IEC 62236 [15], radiated immunity tests, electrostatic discharge (ESD) immunity tests, electrical fast transient/burst (EFT) immunity tests, and surge (SUG) immunity test are carried out to investigate interference sources and coupling paths of the PWM encoder, which is the sensitive equipment.

A. Investigation of coupling path

Electromagnetic coupling can be classified into two types: radiation coupling and conduction coupling. The radiated immunity test is carried out on the PWM encoder as shown in Fig. 2. The radio frequency signal transmitter (HP-8648C) and the log-periodic antenna (DS-3200) are utilized to simulate potential radiation interference sources such as the pantograph-catenary arc on trains mentioned previously.

In this test, vertical and horizontal polarization radiation is carried out on six surfaces of the PWM encoder, respectively. The results are shown in Table 1. It is evident that the encoder can work normally after being exposed to radiation on all six surfaces within the experimental frequency range of 80 MHz-1 GHz with an electric field intensity of 20 V/m and a frequency range of 1.4 GHz-2 GHz with an electric field intensity of 10 V/m.

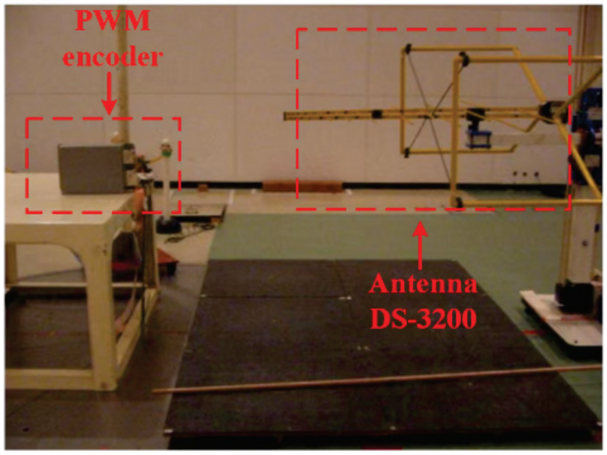

Fig. 2. Radiated immunity test on PWM encoder.

Table 1: Radiated immunity results of PWM encoder

Frequency	Electric Field Intensity	Test Times	Results
80 MHz-1 GHz	20 V/m	20	Normal
1.4 GHz-2 GHz	10 V/m	20	Normal

Moreover, the PWM encoder on the train is tested with the handheld field intensity meter (TES-593) at the work site. The data showed that the maximum electric field intensity in the working environment does not exceed 5 V/m, which indicates that radiation coupling is not responsible for the burnout of the PWM encoder, and therefore the coupling path is conduction coupling.

B. Investigation of interference source type

Conduction coupling tests, including ESD, EFT, and SUG immunity tests, are carried out on the PWM encoder to determine the source of interference.

(1) ESD test

As illustrated in Fig. 3, an ESD generator (ESD61002AG) is selected as the test equipment.

The results of the ESD test are presented in Table 2, showing that the encoder can still work normally after being subjected to 20 direct and indirect discharges at the voltage level of ±4 kV.

(2) EFT test

As illustrated in Fig. 4, the EFT generator (EFT61004BG) is selected as the test equipment.

The results of the EFT test are presented in Table 3, showing that the PWM encoder can still work normally after 20 tests on the power port and signal port of the encoder under a voltage level of ±2 kV.

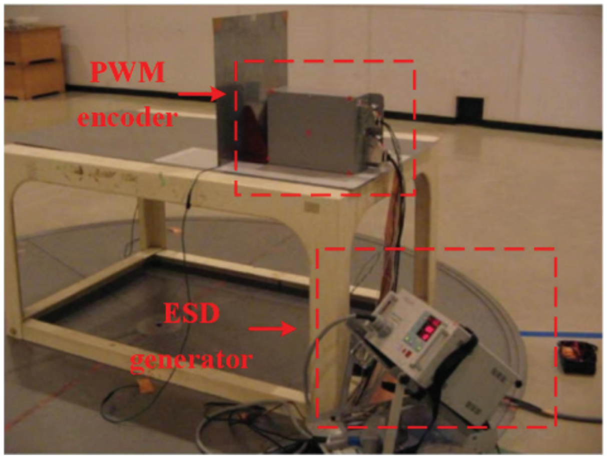

Fig. 3. ESD immunity test of PWM encoder.

Table 2: ESD immunity results of PWM encoder

Types	Voltage Level	Test Times	Results
Direct discharge	±4 kV	20	Normal
Indirect discharge	±4 kV	20	Normal

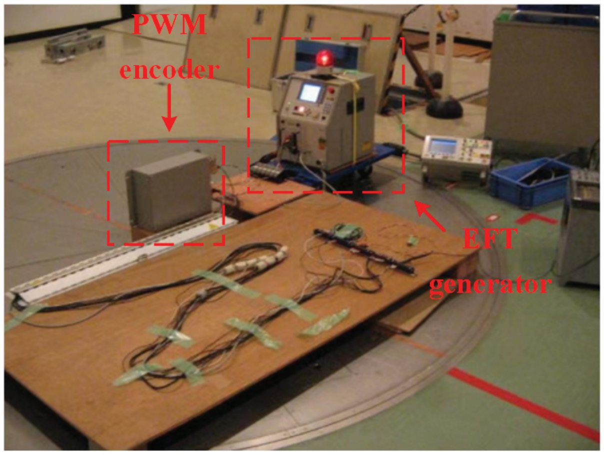

Fig. 4. EFT immunity test of PWM encoder.

Table 3: PWM encoder EFT immunity results

Location	Voltage Level	Test Times	Results
Power port	±2 kV	20	Normal
Signal port	±2 kV	20	Normal

(3) SUG test

As illustrated in Fig. 5, the SUG generator (SUG61005AG) is selected as the test equipment.

The results of the SUG test are shown in Table 4. The PWM encoder can still work normally after 20 tests on its power port at a voltage level of ±2 kV; however, it burned out when the voltage applied to its internal circuit port reached 1.8 kV or higher.

From the test results, it can be determined that the EMI is not caused by ESD or EFT. The interference

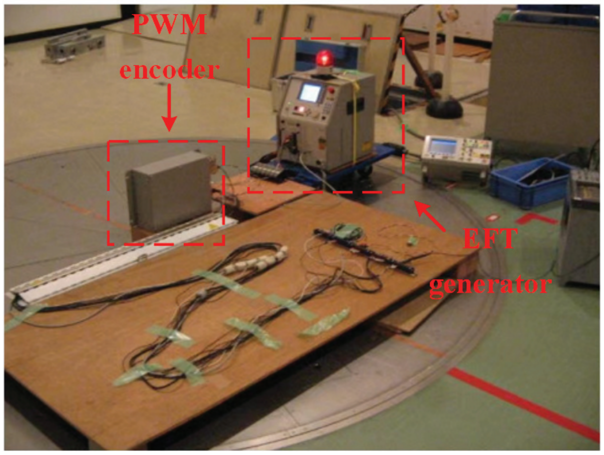

Fig. 5. SUG immunity test of PWM encoder.

Table 4: PWM encoder SUG immunity results

Location	Voltage Level	Test Times	Results
Power port	±2 kV	20	Normal
Internal circuit port	±2 kV	20	Burned
	±1.9 kV	20	Burned
	±1.8 kV	20	Burned
	±1.7 kV	20	Normal

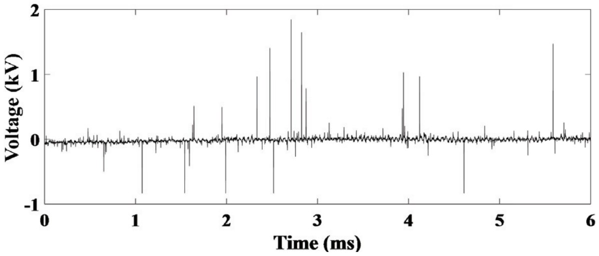

Fig. 6. The voltage of encoder output port tested by oscilloscope.

source is identified as the SUG voltage from the internal circuit port of the PWM encoder. In addition, an oscilloscope is used to test the output port of the PWM encoder at the operation site of the urban train, as shown in Fig. 6. The actual transient voltage peak value is measured up to 1843 V, which verifies the rationality of the above EMC tests.

III. COUPLING MECHANISM OF EMI

A. Coupling model of EMI

By performing on-site investigations of the urban train operations in Rio de Janeiro, Brazil, it is found that the majority of the train's grounding wires are overloaded with current and have become blackened due to the overcurrent. In serious cases, some grounding wires have even been burned off. In addition, the rails are found to be in poor condition, having suffered from severe rusting caused by corrosion from the sea breeze. Even some of the electric connecting wires between the rails are missing, causing the grounding current to fail to return to the traction substation properly. The current acquisition device is used for field testing of the current in each grounding wire of the train. The transient current of the grounding wire is illustrated in Fig. 7, where a positive amplitude indicates that the transient current is flowing into the train body and a negative amplitude indicates that it is flowing out.

The inflow of transient grounding current into the train body can lead to an excess potential difference in the rails under the train, and can also lead to an unbalanced voltage in the train body due to its own impedance, thereby affecting the onboard electrical equipment. The interconnect cable of the PWM encoder is a two-core symmetric shielded cable whose shielding layer is grounded, that is, connected to the train body. When the unbalanced voltage of the train body is applied to both ends of the shielding layer, it capacitively couples to the inner core wires of the shielded cable and creates a potential difference. This interference voltage is then connected to the internal circuit of the PWM encoder, as demonstrated in Fig. 8. C_{10} and C_{20} are the equivalent capacitances between the shielding layer and the two inner core wires, and C_{12} is the equivalent capacitance between the two inner core wires [16]. R_{e6}, R_{e7}, C, and T_3 are the internal components of the PWM encoder in Fig. 1, U_c is the unbalanced voltage at the two ends of the shielding layer, and U_{12} is the interference voltage coupled to the output end of the encoder.

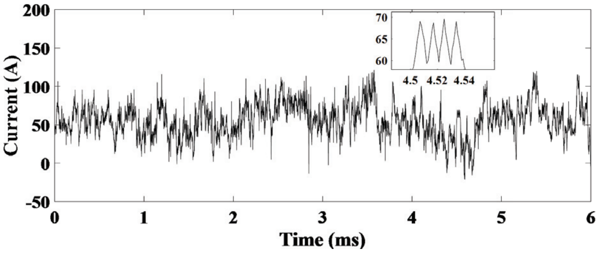

Fig. 7. The transient current of grounding wire.

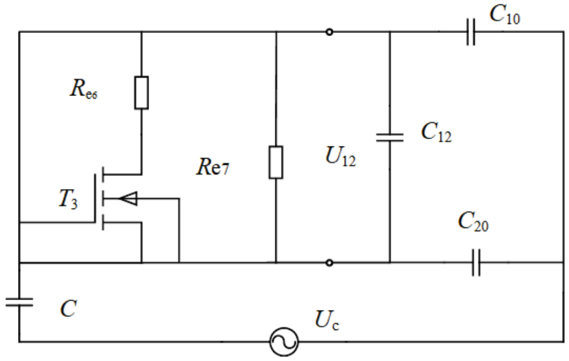

Fig. 8. Capacitive coupling model.

B. Calculation of parameters

In order to obtain U_c and U_{12}, it is necessary to calculate the related parameters of rail and train body.

(1) Rail resistance and inductance

It can be seen from the partially enlarged area of Fig. 7 that the transient current here presents a periodic change with a cycle time of 0.01 ms, so the frequency f of the transient current is approximately 100 kHz. At this frequency, the amplitude of the current density in the current-carrying conductor will be attenuated, and the current mainly exists in the thin layer on the surface of the con-

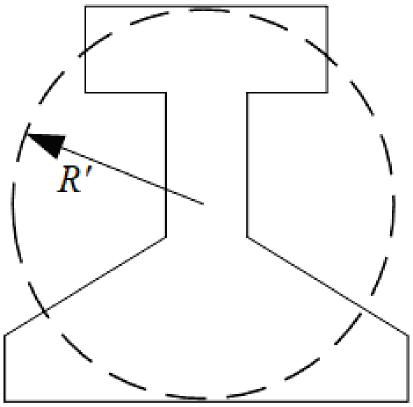

Fig. 9. Equivalent section of the rail.

ductor, which is called the skin effect. Specifically,

$$\delta_1 = \sqrt{1/\pi f \mu_0 \mu_r \gamma_1}, \tag{1}$$

where δ_1 is the effect depth, γ_1 is the conductivity of the rail, μ_0 and μ_r represent vacuum permeability and rail permeability, respectively.

The equivalent section of the rail is shown in Fig. 9 [17], where *R'* is the equivalent radius of the rail.

Accounting for skin effect, the rail AC resistance can be mathematically expressed as

$$R_G = \frac{R'}{[R'^2-(R'-\delta_1)^2]} R_g, \tag{2}$$

$$R_g = 1/(\gamma_1 \pi R'^2), \tag{3}$$

where R_G is the rail AC resistance considering skin effect, R_g is the rail DC resistance.

The magnetic flux is divided into inner and outer magnetic flux. When the current is uniformly distributed within the rail conductor, the flux linkage Ψ_i between the current-carrying conductor and the inner magnetic flux is:

$$\Psi_i = \mu_0 I / 8\pi, \tag{4}$$

where I is the current flowing through the conductor.

However, in the case of a high frequency of 100 kHz, (4) needs to be modified due to the existence of the skin effect. The current density $J(r)$ at the rail radius r can be written as

$$J(r) = J_0 \exp[-(R'-r)/\delta_1], \tag{5}$$

where J_0 is the rail surface current density.

The total current flowing through the rail is

$$I = \int_0^{R'} J(r) 2\pi r dr. \tag{6}$$

The current I' contained at the rail radius r is:

$$I' = \int_0^{r} J(r) 2\pi r dr. \tag{7}$$

Flux linkage Ψ_i between I and the inner magnetic flux can be deduced as

$$\Psi_i = \int_0^{R'} d\psi_i = \int_0^{R'} \frac{I'}{I} B dr. \tag{8}$$

The internal self-inductance of the rail is

$$L_{i1} = \frac{\Psi_i}{I} = \frac{\mu_0 \mu_r \int_0^{R'} 1/rk^2 dr}{2\pi k^2}, \tag{9}$$

where the coefficient k is

$$k = \int_0^{r} \exp[-(R'-r)\sqrt{\pi f \mu_0 \mu_r \gamma_1}] r dr. \tag{10}$$

The calculation diagram of flux linkage between outer magnetic flux and current of rail is shown in Fig. 10. The distance between the rail and the catenary denotes D, and the flux linkage Ψ_o between outer magnetic flux and current is

$$\Psi_o = \int d\phi m = \frac{\mu_0 I}{\pi} \ln \frac{D-R'}{R'}. \tag{11}$$

The rail outer self-inductance L_{o1} is as follows:

$$L_{o1} = \Psi_o / I. \tag{12}$$

(2) Train body inductance

To calculate the train body inductance, the catenary and the train body can be approximately equivalent to a cylinder and a hollow cylinder with thickness d_0, respectively, as shown in Fig. 11 [18]. Here, d_0 is the difference between the inner radius r_2 and the outer radius r_3 of the equivalent train body; r_1 is the equivalent radius of the catenary; and d is the distance between the catenary and the train.

In practice, the train body can be approximated as a cuboid with width b and height h, and its per unit length mass and density are m and ρ, respectively. The relationship between these parameters is expressed as follows:

$$r_2 = (b+h)/\pi, \tag{13}$$

$$r_3 = \sqrt{(b+h)^2/\pi^2 - m/\pi\rho}, \tag{14}$$

$$d_0 = r_3 - r_2. \tag{15}$$

According to relevant self-inductance knowledge and skin effect [19, 20], the train body current will

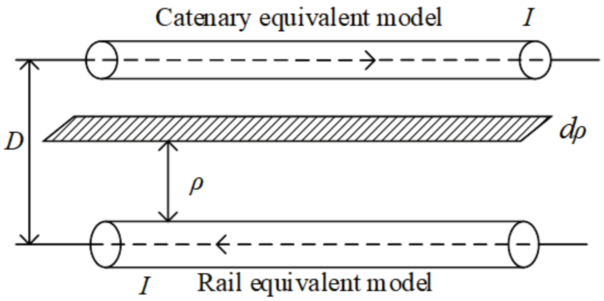

Fig. 10. Schematic diagram of flux linkage calculation.

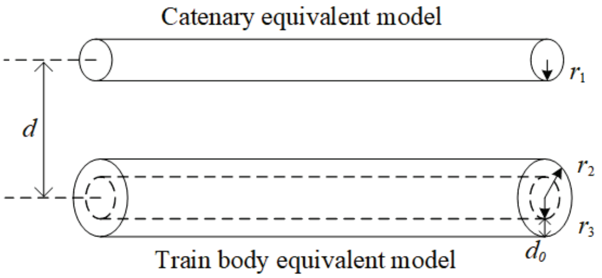

Fig. 11. Train body-catenary equivalent model.

mainly be distributed to the effect depth δ_2:

$$\delta_2 = \sqrt{1/\pi f \mu \gamma_2}, \tag{16}$$

where μ represents the permeability of train body and γ_2 denotes its conductivity.

By calculating the inner self-inductance L_{i2} and outer self-inductance L_{o2} of the train body, the train body self-inductance L can be obtained as

$$L_{i2} = \frac{\mu_0}{2\pi[r_2^2-(r_2-\delta_2)^2]^2}\left\{\frac{1}{4}\left[r_2^4-(r_2-\delta_2)^4\right]\right.$$
$$\left.-r_3^2[r_2^2-(r_2-\delta_2)^2]+(r_2-\delta_2)^4\ln\frac{r_2}{r_2-\delta_2}\right\}, \tag{17}$$

$$L_{o2} = \frac{\mu_0}{2\pi}\ln\frac{d-r_1}{r_2}, \tag{18}$$

$$L = L_{i2} + L_{o2}. \tag{19}$$

The vehicle-catenary-rail model of the urban rail train is built based on the EMTP software to calculate the unbalanced voltage of the train body U_c, which is shown in Fig. 12. The train is composed of two tractors (01M, 04M) and two trailers (02T, 03T). The pantograph is connected to the train body by high-voltage cables, and the train body is connected to the rails by a grounding system. As mentioned in Sec. III, the inflow of transient grounding current into the train body is responsible for U_c, and the frequency of the transient current is approximately 100 kHz, as shown in Fig. 7. Thus, the AC model is built with the transient grounding current as the source. Relevant parameters can be obtained from on-site measurements, theoretical calculations, and table lookup, as listed in Table 5.

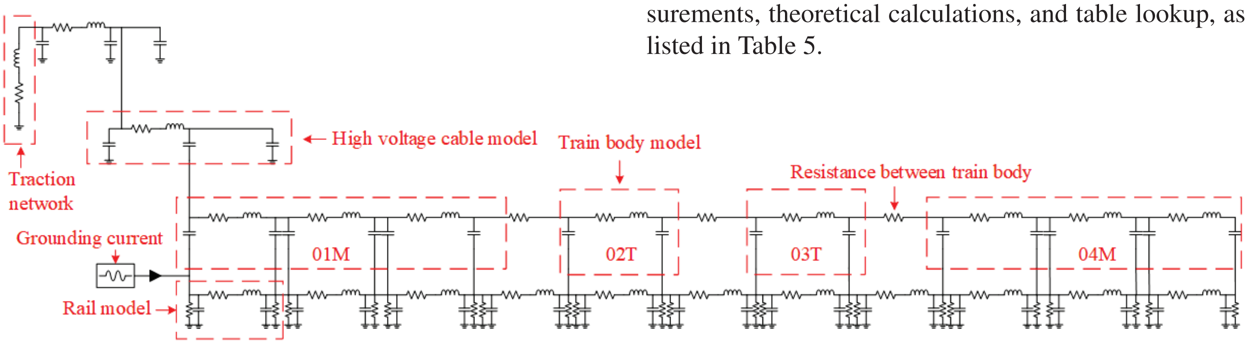

Fig. 12. The vehicle-catenary-rail model of urban rail train.

Table 5: Relevant parameters of urban rail train

Variable	Value	Variable	Value	Variable	Value
C_{10} /(μF)	0.005611	D/(m)	6.5	High voltage cable inductance/(mH/m)	0.000131
C_{20} /(μF)	0.005611	r_1/(m)	0.01	High voltage cable capacitance /(μF/m)	0.000411
C_{12} /(μF)	0.001414	b/(m)	2.8	Rail resistance/(mΩ/m)	5.15
μ_0 /(H/m)	$4\pi\times10^{-7}$	h/(m)	3.8	Rail inductance/(mH/m)	0.00178
μ_r	150	m/(kg)	150	Rail capacitance/(μF/m)	0.000852
μ/(H/m)	$4\pi\times10^{-7}$	ρ/(kg/m^3)	2700	Train body resistance/(mΩ/m)	0.15
γ_1/(S/m)	4.762×10^6	Traction substation resistance/(Ω)	0.165	Train body inductance /(mH/m)	0.000473
γ_2/(S/m)	5.8×10^7	Traction substation inductance/(mH)	10.8	Train body capacitance/(μF/m)	0.0000234
R'/(mm)	109	High voltage cable resistance/(mΩ/m)	0.014	Resistance between train body/(mΩ)	4

IV. VERIFICATION AND ANALYSIS

This section is divided into two parts, including the correctness of the capacitive coupling model and measures for interference suppression.

A. Verification of coupling model

The transient voltage waveform of the rail obtained by EMTP is shown in Fig. 13, revealing a maximum value of 4867 V. The unbalanced voltage U_c of the train body is shown in Fig. 14 with a maximum voltage of 3632 V.

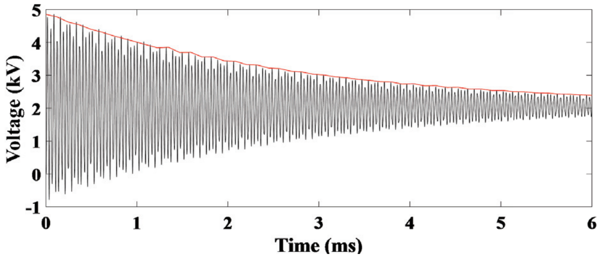

Fig. 13. The transient voltage of rail.

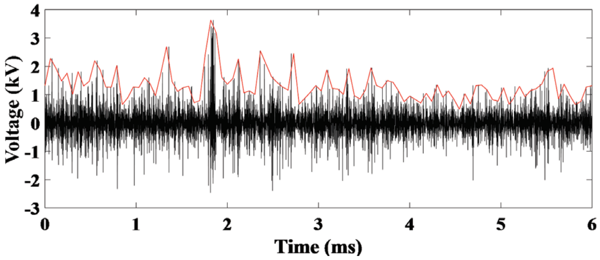

Fig. 14. The unbalanced voltage U_c of train body.

According to the coupling model illustrated in Fig. 8, when T_3 is conducting, its resistance is 0.2 Ω, and the output equivalent resistance R_c is 2.4 Ω; otherwise, its resistance is 2.4 kΩ, and the output equivalent resistance R_c is 2.4 kΩ. The voltage U_{12} coupled to the output port in the aforementioned two states can be calculated. As shown in Fig. 15 (a), when the output of the PWM encoder is at a low level, the peak voltage resulting from transient current coupling to the output port can reach up to 33 V. Conversely, when the output is at a high level, as shown in Fig. 15 (b), the maximum peak voltage of the output port reaches 1894 V. Compared to the voltage of the encoder output port, 1843 V, measured by the oscilloscope in Fig. 6, the absolute error between simulated and measured voltage results is small, indicating the soundness of the coupled model and mechanism analysis.

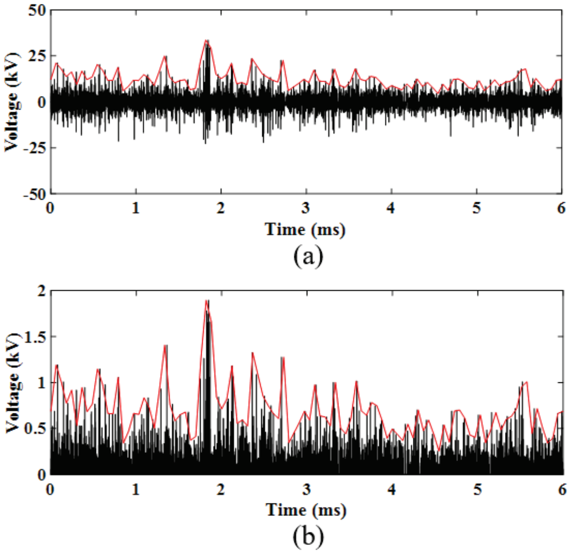

Fig. 15. The output port voltage of PWM encoder: (a) low level, (b) high level.

B. EMI suppression measures

Because the PWM encoder and the train are produced and supplied by different companies with different EMC standards, it is easy to cause the resistance and MOSFET to be burned. It can be seen from the SUG test that the PWM encoder needs to be able to withstand higher surge impulse voltages. Therefore, from the perspective of sensitive equipment, enhancing its immunity to suppress EMI can be considered as a solution. The suppression measure involves selecting the thyristor surge suppressors (TSS) P0300SC and installing them between the positive and negative lines of the output port of the PWM encoder. A schematic diagram depicting this arrangement is shown in Fig. 16.

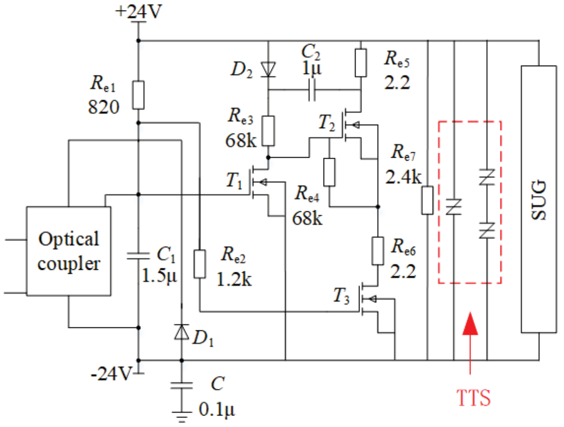

Fig. 16. The schematic diagram of installing TSS at PWM encoder output port.

When the PWM encoder is working properly, the TSS is cut off. When the surge transient voltage is coupled and impacts the internal circuit, the TSS will be conducting to discharge the surge current to the ground, thereby protecting the internal components of the encoder.

The SUG test was performed following the internal circuit diagram described above after the TSS was installed, and the results are shown in Table 6. Compared to the original case without the suppression measure, the encoder with TSS can withstand a voltage of up to 3.3 kV and its working state is not affected, which can effectively suppress the EMI. Furthermore, the components are not burned and the train operates normally after putting the encoder with the TSS into the urban rail train.

Table 6: SUG immunity results of PWM encoder with TSS

Location	**Grade**	**Test Times**	**Results**
Internal circuit port	±1.8 kV	20	Normal
	±3.2 kV	20	Normal
	±3.3 kV	20	Normal
	±3.4 kV	20	Burned

V. CONCLUSION

In this paper, EMC tests are conducted to investigate the types of EMI sources and interference coupling paths for the PWM encoder used in urban rail trains in Brazil. A coupling model is then established based on the test data to analyze the interference coupling mechanism of the encoder. It is shown that the unbalanced voltage of the train body is the main cause for the interference of the PWM encoder, which can reach a peak voltage of up to 3632 V. In addition, the unbalanced voltage of the train body will be coupled to the internal port of the PWM encoder via the shielded cable with a coupling voltage of 1894 V, which can cause EMI on the encoder and burn out its components. This voltage value is consistent with the EMC test and measurement data, validating the correctness of the analysis.

Finally, the EMI problem of the PWM encoder has been solved by installing the TSS P0300SC between the positive and negative lines of the output port of the PWM encoder, which increases the interference voltage from 1.8 kV to 3.3 kV.

ACKNOWLEDGMENT

This work is supported by the National Key R&D Program of China (No.2018YFC0809500) and the Science and Technology Project of Sichuan College of Architectural Technology (No.2023KJ05).

REFERENCES

[1] Y. Tang, F. Zhu, and Y. Chen. "Research on the influence of train speed change on the EMI of pantograph-catenary arc to main navigation stations," *Applied Computational Electromagnetics Society (ACES) Journal*, vol. 36, no. 4, pp. 450-457, 2021.

[2] Y. Tang, F. Zhu, H. Lu, and X. Li, "Analysis and suppression of EMI for traction control unit speed sensors of CRH380BL electric multiple unit," *Applied Computational Electromagnetics Society (ACES) Journal*, vol. 66, no. 5, pp. 553-560, May 2018.

[3] D. S. Jia and S. S. Wang, "Application of PWM encoder based on micro-controller for light rail vehicles," *Electric Locomotives & Mass Transit Vehicles*, vol. 31, no. 1, pp. 23-26, Jan. 2008.

[4] K. Huang, Z. Liu, F. Zhu, Z. Zheng, and Y. Cheng, "Evaluation scheme for EMI of train body voltage fluctuation on the BCU speed sensor measurement," *IEEE Transactions on Instrumentation and Measurement*, vol. 66, no. 5, pp. 1046-1057, May 2017.

[5] D. Franco, M. Aguado, C. Pinedo, I. Lopez, I. Adin, and J. Mendizabal, "A contribution to safe railway operation: evaluating the effect of electromagnetic disturbances on balise-to-BTM communication in railway control signaling systems," *IEEE Vehicular Technology Magazine*, vol. 16, no. 2, pp. 104-112, June 2021.

[6] Y. Wen, Q. Geng, J. Xiao, Y. Zhu, D. Zhang, and P. Spadoni, "Study on the electromagnetic susceptibility of balise transmission module system," *International Conference on Electromagnetics in Advanced Applications*, Cartagena De Indias, Colombiano, pp. 667-670, 2018.

[7] C. Song, R. Wang, and Y. Feng, "Potential EMI analysis of the LED display panel driving current," *Journal of Optoelectronics Laser*, vol. 24, no. 6, pp. 1059-1064, June 2017.

[8] S. Kim, S. An, N. Kim, H. Jeong, and H. Choi, "Circuit design for broad band EMI reduction in LCD driver IC," *2014 NORCHIP*, pp. 1-4, 2014.

[9] J. Guardado, S. Maximov, E. Melgoza, J. Naredo, and P. Moreno, "An improved arc model before current zero based on the combined Mayr and Cassie arc models," *IEEE Trans. Power Delivery*, vol. 20, no. 1, pp. 138-142, Jan. 2005.

[10] M. Cassie, "Theorie nouvelle des arcs de rupture et de la rigidite des circuits," *Cigre*, pp. 588-608, 1939.

[11] O. Mayr, "Beitrage zur theorie des statischen und des dynamischen lichtbogens," *Archiv fur Elektrotechnik*, vol. 37, no. 12, pp. 588-608, 1943.

[12] X. Wei, G. Guo, P. Chen, and G. Wu, "Influence of protective grounding on high-speed EMU grounding reflux," *Journal of the China Railway Society*, vol. 39, no. 8, pp. 39-44, Aug. 2017.

[13] L. Xie, T. Wang, N. Sun, X. Hou, Z. Chen, C. Ju, and X Zhou, "Study on the mechanism and suppression method of transient overvoltage in high-speed trains," *2020 5th Asia Conference on Power and Electrical Engineering (ACPEE)*, pp. 727-731, 2017.

[14] X. Song, Z. Liu, and Y. Wang, "Study on electromagnetic transient process in split-phase insulator considering viaduct's electrical coupling based on ATP-EMTP," *Power System Protection and Control*, vol. 44, no. 13, pp. 6-13, July 2016.

[15] IEC 62236 Railway Applications-Electromagnetic Compatibility, 2018.

[16] C. Feng and X. Ma, *An Introduction to Engineering Electromagnetic Fields*, Higher Education, Beijing, 2004.

[17] F. Zhu, X. Li, P. Li, J. Li, and X. Xing, "Accurate calculation formula for rail inductance of electrified railway," *China Railway Science*, vol. 38, no. 3, pp. 83-88, May 2017.

[18] Y. Wang and Y. Tsai, "Calculation of the frequency-dependent impedance of rail tracks using a four-parameter equivalent tubular conductor model," *IEEE Trans. Power Delivery*, vol. 19, no. 3, pp. 1142-1147, 2004.

[19] F. Tesche, M. Ianoz, and T. Karlsson, *EMC Analysis Methods and Computational Models*, John Wiley & Sons, New York, 1997.

[20] R. Paul, *Analysis of Multiconductor Transmission Lines*, John Wiley & Sons, New York, 2008.

Yang Yang was born in Shanxi, China, in 1989. She received the master's degree in control theory and control engineering from Northwestern Polytechnical University in 2014. She is currently working toward the Ph.D. degree in electrical engineering at Southwest Jiaotong University, Chengdu, China. At the same time she is also a lecturer at Sichuan College of Architectural Technology.

Her research interests include electromagnetic environment test and evaluation, electromagnetic compatibility analysis, and design in the areas of rail transit.

Feng Zhu was born in Anhui Province, China, in 1963. He received the Ph.D. degree in railway traction electrification and automation from the Southwest Jiaotong University, Sichuan, China, in 1997.

He is currently a full professor with the School of Electrical Engineering, Southwest Jiaotong University. His current research interests include locomotive over-voltage and grounding technology, electromagnetic theory and numerical analysis of electromagnetic field and electromagnetic compatibility analysis and design.

Yuxuan Wang was born in Sichaun Province, China, in 1998. He received the B.S. degree in automation from the University of South China, Hengyang, China, in 2020. He is currently working toward the master's degree in electronic and information engineering at Southwest Jiaotong University, Chengdu, China. His research interests are in the areas of electrified railway, electromagnetic compatibility, electromagnetic environment test and evaluation.

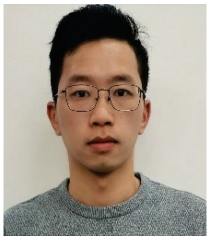

Chengpan Yang was born in Sichaun Province, China, in 1994. He received the master's degree in electrical engineering from Nanjing Normal University, Nanjing, China, in 2020. He is currently working toward the Ph.D. degree in electrical engineering at Southwest Jiaotong University, Chengdu, China.

His research interests are in the areas of electrified railway, electromagnetic compatibility, crosstalk, and multiconductor transmission lines.

Failure Mechanism Analysis of the Stochastic Galerkin Method in EMC Simulation Considering Geometric Randomness

Jinjun Bai, Bing Hu, and Yixuan Wan

College of Marine Electrical Engineering
Dalian Maritime University, Dalian, 116026, China
baijinjun@dlmu.edu.cn, hb1120221308@dlmu.edu.cn, wanyixuan@dlmu.edu.cn

Abstract **–** By virtue of its high calculational accuracy and efficiency, the stochastic Galerkin method (SGM) has been successfully applied many times in electromagnetic compatibility (EMC) simulation in recent years. This paper proposes a calculating example taking geometric uncertainty factors into consideration. As is proved in the paper, there is a relatively large error when using the SGM to solve the example mentioned above. According to failure mechanism, the fundamental reason of the failure of the simulation lies in the additional error caused by using numerical integration to solve the inner product formula. Meanwhile, it is proved that no additional errors are introduced when using the stochastic collocation method (SCM), so the SCM is better than the SGM in stability. In the end, the paper revised the general selective strategy for uncertainty analysis methods, thus providing theoretical basis for their universal application in EMC field.

Index Terms **–** electromagnetic compatibility, failure mechanism analysis, stochastic collocation method, stochastic Galerkin method, uncertainty simulation method.

I. INTRODUCTION

Nowadays, uncertainty simulation methods are widely used in the field of electromagnetic compatibility (EMC) to accurately describe random factors in the actual engineering environment.

The Monte Carlo method (MCM) is the first uncertainty simulation method introduced into the EMC field, but its low computational efficiency renders it uncompetitive [1, 2]. At the same time, some efficient uncertainty simulation methods have also been proposed, such as the perturbation method [3, 4], the moment method [5, 6] and the stochastic reduced order models [7]. However, the calculation accuracy of these methods is not ideal. When the uncertainty of the EMC simulation input is large, the accuracy of the perturbation method will be severely reduced [4]. When the nonlinearity between the input and output of the EMC simulation is large, the moment method will fail [6]. For the stochastic reduced order models, the lack of effective method for judging its convergence will seriously affect the credibility of the simulation results [7].

Since 2013, the stochastic Galerkin method (SGM) [8–11] and the stochastic collocation method (SCM) [12–14] have always been research hotspots and have been widely applied in EMC field till now due to their calculation accuracy and efficiency. Both are based on generalized polynomial chaos theory. The difference is that the SGM is an embedded uncertainty simulation method, while the SCM is non-embedded. Obviously, the SCM is superior to the SGM in terms of stability and ease of implementation. Theoretically, SGM converges faster, causing its accuracy to be slightly higher than SCM [14]. So the following conclusion can be drawn from the reference [14]: Under the premise that the solver can be changed, SGM should be used for EMC uncertainty simulation, because its calculation efficiency and accuracy are slightly better than that of the SCM.

However, as an embedded uncertainty analysis method, the reliability of SGM is inevitably affected by factors such as random variable types and nonlinear boundary conditions. In existing literature, there is a lack of research on its failure mechanism. In this paper, geometric uncertainty factors are taken into account in a benchmark calculating example in both [5] and [15], then an improved calculation example is given. After simulating and analyzing this improved calculation example, it is found that the SGM is not as good as expected. Furthermore, the failure mechanism of the SGM is analyzed in detail. The fairly good accuracy that SGM can show in the existing literature is a “survivorship bias”.

The structure of the paper is as follows: Section II explains the calculation example considering geometric uncertainty. Uncertainty simulation based on the SGM is expressed in Section III. Section IV validates simulation results of the SGM and its validity analysis. The comparison with the uncertainty analysis results provided by the SCM is shown in Section V. Section VI summarizes this paper.

Submitted On: December 17, 2023
Accepted On: September 22, 2023

https://doi.org/10.13052/2023.ACES.J.380702

1054-4887 © ACES

II. CALCULATION EXAMPLE CONSIDERING GEOMETRIC UNCERTAINTY

In an actual engineering environment, geometric uncertainties can be seen everywhere. For example, the geometric position randomness caused by the movement or vibration of the object, the geometric shape uncertainty caused by the manufacturing tolerance, the geometric shape uncertainty caused by damage or erosion, and so on.

Figure 1 shows a calculating example of one-dimensional electromagnetic wave propagation when considering the uncertainty of material parameters and the uncertainty of geometric parameters. It is an improvement of the existing benchmark example in [5] and [15].

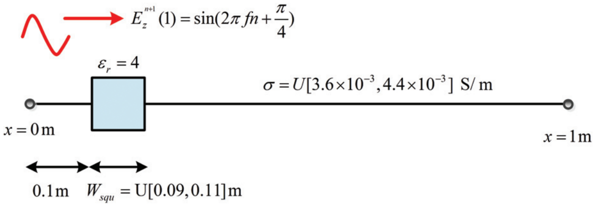
$E_z^{n+1}(1)=\sin(2\pi fn+\frac{\pi}{4})$
$\varepsilon_r=4$
$\sigma=U[3.6\times10^{-3},4.4\times10^{-3}]$ S/m
$x=0$m
$x=1$m
0.1m
$W_{squ}=$ U[0.09,0.11]m

Fig. 1. The calculating example of one-dimensional electromagnetic wave propagation.

The total length of the calculation example is 1 m, and there is a dielectric block starting at x = 0.1 m. There is uncertainty in the length of the dielectric block, which is a uniform distribution in the range of [0.09,0.11] m. The dielectric constant of the block is different from other regions, and the relative dielectric constant of other regions is 1, which is the same as the vacuum dielectric constant $\varepsilon_0 = 8.8542\times10^{-12}$ F/m. The relative dielectric constant of the dielectric block is 4, which is $\varepsilon = 4\times\varepsilon_0$. The end position of the dielectric block can be modeled by the following random variable:

$$W_{\text{pocition}}\left(\xi_1\right) = 0.2 + 0.01\times\xi_1[\text{ m}]. \tag{1}$$

ξ_1 is a random variable with a uniform distribution in the range of $[-1,1]$.

The entire area, including the dielectric block, has the same permeability and conductivity. The value of the permeability is $\mu = 4.0\times\pi\times10^{-7}$ H/m, and the conductivity is an uncertain parameter $\sigma = U\left[3.6\times10^{-3}, 4.4\times10^{-3}\right]$ S/m with a uniform distribution:

$$\sigma\left(\xi_2\right) = 4\times10^{-3}\times\left(1+0.1\xi_2\right)[\text{S/m}]. \tag{2}$$

ξ_2 is also a random variable with a uniform distribution in the range of $[-1,1]$.

There is a sinusoidal excitation source of electric field strength at x = 0 m, and its expression is $\sin\left(2\pi fn+\frac{\pi}{4}\right)$ V/m. Applying the finite difference time domain (FDTD), the space is discretized into 200 discrete points, that is, the space step is $\Delta x = 0.005$ m. In order to meet the Courant stability condition, the time step is calculated by the following formula:

$$\Delta t = \frac{\Delta x}{2\times c} = 8.33\times10^{-12}\text{ s}, \tag{3}$$

where c is the speed of light and its value is 3×10^8 m/s. In this example, the simulation requires 2000 steps, so the total time of electromagnetic wave propagation is $T = 2000\Delta t = 1.67\times10^{-8}$ s. The simulation result is the electric field intensity value of the entire area at time T.

It is worth noting that geometric uncertainty causes the randomness of material properties at different positions, and the corresponding relationship is presented as follows:

$$\varepsilon_r\left(\xi_1,i\right) = \begin{cases} 1, & 1\le i\le 20 \text{ or } 43\le i\le 200 \\ 4, & 21\le i\le 37, \\ F\left(\xi_1\right), & 38\le i\le 42 \end{cases} \tag{4}$$

where i indicates the location of discrete points, and $F\left(\xi_1\right)$ is an unknown constant between 1 and 4.

The set of all random variables can describe the uncertainty factor of the model:

$$\xi = \left\{\xi_1, \xi_2\right\}. \tag{5}$$

After considering the random variable model in (5), one-dimensional random Maxwell equations can be represented:

$$\frac{\partial H_y(\xi)}{\partial t} = \frac{1}{\mu}\left(\frac{\partial E_z(\xi)}{\partial x}\right), \tag{6}$$

$$\frac{\partial E_z(\xi)}{\partial t} = \frac{1}{\varepsilon\left(\xi_1,i\right)}\left(\frac{\partial H_y(\xi)}{\partial x} - \sigma\left(\xi_2\right)E_z(\xi)\right). \tag{7}$$

The uncertainty in the simulation input is reflected in the parameters $\varepsilon\left(\xi_1,i\right)$ and $\sigma\left(\xi_2\right)$. This uncertainty will affect the output results through the simulation process, making it the function of ξ, together with electric field strength $E_z(\xi)$ and magnetic field strength $H_y(\xi)$.

After FDTD transformation [16, 17], the discrete of space and time is realized:

$$\begin{aligned} E_z^{n+1}(i,\xi) &= \alpha(\xi,i)E_z^n(i,\xi) + \beta(\xi,i) \\ &\left[H_y^{n+1/2}(i+1/2,\xi) - H_y^{n+1/2}(i-1/2,\xi)\right], \end{aligned} \tag{8}$$

$$\begin{aligned} H_y^{n+1/2}(i+1/2,\xi) &= H_y^{n-1/2}(i+1/2,\xi) \\ &+ \gamma\left(E_z^n(i+1,\xi) - E_z^n(i,\xi)\right). \end{aligned} \tag{9}$$

The intermediate parameters can be expressed as:

$$\begin{cases} \alpha(\xi,i) = \frac{1-\Delta t\sigma(\xi_2)/2\varepsilon(\xi_1,i)}{1+\Delta t\sigma(\xi_2)/2\varepsilon(\xi_1,i)} \\ \beta(\xi,i) = \frac{\Delta t}{\Delta x\varepsilon(\xi_1,i)[1+\Delta t\sigma(\xi_2)/2\varepsilon(\xi_1,i)]}. \\ \gamma = \frac{\Delta t}{\mu\Delta x} \end{cases} \tag{10}$$

The discrete one-dimensional Maxwell equations with random variables are shown. Then, how to solve these equations based on the SGM will be provided in next section.

Table 1: Legendre polynomial under 2 variables

Expansion Items	Expansion Order	Legendre Polynomial
0	0	1
1	1	$\sqrt{3}\xi_1$
2	1	$\sqrt{3}\xi_2$
3	2	$\frac{\sqrt{5}}{2}\left(3\xi_1^2-1\right)$
4	2	$3\xi_1\xi_2$
5	2	$\frac{\sqrt{5}}{2}\left(3\xi_2^2-1\right)$
6	3	$\frac{\sqrt{7}}{2}\left(5\xi_1^3-3\xi_1\right)$
7	3	$\frac{\sqrt{15}}{2}\left(3\xi_1^2-1\right)\xi_2$
8	3	$\frac{\sqrt{15}}{2}\left(3\xi_2^2-1\right)\xi_1$
9	3	$\frac{\sqrt{7}}{2}\left(5\xi_2^3-3\xi_2\right)$

III. UNCERTAINTY SIMULATION BASED ON THE SGM

The chaotic polynomial is used to expand the simulation outputs in formula (8). For convenience, we only take the first three polynomials as examples.

$$\begin{gathered}E_z^{n+1}(i,\xi)=e_0^{n+1,i}\varphi_0(\xi)+\\ e_1^{n+1,i}\varphi_1(\xi)+e_2^{n+1,i}\varphi_2(\xi),\end{gathered}\tag{11}$$

$$E_z^n(i,\xi)=e_0^{n,i}\varphi_0(\xi)+e_1^{n,i}\varphi_1(\xi)+e_2^{n,i}\varphi_2(\xi),\tag{12}$$

$$\begin{gathered}H_y^{n+1/2}(i+1/2,\xi)=h_0^{n+1/2,i+1/2}\varphi_0(\xi)+\\ h_1^{n+1/2,i+1/2}\varphi_1(\xi)+h_2^{n+1/2,i+1/2}\varphi_2(\xi),\end{gathered}\tag{13}$$

$$\begin{gathered}H_y^{n+1/2}(i-1/2,\xi)=h_0^{n+1/2,i-1/2}\varphi_0(\xi)+\\ h_1^{n+1/2,i-1/2}\varphi_1(\xi)+h_2^{n+1/2,i-1/2}\varphi_2(\xi).\end{gathered}\tag{14}$$

Among them, $\varphi_0(\xi)$, $\varphi_1(\xi)$, and $\varphi_2(\xi)$ are the chaotic polynomials, the coefficients in front of them are the parameters to be solved. According to the Askey rule, there is a one-to-one correspondence between random variables and chaotic polynomials [6]. The random variable with uniform distribution corresponds to the Legendre chaotic polynomial, and the result of the polynomial under one-dimensional random variable ξ_i is proposed as

$$\varphi_0\left(\xi_i\right)=1,\tag{15}$$

$$\varphi_1\left(\xi_i\right)=\sqrt{3}\xi_i,\tag{16}$$

$$\varphi_2\left(\xi_i\right)=\frac{\sqrt{5}}{2}\left(3\xi_i^2-1\right),\tag{17}$$

$$\varphi_3\left(\xi_i\right)=\frac{\sqrt{7}}{2}\left(5\xi_i^3-3\xi_i\right).\tag{18}$$

In the example given in this article, the number of random variables is 2, so the corresponding chaotic polynomial form is presented in Table 1.

The chaotic polynomials are orthogonal to each other, and the mathematical description is:

$$\left\langle\varphi_i,\varphi_j\right\rangle=\left\langle\varphi_i^2\right\rangle\delta_{ij},\tag{19}$$

$$\delta_{ij}=\begin{cases}1 & (i=j)\\ 0 & (i\neq j)\end{cases}.\tag{20}$$

The inner product calculation is defined as

$$\left\langle\varphi_i,\varphi_j\right\rangle=\int\varphi_i(\xi)\varphi_j(\xi)w(\xi)d\xi.\tag{21}$$

Among them, $w(\xi)$ is the weight function, which is the joint probability density function of all random variables. When all random variables are independent of one another, $w(\xi)$ can be calculated by directly multiplying the probability density functions of each random variable. The integral operation in the formula is a multiple definite integral operation. The integral multiplicity is the number of random variables in the random space. The upper and lower limits of the integral are hypercubes composed of the upper and lower limits of each random variable.

After putting formulas (11) to (14) into formula (8), and then applying $\varphi_0(\xi)$ to do the inner product operation on both sides of the equation, the following equation can be provided:

$$\begin{aligned}e_0^{n+1,i}&=e_0^{n,i}\left\langle\alpha(\xi,i)\varphi_0(\xi),\varphi_0(\xi)\right\rangle\\ &+e_1^{n,i}\left\langle\alpha(\xi,i)\varphi_1(\xi),\varphi_0(\xi)\right\rangle+e_2^{n,i}\left\langle\alpha(\xi,i)\varphi_2(\xi),\varphi_0(\xi)\right\rangle\\ &+\left(h_0^{n+1/2,i+1/2}-h_0^{n+1/2,i-1/2}\right)\left\langle\beta(\xi,i)\varphi_0(\xi),\varphi_0(\xi)\right\rangle\\ &+\left(h_1^{n+1/2,i+1/2}-h_1^{n+1/2,i-1/2}\right)\left\langle\beta(\xi,i)\varphi_1(\xi),\varphi_0(\xi)\right\rangle\\ &+\left(h_2^{n+1/2,i+1/2}-h_2^{n+1/2,i-1/2}\right)\left\langle\beta(\xi,i)\varphi_2(\xi),\varphi_0(\xi)\right\rangle.\end{aligned}\tag{22}$$

In the same way, the following equations can be arranged by performing inner product operations with $\varphi_1(\xi)$ and $\varphi_2(\xi)$ respectively:

$$\begin{gathered}\begin{bmatrix}e_0^{n+1,i}\\ e_1^{n+1,i}\\ e_2^{n+1,i}\end{bmatrix}=\begin{bmatrix}A_{0,0}^{\alpha,i} & A_{1,0}^{\alpha,i} & A_{2,0}^{\alpha,i}\\ A_{0,1}^{\alpha,i} & A_{1,1}^{\alpha,i} & A_{2,1}^{\alpha,i}\\ A_{0,2}^{\alpha,i} & A_{1,2}^{\alpha,i} & A_{2,i}^{\alpha,i}\end{bmatrix}\begin{bmatrix}e_0^{n,i}\\ e_1^{n,i}\\ e_2^{n,i}\end{bmatrix}+\\ \begin{bmatrix}A_{0,0}^{\beta,i} & A_{1,0}^{\beta,i} & A_{2,0}^{\beta,i}\\ A_{0,1}^{\beta,i} & A_{1,1}^{\beta,i} & A_{2,1}^{\beta,i}\\ A_{0,2}^{\beta,i} & A_{1,2}^{\beta,i} & A_{2,2}^{\beta,i}\end{bmatrix}\times\begin{bmatrix}h_0^{n+1/2,i+1/2}-h_0^{n+1/2,i-1/2}\\ h_1^{n+1/2,i+1/2}-h_1^{n+1/2,i-1/2}\\ h_2^{n+1/2,i+1/2}-h_2^{n+1/2,i-1/2}\end{bmatrix}.\end{gathered}\tag{23}$$

Among them, the middle parameter represents the inner product operation process:

$$\begin{cases}A_{m,l}^{\alpha,i}=\left\langle\alpha(\xi,i)\varphi_m(\xi),\varphi_l(\xi)\right\rangle\\ A_{m,l}^{\beta,i}=\left\langle\beta(\xi,i)\varphi_m(\xi),\varphi_l(\xi)\right\rangle\end{cases}\quad m,l=0,1,2.\tag{24}$$

As shown in formula (4), due to geometric uncertainty, the inner product calculation formula at each discrete point is different, the calculation formula is calculated as follows:

$$\begin{gathered}\left\langle\alpha(\xi,i)\varphi_{xi}(\xi),\varphi_{yi}(\xi)\right\rangle=\\ \begin{cases}\frac{1}{4}\int_{-1}^{1}\int_{-1}^{1}\frac{1-\Delta t\sigma(\xi_2)/2\varepsilon_0}{1+\Delta t\sigma(\xi_2)/2\varepsilon_0}\varphi_{xi}(\xi)\varphi_{yi}(\xi)d\xi_1d\xi_2\\ \quad 1\leq i\leq 20\text{ or }43\leq i\leq 200\\ Q_\alpha,38\leq i\leq 42\\ \frac{1}{4}\int_{-1}^{1}\int_{-1}^{1}\frac{1-\Delta t\sigma(\xi_2)/8\varepsilon_0}{1+\Delta t\sigma(\xi_2)/8\varepsilon_0}\varphi_{xi}(\xi)\varphi_{yi}(\xi)d\xi_1d\xi_2\\ \quad 21\leq i\leq 37,\end{cases}\end{gathered}\tag{25}$$

$$Q_\alpha = \frac{1}{4}\int_{-1}^{1}\int_{-1}^{\frac{i/40-1}{0.05}} \frac{1-\Delta t\sigma(\xi_2)/2\varepsilon_0}{1+\Delta t\sigma(\xi_2)/2\varepsilon_0}\varphi_{xi}(\xi)\varphi_{yi}(\xi)d\xi_1 d\xi_2 + \frac{1}{4}\int_{-1}^{1}\int_{\frac{i/40-1}{0.1}}^{1} \frac{1-\Delta t\sigma(\xi_2)/8\varepsilon_0}{1+\Delta t\sigma(\xi_2)/8\varepsilon_0}\varphi_{xi}(\xi)\varphi_{yi}(\xi)d\xi_1 d\xi_2, \tag{26}$$

$$\langle \beta(\xi,i)\varphi_{xi}(\xi),\varphi_{yi}(\xi)\rangle = \begin{cases} \frac{1}{4}\int_{-1}^{1}\int_{-1}^{1}\frac{\Delta t}{\Delta x\varepsilon_0[1+\Delta t\sigma(\xi_2)/2\varepsilon_0]}\varphi_{xi}(\xi)\varphi_{yi}(\xi)d\xi_1 d\xi_2 \\ 1\le i\le 20 \text{ or } 43\le i\le 200 \\ Q_\beta, 38\le i\le 42 \\ \frac{1}{4}\int_{-1}^{1}\int_{-1}^{1}\frac{\Delta t}{4\Delta x\varepsilon_0[1+\Delta t\sigma(\xi_2)/8\varepsilon_0]}\varphi_{xi}(\xi)\varphi_{yi}(\xi)d\xi_1 d\xi_2 \\ 21\le i\le 37, \end{cases} \tag{27}$$

$$Q_\beta = \frac{1}{4}\int_{-1}^{1}\int_{-1}^{\frac{i/40-1}{0.05}} \frac{\Delta t}{\Delta x\varepsilon_0[1+\Delta t\sigma(\xi_2)/2\varepsilon_0]} \varphi_{xi}(\xi)\varphi_{yi}(\xi)d\xi_1 d\xi_2 + \frac{1}{4}\int_{-1}^{1}\int_{\frac{i/40-1}{0.05}}^{1} \frac{\Delta t}{4\Delta x\varepsilon_0[1+\Delta t\sigma(\xi_2)/8\varepsilon_0]} \varphi_{xi}(\xi)\varphi_{yi}(\xi)d\xi_1 d\xi_2. \tag{28}$$

Among them, the calculation process of the boundary point $\frac{i/40-1}{0.05}$ of the integral limit is provided as follows:

$$W_{\text{position}}(\xi_{1,\text{lim}}) = 40\Delta x(1+0.05\xi_{1,\text{lim}}), \tag{29}$$

$$W_{\text{position}}(\xi_{1,\text{lim}}) = i\Delta x, \tag{30}$$

$$i\Delta x = 40\Delta x(1+0.05\xi_{1,\text{lim}}), \tag{31}$$

$$\xi_{1,\text{lim}} = \frac{i/40-1}{0.05}. \tag{32}$$

The SGM transforms the stochastic Maxwell equations shown in equation (8) into the augmented deterministic Maxwell equations shown in equation (23). Next, the traditional FDTD method can be used to solve equation (23) to obtain the chaotic polynomial coefficients in equations (11) to (14). Finally, by statistical sampling of random variables, the final uncertainty analysis results can be obtained, such as expectation value, standard deviation, worst-case estimate, probability density curve, and so on.

IV. SIMULATION RESULT OF THE SGM AND ITS VALIDITY ANALYSIS

Figure 2 shows the expectation value results of electric field intensity at each discrete point based on the SGM, and Fig. 3 shows the corresponding standard deviation results. Simulation results of the MCM are also given as standard data.

Feature selective validation (FSV) method [18, 19] is used to compare the difference between two sets of one-dimensional curves. In Fig. 2, the FSV value between the MCM and the SGM in expectation value results is 0.04, and it is presented that the accuracy of the SGM is in "Excellent" level. In Fig. 3, the FSV value is 0.25, and it is shown that the accuracy of the SGM in standard deviation results is only in "Good" level. It is clearly seen that there is a significant difference between the two curves in Fig. 3.

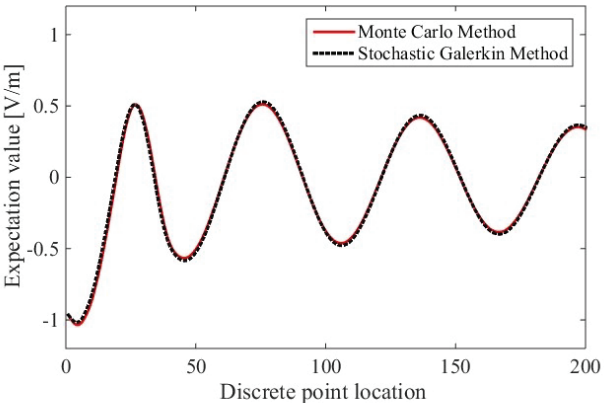

Fig. 2. Comparison of expectation values between the SGM and the MCM.

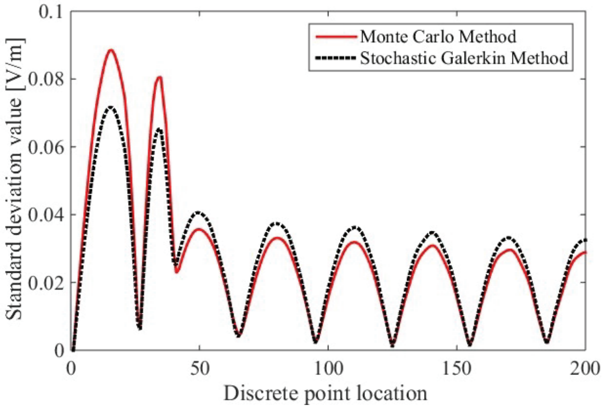

Fig. 3. Comparison of standard deviations between the SGM and the MCM.

Back to equation (4), since $F(\xi_1)$ is an unknown random number, the following inner product calculation formula is needed to deal with this geometric uncertainty:

$$\int_{-1}^{1} f(\varepsilon_r(\xi_1,i))d\xi_1 = \int_{-1}^{1} f(F(\xi_1))d\xi_1 \approx \int_{-1}^{\frac{i/40-1}{0.05}} f(4)d\xi_1 + \int_{\frac{i/40-1}{0.05}}^{1} f(1)d\xi_1, \quad i = 38,\ldots,42. \tag{33}$$

Both equation (26) and equation (28) are derived from the principle shown in equation (33). Figure 4 is given in order to better demonstrate its mathematical principle. It is shown that the area of the curved trapezoid below the red dotted line is approximately equal to the sum of the areas of the two rectangles. This is the principle of numerical integration calculation.

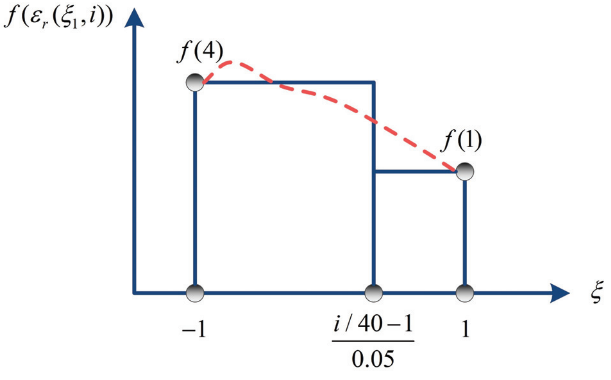

Fig. 4. Mathematical principle of numerical integration calculation.

This approximate calculation is right, but additional error will ensue. For under normal conditions, the error in the SGM is caused solely by the truncation of chaotic polynomials. However, in this calculation example, there is not only truncation error, but also additional error caused by numerical integration operations. Therefore, the introduction of additional error is the reason why the SGM fails.

V. UNCERTAINTY SIMULATION BASED ON THE SCM

The uncertainty simulation based on the SCM is given in this section as a comparison. Zero points of the chaotic polynomial are selected as the collocation points of the SCM. According to numerical analysis theory, these zero points are Gaussian volume points, which can maximize the convergence of the algorithm and thus improve its computational accuracy [12, 14]. For example, the collocation points in the case of one-dimensional and three-order polynomial (17) is $\left\{0,\pm\frac{\sqrt{15}}{5}\right\}$. In this paper, the calculation example contains two random variables, and the collocation points are given in the form of tensor product $\mathrm{P}_{SCM}=\left\{0,\pm\frac{\sqrt{15}}{5}\right\}\otimes\left\{0,\pm\frac{\sqrt{15}}{5}\right\}$. Performing the multi-dimensional Lagrange interpolation algorithm on the collocation points, the uncertainty analysis results of the SCM can be obtained:

$$\mathrm{EMC}_{\mathrm{SCM}}(\xi)=\sum_{j_1=1}^{3}\sum_{j_2=1}^{3}\mathrm{EMC}\left(\mathrm{P}_{SCM}\right)\times\mathrm{Lag}\left(\mathrm{P}_{SCM},\xi\right). \tag{34}$$

ξ still represents a collection of random variables $\{\xi_1,\xi_2\}$. $\mathrm{EMC}\left(\mathrm{P}_{SCM}\right)$ refers to the deterministic EMC simulation result at the collocation points. $\mathrm{Lag}\left(\mathrm{P}_{SCM},\xi\right)$ refers to the multidimensional Lagrange interpolation results at the collocation points, and it is a function of the random variable ξ.

Finally, statistical sampling is also required, and the final uncertainty analysis results can be obtained.

The uncertainty analysis based on the SCM is performed on the calculating example in Fig. 1, the results of expectation values and standard deviations are provided in Figs. 5 and 6, respectively. Using the FSV method, the FSV value between the MCM and the SCM in expectation value results is 0.03, and the value in standard deviation results is 0.07. Compared with FSV values of SGM, both 0.03 and 0.04 belong to the range of greater than 0 but less than 0.1, which belongs to the "Excellent" level in the qualitative judgment criteria for FSV. However, the difference between 0.03 and 0.04 is not significant, and it can be considered that the accuracy of the expected values for the SCM and the SGM is very similar. Looking at the standard deviation results in Fig. 6, it is evident from the figures that the accuracy of the SCM is much higher than that of the SGM. From the perspective of

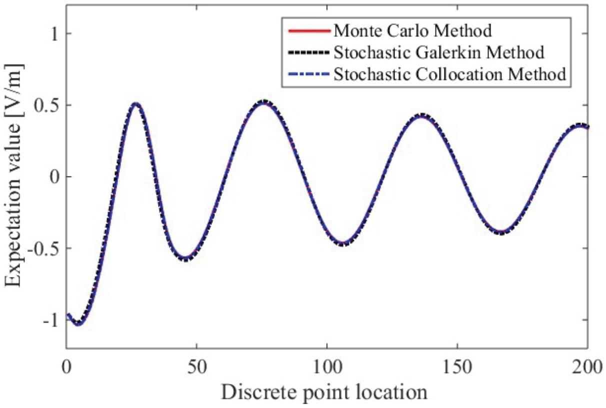

Fig. 5. Expectation values provided by the SCM.

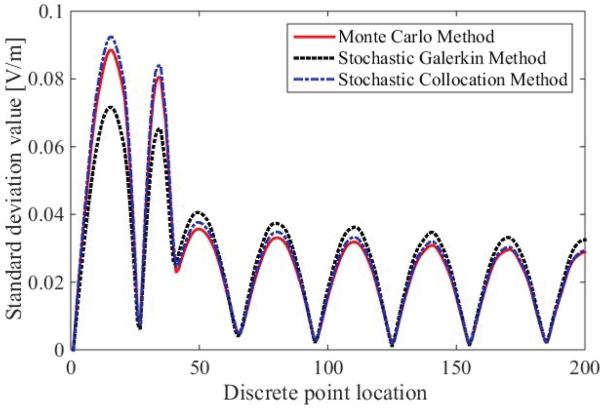

Fig. 6. Standard deviations provided by the SCM.

FSV value, the SCM's FSV value of 0.07 still belongs to the "Excellent" level, while the SGM's 0.25 is only the "Good" level, which differs by two levels in qualitative standards. In summary, in this calculation example, the calculation accuracy of the SCM is much higher than that of the SGM, which is at the same level of accuracy as the MCM.

The SCM is a non-embedded uncertainty analysis method and will not modify the original solver. Therefore, there is only truncation error of the chaotic polynomial in the SCM simulation results and no additional error introduced by the numerical integration. Conversely, the SGM contains two types of errors (its principle has been explained in Fig. 4), so the theoretical accuracy of the SGM in this example is lower than that of the SCM. Obviously, in this calculating example, the SCM is more accurate than the SGM. Therefore, the reliability of the SCM is much higher than that of the SGM, and only a stable and reliable deterministic EMC solver is needed. At the same time, the programming implementation of the SCM is much easier than the SGM, and it can effectively avoid calculation accuracy deviations caused by programming errors.

The simulation time of the MCM is 1.17 hours, and that of the SGM is 0.10 hours, but that of the SCM is only 5.16 seconds. Because the MCM is based on the law of weak large numbers, a large number of deterministic EMC simulations are needed to ensure convergence, so the simulation time is the longest. The SGM needs to calculate the numerical integration at different discrete points, so it also takes a certain amount of time for simulation. The SCM takes the shortest time since it only needs 9 deterministic EMC simulations.

It is worth noting that the single EMC simulation time of this example is relatively short, so the time of numerical integration calculation appears relatively long. As a result, the calculation efficiency of the SCM is better than that of the SGM. However, when the single simulation time is much longer than the numerical integration time, the calculation efficiency of the SGM and the SCM are at the same level. Of course, their computational efficiency is far better than the MCM under any conditions.

VI. CONCLUSION

After properly taking geometric uncertainty into consideration, this paper, aiming at a published example of a typical EMC simulation, found that the results of uncertainty analysis of the SGM are far from expected, which means the error of the SGM was hard to ignore. According to failure mechanism, the root cause of the failure of the simulation is the additional error introduced by using numerical integration to solve the inner product formula. Compared with the results of the SCM, it's concluded that the SCM is more accurate than the SGM when processing geometric uncertainty factors.

Through analysis of the failure mechanism, the applicable scope of the SGM was further determined, thus general selective strategies of uncertainty analysis method should be rectified: (1) the MCM should be adopted when the time of a single simulation is relatively short; (2) the SGM should be selected when a model has long single simulation time, high computational accuracy demand, and its solver is easy to change without modifying the inner product formula; (3) the SCM is to be preferred in any other situation that hasn't been mentioned above.

ACKNOWLEDGMENT

This work was supported in part by the Youth Science Foundation Project, National Natural Science Foundation of China, under Grant 52301414.

REFERENCES

[1] S. A. Pignari, S. Giordano, and G. Flavia, "Modeling field-to-wire coupling in random bundles of wires," *IEEE Electromagnetic Compatibility Magazine*, vol. 6, no. 3, pp. 85-90, Nov. 2017.

[2] H. Xie, J. F. Dawson, J. Yan, A. C. Marvin, and M. P. Robinson, "Numerical and analytical analysis of stochastic electromagnetic fields coupling to a printed circuit board trace," *IEEE Transactions on Electromagnetic Compatibility*, vol. 62, no. 4, pp. 1128-1135, Aug. 2020.

[3] Y. Zhang, C. Liao, R. Huan, Y. Shang, and H. Zhou, "Analysis of nonuniform transmission lines with a perturbation technique in time domain," *IEEE Transactions on Electromagnetic Compatibility*, vol. 62, no. 2, pp. 542-548, April 2020.

[4] A. Gillman, A. H. Barnett, and P.-G. Martinsson, "A spectrally accurate direct solution technique for frequency domain scattering problems with variable media," *BIT Numerical Mathematics*, vol. 55, no. 1, pp. 141-170, Aug. 2013.

[5] J. Bai, G. Zhang, L. Wang, and T. Wang, "Uncertainty analysis in EMC simulation based on improved method of moments," *Applied Computational Electromagnetics Society Journal*, vol. 31, no. 1, pp. 66-71, Jan. 2016.

[6] R. Edwards, A. Marvin, and S. Porter, "Uncertainty analyses in the finite difference time domain method," *IEEE Transactions on Electromagnetic Compatibility*, vol. 52, no. 1, pp. 155-163, Feb. 2010.

[7] Z. Fei, Y. Huang, J. Zhou, and Q. Xu, "Uncertainty quantification of crosstalk using stochastic reduced order models," *IEEE Transactions on Electromagnetic Compatibility*, vol. 59, no. 1, pp. 228-239, Feb. 2016.

[8] P. Manfredi, D. V. Ginste, I. S. Stievano, D. De Zutter, and F. G. Canavero, "Stochastic transmission line analysis via polynomial chaos methods: An overview," *IEEE Electromagnetic Compatibility Magazine*, vol. 6, no. 3, pp. 77-84, Nov. 2017.

[9] P. Manfredi, D. V. Ginste, D. De Zutter, and F. G. Canavero, "Generalized decoupled polynomial chaos for nonlinear circuits with many random parameters," *IEEE Microwave & Wireless Components Letters*, vol. 25, no. 8, pp. 505-507, Aug. 2015.

[10] P. Manfredi, R. Trinchero, and D. V. Ginste, "A perturbative stochastic Galerkin method for the uncertainty quantification of linear circuits," *IEEE Transactions on Circuits and Systems*, vol. 67, no. 9, pp. 2993-3006, 2020.

[11] T.-L. Wu, F. Buesink, and F. Canavero, "Overview of signal integrity and EMC design technologies on PCB: Fundamentals and latest progress," *IEEE Transactions on Electromagnetic Compatibility*, vol. 55, no. 4, pp. 624-638, Aug. 2013.

[12] B. Xia, Y. Chen, W. Yang, Q. Chen, X. Wang, and K. Min, "Stochastic optimal power flow for power systems considering wind farms based on the stochastic collocation method," *IEEE Access*, vol. 10, no. 1, pp. 44023-44032, April 2022.

[13] Y. Chi, B. Li, X. Yang, T. Wang, K. Yang, and Y. Gao, "Research on the statistical characteristics of crosstalk in naval ships wiring harness based on polynomial chaos expansion method," *Polish Maritime Research*, vol. 24, no. s2, pp. 205-214, Aug. 2017.

[14] J. Bai, G. Zhang, D. Wang, A. P. Duffy, and L. Wang, "Performance comparison of the SGM and the SCM in EMC simulation," *IEEE Transactions on Electromagnetic Compatibility*, vol. 58, no. 6, pp. 1739-1746, Dec. 2016.

[15] J. Bai, G. Zhang, L. Wang, and D. Alistair, "Uncertainty analysis in EMC simulation based on stochastic collocation method," *IEEE Electromagnetic Compatibility Magazine*, pp. 930-934, Sep. 2015.

[16] M. Moradi, V. Nayyeri, S.-M. Sadrpour, M. Soleimani, and O. M. Ramahi, "A 3-D weakly conditionally stable single-field finite-difference time-domain method," *IEEE Transactions on Electromagnetic Compatibility*, vol. 62, no. 2, pp. 498-509, April 2020.

[17] R. Tsuge, Y. Baba, H. Kawamura, and N. Itamoto, "Finite-difference time-domain simulation of a lightning-impulse-applied ZnO element," *IEEE Transactions on Electromagnetic Compatibility*, vol. 62, no. 5, pp. 1780-1786, Oct. 2020.

[18] A. P. Duffy, A. Orlandi, and Z. Gang, "Review of the feature selective validation method (FSV). Part I-Theory," *IEEE Transactions on Electromagnetic Compatibility*, vol. 60, no. 4, pp. 814-821, Aug. 2018.

[19] A. Orlandi, A. P. Duffy, and Z. Gang, "Review of the feature selective validation method (FSV). Part II-Performance analysis and research fronts," *IEEE Transactions on Electromagnetic Compatibility*, vol. 60, no. 4, pp. 1029-1035, Aug. 2018.

Jinjun Bai received the Ph.D. degree in electrical engineering in 2019 from the Harbin Institute of Technology, Harbin, China. He is now a lecturer at Dalian Maritime University. His research interests include uncertainty analysis methods in EMC simulation.

Bing Hu He is currently a graduate student in electrical engineering at Dalian Maritime University, where his research interests include uncertainty analysis methods in EMC simulation.

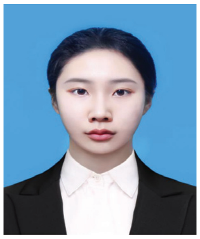

Yixuan Wan She is working toward a master's degree in electrical engineering. Her current research on simulation of electromagnetic radiation related to electric vehicles. She is now engaged in electric vehicle cable harness crosstalk simulation.

Antenna Synthesis by Levin's Method using Reproducing Kernel Functions

Goker Sener

Department of Electrical-Electronics Engineering
Cankaya University, Ankara, 06790, Turkey
sener@cankaya.edu.tr

Abstract **–** An antenna synthesis application is presented by solving a highly oscillatory Fourier integral using a stable and accurate Levin's algorithm. In antenna synthesis, the current distribution is obtained by the inverse Fourier integral of the antenna radiation pattern. Since this integral is highly oscillatory, the Levin method can be used for its solution. However, when the number of nodes or the frequency increases, the Levin method becomes unstable and ineffective due to the large condition number of the interpolation matrix. Thus, an improved scheme of the method is used in an antenna synthesis application in which reproducing kernel functions are used as the basis of the approximation function. The accuracy of the new method is verified by a log-periodic antenna example. The error and stability analysis results show that the new method is more stable and accurate than other well-known kernels, especially for a large number of nodes.

Index Terms **–** Antenna synthesis, Fourier integral, highly oscillatory integrals, Levin's method, reproducing kernel functions.

I. INTRODUCTION

Antenna synthesis aims to find the current distribution on a specific antenna geometry that yields the desired radiation pattern. This procedure is called beam shaping and is applied using the Fourier transform technique [1]. In antenna analysis, the Fourier integral of the current distribution gives the antenna radiation characteristics. Conversely, in antenna synthesis, the inverse Fourier integral of the radiation pattern gives the current distribution on the antenna geometry [2].

Since the Fourier integral is highly oscillatory, numerical techniques such as the Simpson rule and Gaussian-type quadrature methods are ineffective for solving such integrals [3]. Instead, the asymptotic expansion method (stationary phase), steepest descent method, and Filon and Levin methods are used [4, 5]. Each method has its advantages and disadvantages. For instance, in the asymptotic expansion method, the accuracy of the algorithm is dependent on the degree of oscillation. In the steepest descent and Filon methods, the steepest descent paths and the moments must be calculated, respectively. Similarly, in the Levin method, the solution fails in the presence of stationary points.

Nevertheless, the Levin method is used extensively and yields accurate solutions, especially with complex phase functions. Furthermore, the Levin method can be modified to obtain successful results even in stationary points utilizing a class of specific kernels such as radial basis functions (RBFs) [6]. For example, in [7, 8], Levin's method, utilizing multiple quadrature radial basis functions (MQ-RBFs), is employed to provide accurate solutions in terms of relative errors for highly oscillatory integrals, both with and without singular points. Similarly, in [9], different RBFs such as the Gaussian type, are used to improve the convergence of the method in the presence of singular points.

The key feature of the Levin method is to convert integrals into a system of ordinary differential equations (ODEs), or partial differential equations (PDEs) [10, 11]. The solution of these equations is usually found by the linear equation system constructed by the collocation methods [12, 13]. In general, the accuracy of the differential equation solution determines the accuracy of the method.

The major drawback of the Levin method, with or without RBFs, is that the convergence matrix becomes ill-conditioned at high frequencies or when the number of nodes exceeds 10. In this case, the stability of the method decreases. The most common strategy against this problem is to use fewer nodes and divide the integration domain into more sub-intervals. On the other hand, if the domain has to be partitioned at a small number of intervals, mainly for faster evaluations, then the interpolation matrix has to be banded (sparse) for better convergence. There have been some attempts toward this goal in the literature. For example, in [9], the stability of the Levin method is increased by using Gaussian RBFs. Also, in a recent study in [14], the Levin method is modified to be an accurate and stable algorithm using compactly supported radial basis functions (CS RBFs). In this technique, the stability is increased because the

Submitted On: September 21, 2022
Accepted On: September 5, 2023

https://doi.org/10.13052/2023.ACES.J.380703

1054-4887 © ACES

application of CS RBFs for large-scale problems results in a sparse matrix of the system due to compact support [15]. However, the disadvantage of this method is that although it gives good stability in the solution of a high-dimensional system of equations, its accuracy decreases, especially when used with a small number of collation points.

In a recently published study in [16], another class of base functions, called reproducing kernel functions, are used in the Levin method for the first time, and very stable and accurate results are obtained. Reproducing kernel functions (RKFs) are defined in the reproducing kernel Hilbert space. This theory has been used to solve fractional differential equations and singular boundary value problems for the last few decades [17, 18].

In this paper, Levin's method using RKFs, is used in an antenna synthesis application for the first time. First, the radiation pattern of a rotatable log periodic antenna (RLPA), 4030/LP/10, is sampled and transferred into Matlab. Next, this data is used to solve the inverse Fourier integral to find the equivalent antenna current distribution on a linear conductor. The accuracy of the results is verified by comparing the radiation pattern created by this current source with the original antenna pattern. The error and stability analysis results regarding the absolute error and matrix condition numbers are presented. The results for the RKF are also compared with the monomial and the radial Gaussian basis functions, which are known to yield accurate and stable outcomes with the Levin method. It is concluded that RKF offers the best accuracy and stability, particularly for a small number of integration intervals and a large number of collocation points.

II. LEVIN'S METHOD

Levin's method is used to solve highly oscillatory integrals in the form

$$I=\int_a^b f(x)e^{iq(x)}dx, \tag{1}$$

where $f(x)$ is a smooth and slowly varying function, and $q(x)$ is a highly oscillating function, usually written as $q(x)=\omega g(x)$, where ω is a constant and $g(x)$ is a non-oscillatory smooth function. The oscillating nature of $q(x)$ requires that $|q'(x)|\approx\omega\gg(b-a)^{-1}$.

The integration variable x can be any physical variable, such as time. In antenna synthesis applications, a and b define the limits for the integration variable x, which is defined as the angle for the radiation pattern function and the distance for the antenna length.

In Levin's method, the function $f(x)$ is defined as

$$f(x)=iq'(x)p(x)+p'(x)=L^{(1)}p(x). \tag{2}$$

Substituting (2) in (1) gives

$$\begin{aligned} I &= \int_a^b \left(iq'(x)p(x)+p'(x)\right)e^{iq(x)}dx \\ &= \int_a^b \frac{d}{dx}\left(p(x)e^{iq(x)}\right)dx \\ &= p(b)e^{iq(b)}-p(a)e^{iq(a)}. \end{aligned} \tag{3}$$

Thus, the evaluation of the integral in (1) is reduced to finding $p(a)$ and $p(b)$. The function $p(x)$ can be approximated at n collocation points as

$$p_n(x)=\sum_{k=1}^{n}\alpha_k u_k(x), \tag{4}$$

where $\{u_k(x)\}_{k=1}^{n}$ are some linearly independent basis functions, and α_k's are the coefficients to be determined by the n collocation conditions

$$L^{(1)}p_n(x_j)=f(x_j),\ j=1,2,...,n. \tag{5}$$

Substituting (4) into (2) using (5) gives the linear equation system

$$\begin{gathered}\sum_{k=1}^{n}\alpha_k u_k'(x_j)+iq'(x_j)\sum_{k=1}^{n}\alpha_k u_k(x_j)=f(x_j), \\ j=1,2,3,...,n,\end{gathered} \tag{6}$$

whose solution gives the unknown coefficients $\{\alpha_k\}_{k=1}^{n}$. Then, (4) is substituted into (4) to find the solution to the integral in (1) as

$$I=\sum_{k=1}^{n}\alpha_k u_k(b)e^{iq(b)}-\sum_{k=1}^{n}\alpha_k u_k(a)e^{iq(a)}. \tag{7}$$

The large convergence matrix of the linear system reduces the stability and efficiency of the method. In order to overcome this problem, instead of increasing the collocation number n, the interval $[a,b]$ is divided into more sub-intervals. Alternatively, in the case of a small number of sub-intervals and a large number of collocation points, the linear system matrix can be made well-conditioned to maintain stability and accuracy. For this purpose, the basis function set $u_k(x)$ should be chosen to be suitable with the collocation approximation. For example, if the function $f(x)$ is a polynomial, then the $u_k(x)$ should be a polynomial as well. In any case, the selection of the basis function set is vastly important in terms of the stability and the accuracy of the Levin method.

III. LEVIN'S METHOD WITH REPRODUCING KERNEL FUNCTIONS

In Levin's method, the basis function $\{u_k(x)\}_{k=1}^{n}$ is given as

$$u_k(x)=\lambda_{k,y}K^m(x,y), \tag{8}$$

where $K^m(x,y)$ is the reproducing kernel function, defined as [16]

$$K^m(x,y)=\begin{cases}\xi(x,y), & y\le x\\ \xi(y,x), & y>x\end{cases}, \tag{9}$$

where

$$\xi(x,y) = \sum_{i=0}^{m-1} \left(\frac{y^i}{i!} + (-1)^{m-1-1} \frac{y^{2m-1-i}}{(2m-1-1)!} \right) \frac{x^i}{i!}, \tag{10}$$

and $\lambda_k = \delta_{x_k}$, $k = 1,2,...,n$, is the evaluation function and $\lambda_{k,y}$ is λ_k acting on the function of y. The reproducing kernel function $K^m(x,y) \in H^m[a,b]$, where $H^m[a,b]$ is the reproducing kernel Hilbert space with $m > 1$.

By definition, a Hilbert space H is named as reproducing kernel Hilbert space (RKHS), if for each $x \in E$, the function $K : E \times E \to R$ is known as the reproducing kernel function (RKF) of the Hilbert function space H. The reproducing property of the Hilbert space is satisfied when

$$K(\cdot,x) \in H \; for \; all \; x \in \Omega, \tag{11}$$

and

$$p(x) = \langle p(\cdot), K(\cdot,x) \rangle, \tag{12}$$

where the inner product property is called the reproducing property of the Hilbert space. Figure 1 shows the mapping $K : E \times E \to R$ through the Hilbert space. For further information on RKHS, the reader can refer to [19, 20].

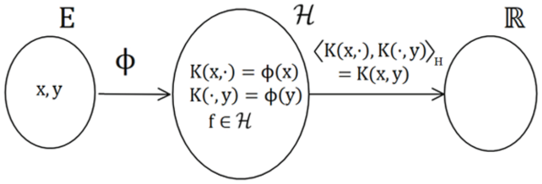

Fig. 1. Mapping diagram for RKHS.

IV. ANTENNA SYNTHESIS APPLICATION I

A. Obtaining the radiation pattern

In this section, Levin's method with RKF is used in an antenna synthesis application. For this purpose, the radiation pattern (space factor for the electric field) of the rotatable log periodic antenna, 4030/LP/10 manufactured by Giovannini E., is obtained from its spec sheet [21]. It is then interpolated by cubic splines at 91 points, and the pattern function, $f(\theta)$, in Fig. 2 is obtained.

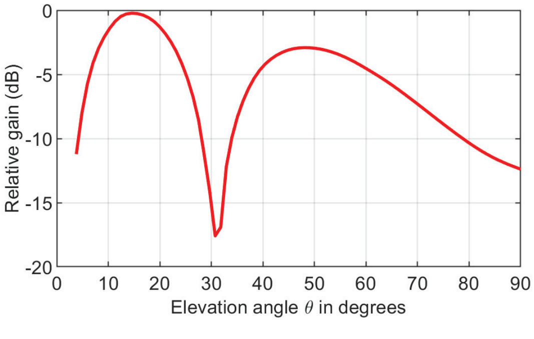

Fig. 2. The radiation pattern of the antenna 4030/LP/10.

B. Finding the current distribution

The equivalent current distribution on a linear antenna is found by solving the inverse Fourier integral

$$I(z') = \frac{1}{2\pi} \int_{-\infty}^{\infty} f(\theta) e^{-jz'\xi} d\xi, \tag{13}$$

where $I(z')$ is the unknown current distribution, and $f(\theta)$ is the desired radiation pattern. The antenna is assumed to be located along the vertical z' axis, where the prime notation is used to designate the source coordinates. The variable ξ is defined as $\xi = kcos\theta$, where k is the free space wavenumber.

The limits of the integral in (13) are truncated to $\theta \in [90°, 0°]$ or $\xi \in [0,k]$, and the integral is divided into ℓ subintervals with each subinterval having n collocation points (knots). Thus, the integral for each subinterval can be written as

$$I_i(z') = \frac{1}{2\pi} \int_{kcos\theta_i}^{kcos\theta_{i+1}} \dot{f}(\theta) e^{-jz'\xi} d\xi, \; i = 1,2,...,\ell, \tag{14}$$

where $\dot{f}(\theta)$ is the part of the radiation pattern in the given interval. Due to the linearity, the total current can be written as

$$I(z') = \sum_{i=1}^{\ell} I_i(z'). \tag{15}$$

The current distribution along the z' axis which would create the pattern in Fig. 2 is obtained by solving (14) using the Levin method with RKF for $\ell = 8$, $n = 11$, and $m = 2$. The resultant current distribution is shown in Fig. 3 for the antenna length $L = 30\,\lambda$.

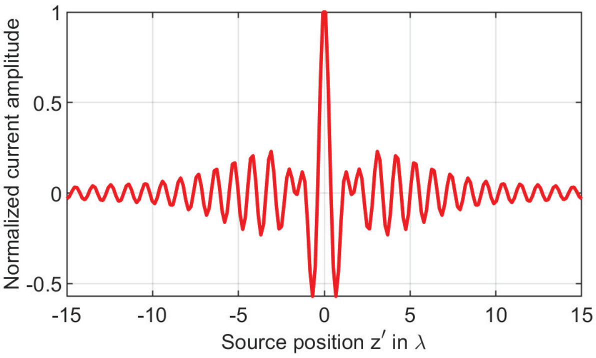

Fig. 3. Normalized current distribution along z', obtained by the Levin method with the RKF ($m = 2$).

C. Validating the results

To analyze the accuracy of the results, the radiation pattern created by this current distribution is evaluated by the Fourier integral

$$f(\theta) = \int_{-L/2}^{L/2} I(z') e^{j\xi z'} dz', \tag{16}$$

where the total antenna length is truncated to $L = 60\,\lambda$. This integral is also highly oscillatory. Therefore, the

Levin method with RKF is reapplied. Higher accuracy is achieved by using $\ell = 90$ and $n = 3$ to eliminate any errors resulting from this second use of the method. Figure 4 shows the results where the accuracy increases as the number of intervals, ℓ, increases. In all simulations, the RKF is used with $m = 2$.

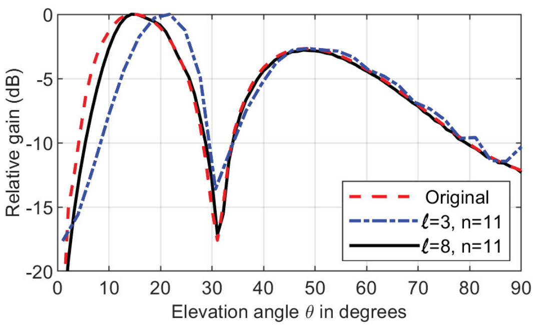

Fig. 4. Radiation pattern due to $I(z')$.

D. Error and stability analysis

In this section, absolute errors and interpolation matrix condition numbers are evaluated for various ℓ and n values. This is achieved by comparing the radiation pattern obtained by the Levin method with the RKF and the original pattern. Furthermore, the results are compared with the "monomial" and the "radial Gaussian" basis functions, both of which are used extensively with the Levin method [4, 10], particularly when polynomial or polynomial spline approximations are used.

The monomial basis functions are defined as

$$u_k(x) = x^{k-1},\ k = 1,2,...,n, \tag{17}$$

and in general, monomial kernels in Levin's method yield very good accuracy with poor condition numbers at increased number of collocation points.

Another type of basis functions, used successfully with Levin's method, is the radial Gaussian functions. These functions are defined as [4]

$$u_k(x) = e^{\frac{-r^2}{\varepsilon^2}}, \tag{18}$$

where the radial term $r = x - x_k$ for $k = 1,2,...,n$, which typically coincide with the collocation points. Additionally, the constant term ε is called the "shape parameter" and is evaluated using the algorithm given in [7]. The radial Gaussian functions also yield good accuracy and stability even at an increased number of collation points. The increased stability is a result of the fact that the interpolation matrix becomes banded by radial functions with pre-defined shape parameters.

The error and stability analysis results are shown in Figs. 5 (a) and (b), respectively. In part a, the absolute error for the radiation pattern function is plotted using the Levin method with the RKF with respect to the collocation points $n = \{3,6,11\}$. Four different graphs are obtained for each part, corresponding to the number of intervals, $\ell = \{3,4,8,12\}$. In part b, the interpolation matrix condition numbers are plotted in decibels. In these simulations, the reproducing kernel function, $K^m(x,y)$, is used with $m = 2$.

Figure 5 shows that when the RKF is used for the same value of m, the error and stability decrease with an increased number of intervals ℓ and the number of collocation points n.

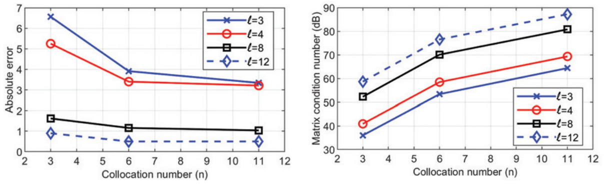

(a) (b)

Fig. 5. (a) Error, (b) stability analysis using the RKF, $K^m(x,y)$, for $m = 2$.

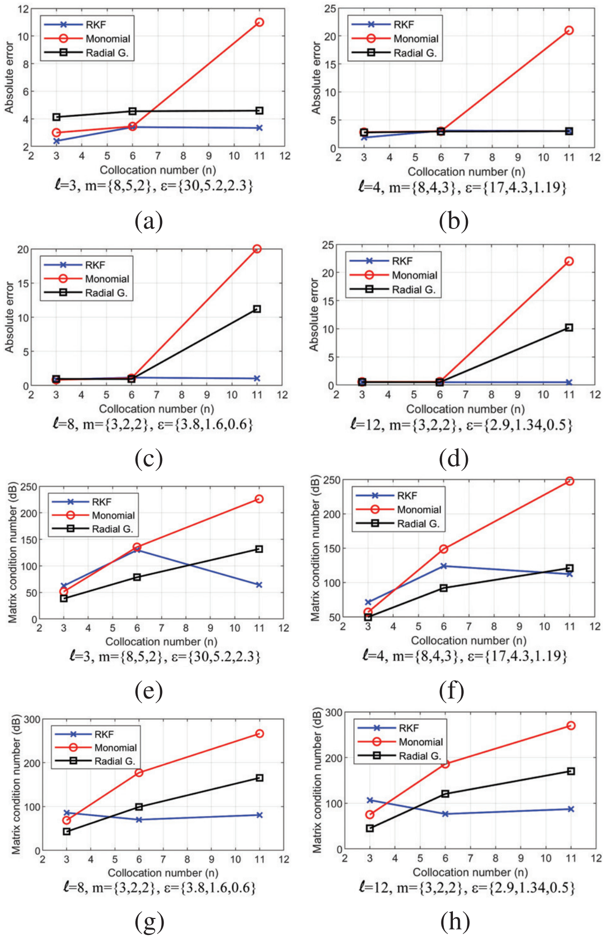

ℓ=3, m={8,5,2}, ε={30,5.2,2.3}
(a)

ℓ=4, m={8,4,3}, ε={17,4.3,1.19}
(b)

ℓ=8, m={3,2,2}, ε={3.8,1.6,0.6}
(c)

ℓ=12, m={3,2,2}, ε={2.9,1.34,0.5}
(d)

ℓ=3, m={8,5,2}, ε={30,5.2,2.3}
(e)

ℓ=4, m={8,4,3}, ε={17,4.3,1.19}
(f)

ℓ=8, m={3,2,2}, ε={3.8,1.6,0.6}
(g)

ℓ=12, m={3,2,2}, ε={2.9,1.34,0.5}
(h)

Fig. 6. Error and stability analysis results at $\ell = \{3,4,8,12\}$. m and ε values are given with respect to the collocation numbers $n = \{3,6,11\}$.

Comparison of the RKF with the monomial and the radial Gaussian basis functions are shown in Fig. 6. In parts a-d and e-h, the absolute errors and the matrix condition numbers are plotted for $\ell = \{3, 4, 8, 12\}$ respectively. In these simulations, the reproducing kernel function, $K^m(x, y)$, is used with the m values that yield the most accurate results. In general, the accuracy of the Levin method with RKF increases with increasing m; however, after a threshold, it starts to decreases because of the high condition number of the interpolation matrix.

In Fig. 6, when the three basis functions are compared, the error is the smallest for the RKF when the optimum values for m are used. Furthermore, RKF has the highest stability as the order of the approximation, n, increases.

The accuracy and stability of the RKF against the other functions for different values of m are presented in Tables 1 and 2, respectively. It can be seen that for a small number of intervals in the integration domain, i.e., $\ell = 3$, it is suitable to use $m = \{8, 5, 2\}$ for $n = \{3, 6, 11\}$. On the other hand, for $\ell \geq 8$, $m = \{3, 2, 2\}$ can be used for the best accuracy.

Table 1: Absolute errors for $n = \{3, 6, 11\}$

Functions	$\boldsymbol{\ell = 3}$	$\boldsymbol{\ell = 8}$	$\boldsymbol{\ell = 12}$
Monomial	3.0, 3.4, 11	0.8, 1.0, 20	0.6, 0.6, 22
Rad. G.	4.1, 4.5, 4.6	1.0, 0.9, 11	0.5, 0.5, 10
RKF, m=2	6.5, 3.9, 3.3	1.6, 1.1, 1.0	0.9, 0.5, 0.5
RKF, m=3	3.0, 3.7, 3.4	0.8, 1.6, 1.1	0.5, 0.6, 0.8
RKF, m=4	2.7, 3.8, 3.5	0.9, 2.5, 14	0.5, 12, 12
RKF, m=5	2.6, 3.4, 7.9	0.9, 14, 16	0.5, 5.2, 13
RKF, m=8	2.4, 5.4, 8.4	1.0, 11, 10	0.5, 15, 11

Table 2: Interpolation matrix condition numbers for $n = \{3, 6, 11\}$ (note that $eA = 10^A$)

Functions	$\boldsymbol{\ell = 3}$	$\boldsymbol{\ell = 8}$	$\boldsymbol{\ell = 12}$
Monomial	e5, e13, e22	e6, e17, e26	e7, e18, e27
Rad. G.	e3, e7, e13	e4, e9, e16	e4, e12, e17
RKF, m=2	e3, e5, e6	e5, e7, e8	e5, e7, e8
RKF, m=3	e5, e8, e10	e8, e11, e13	e9, e12, e14
RKF, m=4	e5, e10, e13	e9, e15, e17	e10,e16, e17
RKF, m=5	e6, e12, e16	e9, e16, e17	e10,e16, e17
RKF, m=8	e6, e15, e17	e9, e16, e17	e10,e16, e17

V. ANTENNA SYNTHESIS APPLICATION II

In this section, the radiation pattern of a narrow beam antenna is interpolated by cubic splines at 91 points, and the radiation pattern function, $f(\theta)$, is obtained as shown in Fig. 7. The beam is centered at $\theta = 30°$ with a beamwidth of $2.5°$.

This pattern function is then used in the inverse Fourier integral to find the current distribution on an equivalent linear source. Levin's method with RKF is used to solve this integral using $\ell = 12$, $n = 11$, and $m = 2$. The resultant current distribution is shown in Fig. 8 for the antenna length $L = 60\,\lambda$.

This current function is then used in the Fourier integral to obtain the radiation pattern. During this evaluation, a large number of intervals are used to keep the margin of error to a minimum. Thus, from the point of view of the method, only the first integral, to find the current distribution, is taken into account. The radiation pattern found by the second Fourier integral is used to assess the error and stability of the method. The results for $\ell = \{3, 12\}$, $n = 11$, and $m = 2$ are compared against the original pattern in Fig. 7.

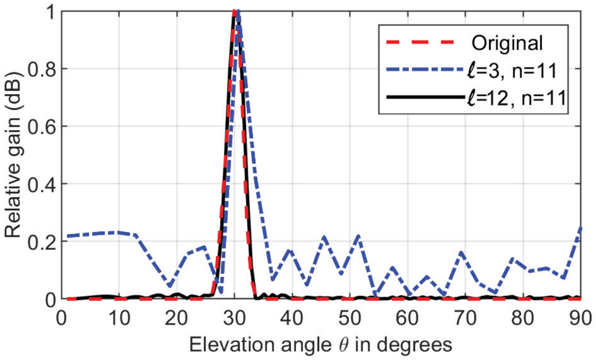

Fig. 7. Narrow-beam antenna radiation pattern.

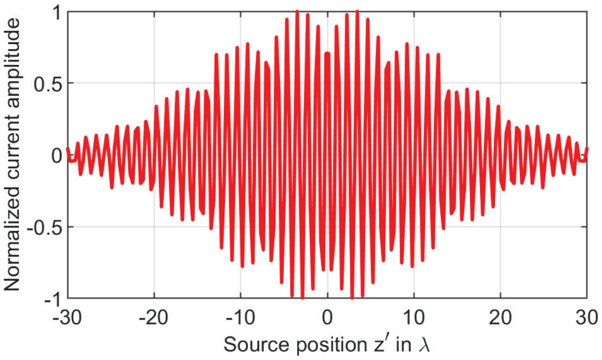

Fig. 8. Narrow beam antenna normalized current distribution.

Comparison of the RKF with the monomial and the radial Gaussian functions are presented in Table 3 in terms of the absolute error. The stability results are the same as in the previous application, given in Table 2.

The results show that for a small number of intervals in the integration domain, i.e., $\ell = 3$, it is suited to use $m = \{8, 5, 4\}$ for $n = \{3, 6, 11\}$. On the other hand, for $\ell \geq 8$, $m = \{3, 2, 2\}$ can be used for the best accuracy.

Table 3: Absolute errors for $n = \{3, 6, 11\}$

Functions	$\boldsymbol{\ell = 3}$	$\boldsymbol{\ell = 8}$	$\boldsymbol{\ell = 12}$
Monomial	5.2, 2.0, 1.8	2.0, 0.9, 12	0.9, 0.3, 30
Rad. G.	5.2, 2.5, 1.4	2.0, 1.2, 0.9	1.0, 0.5, 0.5
RKF, m=2	6.1, 6.8, 7.2	5.3, 3.2, 3.5	1.5, 0.7, 0.3
RKF, m=3	5.3, 2.8, 1.6	2.0, 4.5, 1.4	0.8, 0.6, 0.5
RKF, m=4	5.0, 2.4, 1.4	2.0, 22, 3.8	0.8, 0.4, 13
RKF, m=5	4.8, 2.0, 3.8	2.0, 1.4, 13	0.8, 3.8, 12
RKF, m=8	4.7, 2.4, 10	2.0, 12, 14	0.8, 6.4, 10

VI. CONCLUSION

Levin's method has been used with the RKF in antenna synthesis applications. Based on the results of the examples, the following conclusions are made.

If the radiation pattern is given for $0 \leq \theta \leq 90°$, the number of intervals $\ell = 3$ gives the best results for $m = \{8, 5, 3\}$ corresponding to $n = \{3, 6, 11\}$. The accuracy and stability at these settings are generally greater than the monomial and radial Gaussian functions. Only in a few cases are they equal.

For $\ell = 12$, $m = \{3, 2, 2\}$ or $m = \{3, 3, 2\}$ yields the best results for $n = \{3, 6, 11\}$, respectively. The accuracy and stability at these settings are also generally greater than the monomial and radial Gaussian functions, if not the same. Also, for $\ell > 12$, the simulations have shown similar results to the $\ell = 12$ case regarding accuracy and stability.

For $\ell = 8$, $m = \{3, 2, 2\}$ for $n = \{3, 6, 11\}$ is the single setting that produces the most accurate results in both examples. However, the accuracy and stability in these settings are generally equal to or less than the monomial and the radial Gaussian functions. One must use the optimum m values to get more accurate results.

As a result, Levin's method with RKF is suitable for antenna synthesis applications providing better accuracy and stability, in most cases, than the other known kernels, such as the monomial and radial Gaussian functions, specifically for small or large numbers of intervals, i.e., $\ell = 3$ or $\ell \geq 12$.

REFERENCES

[1] C. A. Balanis, *Antenna Theory*, New York, John-Wiley and Sons, 1997.

[2] O. M. Bucci, G. D'Elia, G. Mazzarella and G. Panariello, "Antenna pattern synthesis: a new general approach," *Proceedings of the IEEE*, vol. 82, no. 3, pp. 358-371, 1994.

[3] G. A. Evans and J. R. Webster, "A comparison of some methods for the evaluation of highly oscillatory integrals," *Journal of Computational and Applied Mathematics*, vol. 112, no. 1-2, pp. 55-69, Nov. 1999.

[4] S. Khan, S. Zaman, A. Arama, and M. Arshad, "On the evaluation of highly oscillatory integrals with high frequency," *Engineering Analysis with Boundary Elements*, vol. 121, pp. 116-125, Dec. 2020.

[5] A. Isarles and S. P. Norsett, "Efficient quadrature of highly oscillatory integrals using derivatives," *Mathematical, Physical and Engineering Sciences*, vol. 461, pp. 1-14, May 2005.

[6] S. U. Islam, I. Aziz, and W. Khan, "Numerical integration of multi-dimensional highly oscillatory, gentle oscillatory and non-oscillatory integrands based on wavelets and radial basis functions," *Engineering Analysis with Boundary Elements*, vol. 36, no. 8, pp. 1284-1295, Aug. 2012.

[7] S. U. Islam, A. S. Al-Fhaid, and S. Zaman, "Meshless and wavelets based complex quadrature of highly oscillatory integrals and the integrals with stationary points," *Engineering Analysis with Boundary Elements*, vol. 37, no. 9, pp. 1136-1144, Sep. 2013.

[8] S. U. Islam and S. Zaman, "New quadrature rules for highly oscillatory integrals with stationary points," *Journal of Computational and Applied Mathematics*, vol. 278, pp. 75-89, April 2015.

[9] S. Zaman, S. Khan and S. U. Islam, "An accurate computation of highly oscillatory integrals with critical points," *Journal of Mathematics*, vol. 50, no. 4, pp. 105-118, 2018.

[10] D. Levin, "Procedures for computing one- and two-dimensional integrals of functions with rapid irregular oscillations," *Mathematics of Computation*, vol. 38, no. 158, pp. 531-538, April 1982.

[11] M. Uddin, Z. Minullah, A. Ali, and Kamran, "On the local kernel-based approximation of highly oscillatory integrals," *Miskolc Mathematical Notes*, vol. 16, no. 2, pp. 1253-1264, March 2015.

[12] H. Brunner, *Collocation Methods for Volterra Integral and Related Functional Equations*, New York, Cambridge University Press, 2004.

[13] Z. C. Li, T. T. Lu, H. Y. Hu, and A. H. D. Cheng, *Trefftz and Collacation Methods*, Wit Press, 2008.

[14] S. Khan, S. Zaman, M. Arshad, H. Kang, H. H. Shah and A. Issakhov, "A well-conditioned and efficient Levin method for highly oscillatory integrals with compactly supported radial basis functions," *Engineering Analysis with Boundary Elements*, vol. 131, no. 8, pp. 51-63, Oct. 2021.

[15] R. Schaback and H. Wendland, "Using compactly supported radial basis functions to solve partial differential equations," *Transactions on Modelling and Simulation*, vol. 22, pp. 311-323, 1999.

[16] F. Z. Geng and X. Y. Wu, "Reproducing kernel function-based Filon and Levin methods for

solving highly oscillatory integral," *Applied Mathematics and Computation*, vol. 397, May 2021.

[17] L. Xiuying and W. Boying, "A new reproducing kernel method for variable order fractional boundary value problems for functional differential equations," *Journal of Computational and Applied Mathematics*, vol. 311, pp. 387-393, Feb. 2017.

[18] F. Z. Geng and S. P. Qian, "Modified reproducing kernel method for singularly perturbed boundary value problems with a delay," *Applied Mathematical Modelling*, vol. 39, no. 18, pp. 5592-5597, Sept. 2015.

[19] O. Baver, *Reproducing Kernel Hilbert Spaces,* M.S. dissertation, Bilkent University, Aug. 2005.

[20] L. Wasserman, *Function Spaces Lecture Notes,* Department of Statistics and Data Science, Carnegie Mellon University, pp. 1-15.

[21] Giovannini Elettromeccanica, "HF Log-periodic Antenna 4 to 30 MHz Mod. 4030/LP/10, 4030/LP/2," [Online] https://www.antenna.it/military/images

Goker Sener was born in 1973. He completed his B.S. in electrical engineering in 1995 at the Wright State University, Dayton, OH. He completed his M.S. and Ph.D. in electrical and electronics engineering in 2004 and 2011 at the Middle East Technical University, Ankara, Turkey. He is currently an assistant professor at Cankaya University Electrical Electronics Engineering Department, Ankara, Turkey. His fields of interest are electromagnetic theory and antennas.

Analysis and Design of Broadband OAM Array Antenna

Yunqi Zhang, Shiliu Zhao, Xuping Li, and Leying Wang

School of Electronic Engineering
Xi'an University of Posts & Telecommunications, Xi'an, 710121, China
johnny_5@126.com, 2804343032@qq.com, lixuping@163.com, 909650203 @qq.com

***Abstract* –**This paper presents a Uniform Circular Array (UCA) antenna of crossed-dipole that can excite vortex waves in a wide frequency range from 3.5 GHz to 8.4 GHz. In the design process, the theoretical derivation of the influence on the Orbital Angular Momentum (OAM) when the antenna elements are arrayed in Co-directional Antenna Array (CAA) and Rotational Antenna Array (RAA) is given respectively. The fixed mode of the dipoles CAA is achieved by feeding each element with equal amplitude and 90° phase difference produced by the broadband feeding network. Furthermore, the proposed broadband OAM array antenna has been fabricated and measured to verify the predicted properties. The vortex electromagnetic wave with +1 mode could be excited in the bandwidth of 82.35%. Simulated and measured results are in good agreement. The proposed OAM array antenna is simple in design principle, compact in structure and low in profile, making this array antenna an excellent candidate for broadband OAM communication systems.

***Index Terms* –** Broadband, CAA, OAM, RAA, uniform circular array antenna.

I. INTRODUCTION

Due to the enormous growth in the number of wireless devices and the steadily increasing demands brought on by wireless applications, spectrum has recently been a barrier for network capacity. Although multiple input multiple output (MIMO) technology can offer numerous channels to boost data-carrying capacity, it also requires the device to use more power. In addition, the introduction of higher-order modulation and more channels of MIMO mean that the receiver has higher requirements on the signal-to-noise ratio of the wireless channel, which reduces the coverage and the anti-interference degree of the device [1]. The fundamental basis of orthogonal frequency division multiple access (OFDMA) lies in how to allocate available bandwidth resources to users more effectively and optimally, without widening the spectrum in the meantime [2]. Therefore, the most direct and effective way to increase capacity is to expand the bandwidth and increase the spectrum resources. The broadband vortex electromagnetic wave has many advantages, such as large communication capacity, good confidentiality, and strong anti-multipath interference ability. Moreover, it presents a new degree of freedom as a result of carrying orbital angular momentum (OAM). With this new electromagnetic advantage, channel capacity issues and low spectrum consumption can be resolved.

Compared with microstrip reflect array [3], shaped vortex antenna [4], resonant cavity antenna [5], metasurface antenna [6], etc., the principle of the array antenna to generate vortex electromagnetic waves is simple, the structure is flexible, and the unit forms are various [7]. Most importantly, the array antenna could generate vortex electromagnetic waves with different modes in a wide frequency range. Array antennas with microstrip patch as units for OAM applications have the characteristics of low profile and low cost [8–10]. For dual full-duplex applications, the multilayer dual-ring UCA realizes the generation of dual OAM modes with low interunit coupling. However, its operation bandwidth is narrow, with only 21.3% (13.5 GHz∼16.7 GHz) [8]. A two-looped concentric uniform circular array is designed for multiplex beams of OAM. Although the sequential rotation of the circularly polarized antenna is used to avoid the use of the feeding network, the operation bandwidth is only 8.7% [9]. A mode-reconfigurable wideband OAM patch array antenna is realized by adopting p-i-n didoes in the feed network. Both the polarization and the OAM modes of the 2×2 array can be reconfigurable in the frequency band range of 2.21 GHz∼2.73 GHz (21%) [10].

Dipole array antennas have also been widely used in the excitation of vortex electromagnetic waves to expand the OAM bandwidth. In 2017, a broadband (2.1 GHz∼2.7 GHz, bandwidth of 25%) 2×2 array with dual-polarized and dual OAM modes has been realized by adopting the bowtie dipole array [11]. The closed-loop cross-dipole antenna array in the literature [12] can cover an ultra-wide frequency band from 2.08 GHz to 3.95 GHz (62.02%), using several pillow-like parasitic patches and a hybrid wideband feeding network. But the antenna structure is complex and the OAM mode purity

Submitted On: November 7, 2022
Accepted On: September 7, 2023

https://doi.org/10.13052/2023.ACES.J.380704

1054-4887 © ACES

needs to be improved. In 2021, a broadband magneto-electric dipole array antenna was proposed for OAM applications, which could generate ±1 and ±2 modes from 5 GHz to 10.3 GHz (69.3%). But the bandwidth is obtained under ideal feeding conditions [13]. In addition, array antennas with different array element forms are also proposed to generate vortex electromagnetic waves, such as Vivaldi antenna [14], horn antenna [15], single arm helical antenna [16], etc.

In this letter, a wideband uniform circular array under the CAA arrangement is studied and developed for broadband OAM communication systems. To better understand the generation mechanism of vortex electromagnetic waves, the array factors for both RAA and CAA have been analyzed. Moreover, a wideband crossed-dipole and phase shifter are introduced to expand the bandwidth. Calculations, simulations, and measurements demonstrate that the antenna can successfully excite vortex electromagnetic waves with mode of +1 in the range of 3.5 GHz to 8.4 GHz (82.35%).

II. DERIVATION AND VERIFICATION

A. Analysis of array arrangement

According to the pattern product theorem of the array antenna, the pattern generated by N isotropic array elements is equal to the product of the element factor and the array factor [17], namely

$$F(\theta,\phi)=F_{\mathrm{e}}(\theta,\phi)\times f_a(\theta,\phi).$$

The unit factor $F_e(\theta,\varphi)$ is related to the form of the unit, and the array factor $f_a(\theta,\varphi)$ is related to the arrangement of the array and the amplitude and phase of the unit excitation signal. As array characteristics, the vortex electromagnetic wave can be focused on the array factor term. The two array arrangements in Fig. 1 belong to the category of uniform circular array antenna. On the *xoy* plane, N cells are evenly and equally spaced on a circle with a radius of R. The relative position of the *nth* unit is (x_n, y_n), and the angle with the x-axis is φ_n, Taking the appropriate position as the observation surface, the electric field vector of the *nth* unit at the point $P(r,\ \theta,\ \varphi)$ on the observation surface can be formulated as:

$$E_{\mathrm{n}}=C\times I_{\mathrm{n}}\times\frac{e^{-jkR_n}}{R_n}=C\times I_{\mathrm{n}}\times\frac{e^{-jkr}}{r}\times e^{-jk(R_n-r)}. \quad (1)$$

Among them, C is a constant term; I_n denotes the excitation signal of each unit; R_n is the vertical distance from the observation point P to the *nth* cell. Here, I_n includes the phase signal α_n and the amplitude signal A_n. The value of the angular beam k is $2\pi/\lambda$. According to the unit position vector and the electric field superposition principle, the total electric field vector of the array antenna is calculated as follows:

$$E=\sum_{n=1}^{N}=C\times\frac{e^{-jkr}}{r}\sum_{n=1}^{N}I_n\times e^{j[ka\sin\theta\cos(\phi-\phi_n)+a_n]}$$
$$=C\times\frac{e^{-jkr}}{r}\times f_a(\theta,\phi). \quad (2)$$

According to (2), it can be seen that the array factor can be expressed as follows:

$$f_a(\theta,\phi)=\sum_{n=1}^{N}I_n\times e^{j[ka\sin\theta\cos(\phi-\phi_n)+a_n]}, \quad (3)$$

where α_n is the final phase value of the *nth* element. The initial phase difference between adjacent array elements is denoted as $\Delta\alpha_0$ and the number of modes excited by the array as l, also known as the topological charge. Then, $\alpha_n=\Delta\alpha_0+2\pi nl/N$. Bringing α_n into (3), $f_a(\theta,\ \varphi)$ can be rewritten as follows:

$$f_a(\theta,\phi)=\sum_{n=1}^{N}I_n\times e^{j[ka\sin\theta\cos(\phi-\phi_n)+\Delta a_0+\frac{2\pi l}{N}\mathrm{n}]}. \quad (4)$$

When N tends to infinity, the summation should be considered the integral of the variable φ, then (4) can be obtained as follows:

$$f_a(\theta,\phi)=\frac{N\mathrm{e}^{\mathrm{j}l\varphi}}{2\pi}\int_0^{2\pi}e^{j[ka\sin\theta(\varphi-\phi)+\imath(\varphi-\phi)]}d(\varphi-\phi). \quad (5)$$

Writing (5) as a Bessel function form of the first kind, an optimization formula after simplification could be expressed as follows:

$$f_a(\theta,\phi)=Nj^{-\imath}\mathrm{e}^{\mathrm{j}l\varphi}J_\imath(ka\sin\theta). \quad (6)$$

It can be seen from (6) that the field strength of the far field contains a helical phase factor $e^{jl\varphi}$, which means that a vortex electromagnetic wave with a topological charge of l is generated.

Array units with different polarization and arrays with different arrangements have a great influence on the OAM performance. For a circularly polarized unit, there are two ways to form an array: One is that the unit be translated into array, named the co-directional antenna array (CAA); the other is that the unit be rotated into an array, called the rotational antenna array (RAA). Figure 1 depicts the excitation principle of vortex waves in different arrays of the same circularly polarized unit.

The chamfered structure is adopted for the array unit to achieve right-handed circular polarization characteristics, and each component of the electric field vector is given in Fig. 1. For CAA, as depicted in Fig. 1 (a), the magnitudes and orientations of the electric field in the X and Y components of each unit are the same, the magnitude in the x direction is 90°, and the orientation is the +x direction; the magnitude in the y direction is 0°, and the orientation is the +y direction. Therefore, it can be considered that the initial phase difference $\Delta\alpha_0$ between adjacent elements of the CAA is 0°. If the *nth* unit of the array is fed with an equal step phase delay ($2\pi nl/N$)

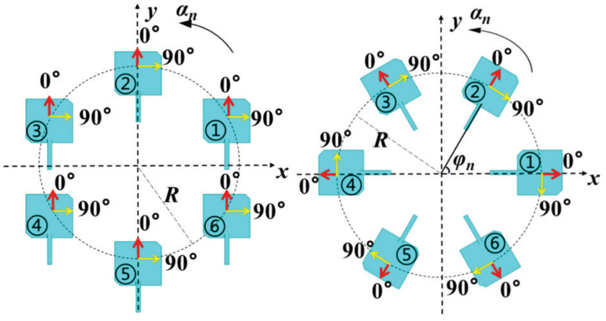

(a) (b)

Fig. 1. OAM array antennas in different arrangements: (a) CAA (unit translation), (b) RAA (unit rotation).

between the elements, the OAM wave with a mode number of *l* can be successfully excited.

For RAA, as depicted in Fig. 1 (b), the electric field characteristics of the array elements in the back-to-back structure are opposite because the change of the element handedness leads to the change of the electric field size and orientation of each element in the *X* and *Y* components, respectively. Therefore, as analyzed in Fig. 1 (b), the theoretical modal values are no longer equal to the modal values produced by the model. The antenna rotates counter-clockwise, so the angle β_n between the electric field vector of the nth element and the +*x* axis is $2\pi(n-1)/N$, then the initial phase difference between adjacent elements of the RAA $\Delta\alpha_0 = \beta_n - \beta_{n-1}$ is no longer 0°, but $2\pi/N$. At this time, the electric field phase delay of the unit can be caused by rotating the antenna. From this, it can be concluded that the phase difference caused by the rotation of the antenna in the RAA is equivalent to the phase difference caused by applying current excitation in the CAA.

B. Simulation

The two structures in Fig. 1 are employed for additional simulation verification in accordance with the theoretical analysis mentioned above. Both antennas are fed by wave port excitation; the radius *R* of the array is about 0.6λ. A square plane with a distance of 1000 mm above the array antenna is selected as the observation area, and the component (*x* or *y*) in the same direction must be guaranteed for sampling. The only variation between CAA and RAA is the array elements' various orientations. The simulation results of wavefront phase distribution in different arrangement modes are illustrated in Fig. 2. As seen, both CAA and RAA with six units are capable of producing electromagnetic vortices in the OAM modes of ±1, ±2, and ±3.

The wavefront phase distribution is calculated by collecting the phase value of each point on the wavefront plane, which is a square with sides 800 mm. Furthermore, the wavefront plane should be perpendicular to the radiation direction of the OAM array antenna. As depicted in Fig. 2 (a), the wavefront phase distribution corresponds to the OAM simulation results of CAA, and Fig. 2 (b) corresponds to that of RAA.

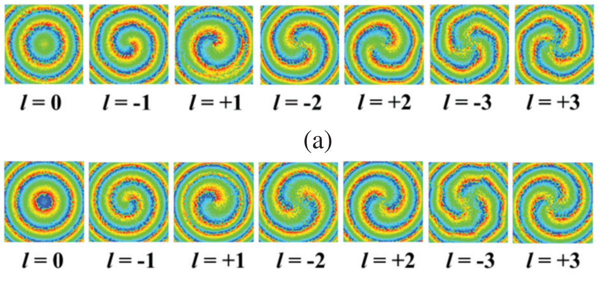

(a) (b)

Fig. 2. Simulated phase distribution of array antenna under different arrangements: (a) CA, (b) RAA.

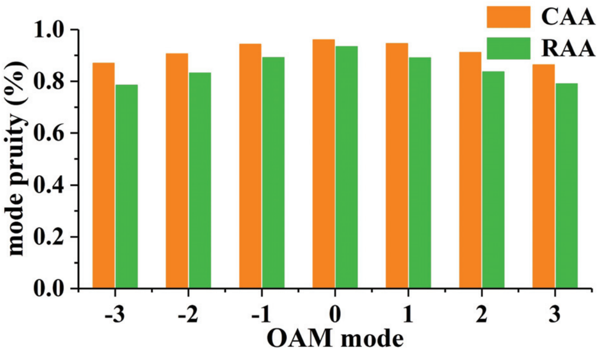

Fig. 3. Comparison of the mode purity between CAA and RAA in different OAM modes.

Obviously, the phase distributions of CAA and RAA depicted in Fig. 2 are slightly different, which is due to the array scheme being able to affect the OAM mode purity. For further clarification on the influence of different arrangements, mode purity has been calculated. Figure 3 compares the OAM mode purity of the CAA and RAA in different modes, and the purity of the vortex waves excited by the CAA is higher than that of the same vortex waves generated by the RAA [18]. Therefore, to generate broadband OAM with higher purity, the CAA arrangement is adopted in the following design.

III. BROADBAND OAM ANTENNA

A. Array design

In order to achieve broadband OAM characteristics, the crossed dipole with a single asymmetrical cross-loop is adopted as the array unit [19]. The simulated results of this unit are depicted in Fig. 4. As seen, the crossed dipole antenna performs a -10 dB impedance bandwidth

(IBW) of 47.51% (3.45∼5.60 GHz), and the axial ratio bandwidth (ARBW) of 61.51% (3.31∼6.25 GHz), which meet the request of the broadband OAM array antenna.

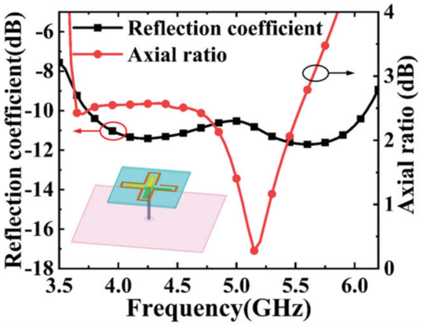

Fig. 4. Simulated reflection coefficient and axial ratio of the crossed dipoles.

The configuration and geometric size of the proposed broadband OAM array antenna are illustrated in Fig. 5. This array antenna consists of four crossed dipoles arrayed in CAA and a broadband feeding network with 90° clockwise phase difference. As shown in Fig. 5 (a), these four units are printed on the top layer of substrate 1, and the feeding network is printed on the bottom layer of substrate 2. To save processing cost, the dielectric substrates used in the proposed antenna array are the same, both of which are FR4 materials (ε_r = 4.4) with thickness of 0.8 mm.

Taking into account the excitation principle of vortex waves and the integrity of the array antenna structure, a broadband feeding network is designed, as depicted in Fig. 5 (b). The feeding network includes an input port with impedance of 50 Ω and four output ports arranged in the clockwise direction. A 180° phase shifter and two 90° phase shifters are cascaded to form the broadband feeding network. The broadband phase shifter for both 90° and 180° can be equivalent to the three-port device shown in Fig. 5 (b). After passing through the three-port device, one signal is divided into two signals with equal amplitude and phase difference of 90° or 180°.

The proposed planar balun shown in Fig. 5 (b) is composed of a wide-band Wilkinson power divider, a microstrip line with two branches, and an N-shaped impedance transformation section with 90° or 180° phase delay. Among them, the 100 Ω isolation resistor, which plays the role of absorbing echoes and adjusting port isolation, is welded to the Wilkinson power divider. These two branches are an open circuit branch and a short circuit branch connected to a via hole on the ground to realize a short circuit [20]. The amplitude and phase imbalance are stable within a wide operation band.

Figure 6 depicts the simulated reflection coefficient and the phase imbalance results of the feeding network.

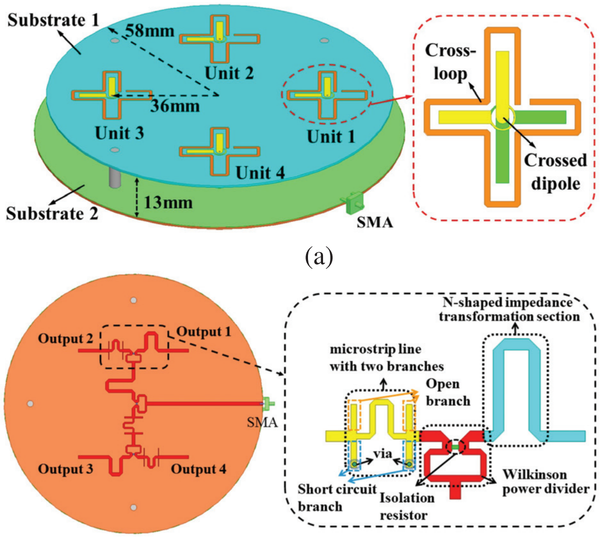

Fig. 5. Configuration of the broadband OAM array antenna: (a) 3D view, (b) feeding network.

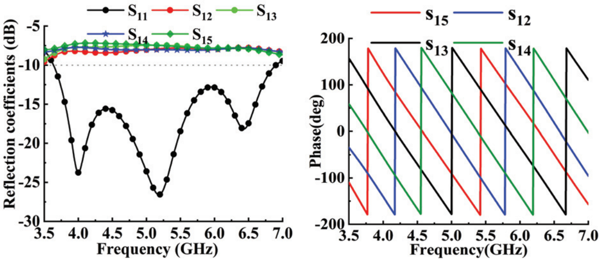

(a) (b)

Fig. 6. Simulated results of the broadband feeding network: (a) Reflection coefficient, (b) phase shift.

It can be seen from Fig. 6 (a) that the return loss is less than -10 dB in the frequency range of 3.63 GHz∼6.90 GHz or 62.1%. Additionally, S_{12}, S_{13}, S_{14}, and S_{15} are relatively stable, and the maximum amplitude difference between the four output ports does not exceed 1 dB. Figure 6 (b) illustrates that these output phase imbalances of the feeding network are stable within the operation band, and the maximum phase difference of the four signals is less than ±3°. Therefore, the feeding network has good performance, which provides a good guarantee for the broadband feeding of the CAA.

B. Results and discussions

The processed wide-band OAM array antenna and feeding network are assembled, and nylon columns are used to support the upper and lower dielectric substrates. As the signal input end, a 50 Ω claw-shaped SMA connector is soldered to the end of the microstrip line. Photographs of the near-field measuring environment

Table 1: Comparison between reported works and proposed antenna

Ref.	Type of Unit	Number of Units	Arrangement	Number of Ports	Bandwidth
[6]	Aperture-coupled antenna	24	CAA+RAA	1	21.3% (13.5∼16.7 GHz)
[7]	Triangle patch antenna	12	RAA	2	8.7% (8.8∼9.6 GHz)
[8]	Circular patch antenna	4	RAA	1	21% (2.21∼2.73 GHz)
[9]	Bowtie dipole	4	RAA	2	25% (2.1∼2.7 GHz)
[10]	Closed-loop dipole	4	RAA	1	66.9% (2.05∼4.11 GHz)
This work	Crossed-dipole	4	CAA	1	82.35% (3.5∼8.4 GHz)

and the antenna's physical composition are shown in Fig. 7. The antenna was measured in an anechoic chamber. And a broadband receiving antenna on the 3D scanning platform is used to collect the amplitude and phase in the near field. The sampling distance varies from 430 mm (3.5 GHz) to 180 mm (8.4 GHz).

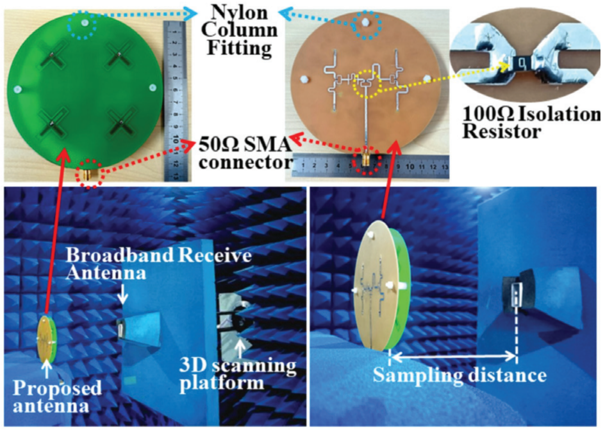

Fig. 7. Fabricated prototype of broadband OAM array antenna, and its measurement environment.

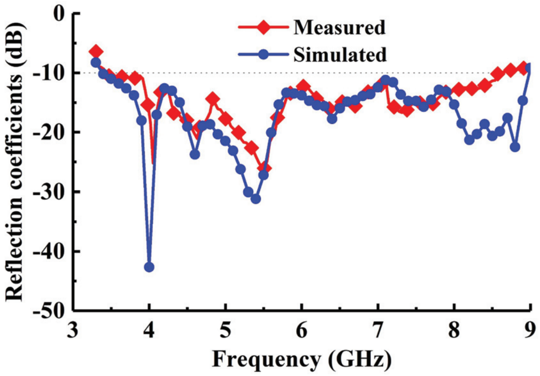

Fig. 8. Comparison of simulated results and measured results of reflection coefficient.

The S parameters of the antenna were measured with the vector network analyzer (Ceyear 3635D). Additionally, the results of simulation and measurement are plotted in Fig. 8. As seen, these two curves are quite consistent across most frequency ranges, and the measured results degrade as frequency increases. The test inaccuracy results from the FR4 dielectric substrate's evident shift in relative dielectric constant with frequency. In addition, machining and welding processes also cause inevitable errors in simulation and measured results. Overall, the consistency between the two is good, and the measured bandwidth essentially agrees with the outcomes of the simulation. It is evident that the bandwidth is greater than that of comparable broadband array antennas and that the -10 dB IBW is 82.35% (3.5-8.4 GHz). A comprehensive comparison with reported works is further conducted, as summarized in Table 1. It shows that the proposed antenna realizes the broadband OAM with fewer units and compact arrangement. It also proves that the analysis of CAA and RAA in section II are effective to the design of the OAM array antenna.

The distance between the probe and the proposed antenna changes continuously with the change of the test frequency. The fixed scanning range of the wave-front plane is $6\lambda_0 \times 6\lambda_0$, where λ_0 is the free-space wavelength at the center frequency. And the sampling grid period is 25 mm. In order to prove the broadband OAM characters, the sampling frequency takes 0.9 GHz equally spaced steps, followed by 3.5 GHz, 4.4 GHz, 5.3 GHz, 6.2 GHz, 7.1 GHz, 8 GHz, and 8.4 GHz. Figure 9 compares the simulated and measured wave-front phase

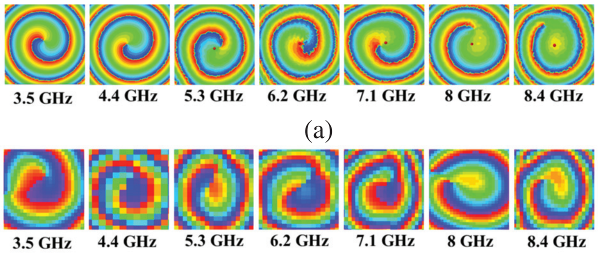

(a)

(b)

Fig. 9. Simulated and measured results of wave-front phase distribution at different frequency points: (a) the simulated results, (b) the measured results.

distribution of the broadband OAM array antenna in near field at different frequency points. Figure 9 (a) illustrates the OAM phase distribution diagram on the X component. The wave front phase diagram of each frequency point has a clear rotation direction, and it is a curve rotating counter-clockwise, which means the vortex electromagnetic beam with mode +1. Figure 9 (b) depicts the measured results in the near field. It can be seen that the measured results of each frequency point are in good agreement with the simulated ones. The OAM vortex characteristics at different frequency points can be clearly observed from the theoretical simulated and measured results. Therefore, the proposed broadband OAM array antenna successfully excited the OAM beam with mode +1 in the frequency range of 3.5 GHz to 8.4 GHz.

To further demonstrate the effectiveness of the design method, the simulated and measured OAM mode purity of each frequency point is plotted in Fig. 10. The main mode of the proposed antenna is +1, and the purity is over 70% within the whole operation band. It is clear that the wide operation band, high OAM mode purity, compact structure size, and low profile of the proposed antenna exhibit comprehensive advantages.

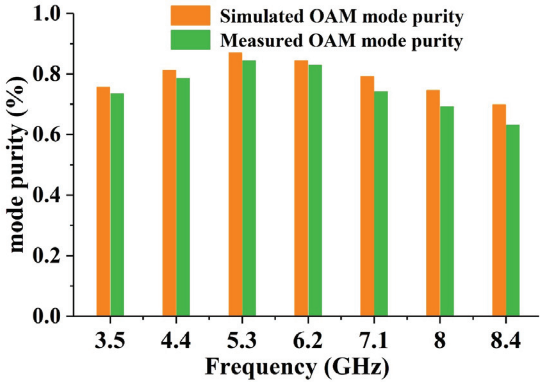

Fig. 10. Simulated and measured OAM mode purity at different frequency points.

IV. CONCLUSION

In this paper, the effects of uniform circular array antennas on vortex electromagnetic waves are analyzed with the units placed in different ways. Compared with the RAA, the CAA arrangement has the advantages of simple principle, easy design, and high purity of excited vortex electromagnetic waves. Furthermore, in order to widen the spectrum resources, a broadband OAM uniform circular array antenna is designed, fabricated, and measured. The simulation and experimental results show that it exhibits obvious and stable vortex wave characteristics in the wide frequency band of 3.5∼8.4 GHz. The proposed broadband OAM array antenna has broad application prospects in underwater short-range communication, radar imaging, and so on.

ACKNOWLEDGMENTS

This work is supported in part by Key Research and Development Program of Shaanxi (Program No. 2021GY-049), Scientific Research Program funded by Shaanxi Provincial Education Department (Program No. 22JC058), and Xi'an Science and Technology Plan Project under Grant 21XJZZ0071.

REFERENCES

[1] N. Jindal, "MIMO broadcast channels with finite-rate feedback," *IEEE Trans. Inf. Theory*, vol. 52, no. 11, pp. 5045-5060, 2006.

[2] M. Ergen, S. Coleri, and P. Varaiya, "QoS aware adaptive resource allocation techniques for fair scheduling in OFDMA based broadband wireless access systems," *IEEE Trans. Broadcast.*, vol. 49, no. 4, pp. 362-370, 2003.

[3] H.-T. Chen, R. Pan, W.-Z. Sun, and S.-Y. Si, "Microstrip reflectarray for generation of electromagnetic waves with beam vorticity," *Applied Computational Electromagnetics Society (ACES) Journal*, vol. 33, no. 5, pp. 488-493, 2018.

[4] X.-N. Hui, S.-L. Zheng, Y. P. Hu, X. Chen, X.-F. Jin, H. Chi, and X.-M. Zhang, "Ultralow reflectivity spiral phase plate for generation of millimeter-wave OAM beam," *IEEE Antennas Wirel. Propag. Lett.*, vol. 14, no.0, pp. 966-969, 2015.

[5] W.-T. Zhang, S.-L. Zheng, X.-N. Hui, Y.-L. Chen, X.-F. Jin, H. Chi, and X.-M. Zhang, "Four-OAM-Mode antenna with traveling-wave ring-slot structure," *IEEE Antennas Wirel. Propag. Lett.*, vol. 16, no. 0, pp. 194-197, 2017.

[6] H. Xu, H. Liu, X. Ling, Y. Sun, and F. Yuan, "Broadband vortex beam generation using multimode pancharatnam–berry metasurface," *IEEE Trans. Antennas Propag.*, vol. 65, no. 12, pp. 7378-7382, 2017.

[7] Y.-L. Zhou, X.-N. Li, K.-Y. Yao, Y.-M. Huang, and H.-Y. Jin, "A topological charge continuously tunable orbital angular momentum (OAM) electromagnetic wave generation method based on fixed-length delay line mixing circuit," *Applied Computational Electromagnetics Society (ACES) Journal*, vol. 37, no. 10, pp. 1071-1076, 2023.

[8] Y. Zhang and J. Li, "An orbital angular momentum-based array for in-band full-duplex communications," *IEEE Antennas Wirel. Propag. Lett.*, vol. 18, no. 3, pp. 417-421, 2019.

[9] T.-Z. Zhang, J. Hu, Q.-Y. Zhang, D. Zhu, Y.-B. Ma, B.-T. Lin, and W. Wu, "A compact multimode OAM antenna using sequentially rotated

configuration," *IEEE Antennas Wirel. Propag. Lett.*, vol. 21, no. 1, pp. 134-138, 2022.

[10] Q. Liu, Z.-N. Chen, Y.-N. Liu, F.-H. Li, Y. Chen, and Z.-G. Mo, "Circular polarization and mode reconfigurable wideband orbital angular momentum patch array antenna," *IEEE Trans. Antennas Propag.*, vol. 66, no. 4, pp. 1796-1804, 2018.

[11] B. Liu, Y. Cui, and R. Li, "A broadband dual-polarized dual-OAM-mode antenna array for OAM communication," *IEEE Antennas Wirel. Propag. Lett.*, vol. 16, no. 0, pp. 744-747, 2017.

[12] Z. Yang, J. Zhou, L. Kang, B. Liu, G. Yang, and X. Shi, "A closed-loop cross-dipole antenna array for wideband OAM communication," *IEEE Antennas Wirel. Propag. Lett.*, vol. 19, no. 12, pp. 2492-2496, 2020.

[13] Z. Li, S. Li, B. Han, G. Huang, L. Cong, and X. Cao, "A broadband magnetic-electric dipole antenna array for OAM generation," *2021 International Conference on Microwave and Millimeter Wave Technology (ICMMT)*, pp. 1-3, 2021.

[14] T. Yang, D. Yang, B. Wang and J. Hu, "Experimentally validated, wideband, compact, OAM antennas based on circular Vivaldi antenna array," *Progress In Electromagnetics Research C*, vol. 80, pp. 211-219, 2018.

[15] K. Liu, H.-Y. Liu, Y.-L. Qin, Y.-Q. Cheng, S.-N. Wang, X. Li, and H.-Q. Wang, "Generation of OAM beams using phased array in the microwave band," *IEEE Trans. Antennas Propag.*, vol. 64, no. 9, pp. 3850-3857, 2016.

[16] L. Li and X.-X. Zhou, "Mechanically reconfigurable single-arm spiral antenna array for generation of broadband circularly polarized orbital angular momentum vortex waves," *Scientific Reports*, vol. 8, no. 1, pp. 1-9, 2018.

[17] Q. Feng, Y.-F. Lin, Y.-S. Zheng, and L. Li, "Vortex beam optimization design of concentric uniform circular array antenna with improved array factor," *Applied Computational Electromagnetics Society (ACES) Journal*, vol. 36, no. 7, pp. 830-837, 2021.

[18] J. Ma, X. Song, Y. Yao, Z. Zheng, X. Gao, and S. Huang, "Research on the purity of orbital angular momentum beam generated by imperfect uniform circular array," *IEEE Antennas Wirel. Propag. Lett.*, vol. 20, no. 6, pp. 968-972, 2021.

[19] G. Feng, L. Chen, X. Xue, and X. Shi, "Broadband circularly polarized crossed-dipole antenna with a single asymmetrical cross-loop," *IEEE Antennas Wirel. Propag. Lett.*, vol. 16, no. 0, pp. 3184-3187, 2017.

[20] Z.-Y. Zhang, Y.-X. Guo, L.-C. Ong, and M. Y. W. Chia, "A new wide-band planar balun on a single-layer PCB," *IEEE Microw. Wireless Compon. Lett.,* vol. 15, no. 6, pp. 416-418, 2005.

Yunqi Zhang was born in BaoTou, Inner Mongolia, China. He received the Master's degree and the Ph.D. degree in micro-electronics from Xidian University in 2012 and 2015, respectively. He is currently working in the Xi'an University of Posts & Telecommunications. His research interests include CP antennas, OAM, omnidirectional antennas, and phase array antennas.

Shiliu Zhao is with the School of Electronic Engineering, Xi'an University of Posts & Telecommunications, Xi'an 710121, China. Her main research interests are array antennas and vortex electromagnetic waves.

Xuping Li was born in Xi'an, Shanxi, China in 1981. He received the Ph.D. degree in electromagnetic fields and microwave technology from Xidian University, Xi'an, China, in 2015. His research interests are antenna theory and engineering.

Leying Wang is with the School of Electronic Engineering, Xi'an University of Posts & Telecommunications, Xi'an 710121, China. Her current research interests include underwater wireless optical communication and signal processing.

A Miniaturized UWB Bandpass Filter Employing Multi-Stub-Loaded Short-Circuited Stepped Impedance Ring Resonator

Guangyong Wei[1], Yunxiu Wang[1*], Jie Liu[2], and Haiping Li[1]

[1]School of Electronic and Information Engineering
China West Normal University, Nanchong, 637009, China
1772478781@qq.com, 627662147@qq.com, 370411361@qq.com
*Corresponding author

[2]School of Physics and Astronomy
China West Normal University, Nanchong, 637009, China
779512555@qq.com

***Abstract* –** This article presents a novel microstrip line topology implementation of an ultra-wideband (UWB) bandpass filter. The proposed topology is a short-circuited stepped-impedance ring resonator with an open-circuit stub and a short-circuit stub loaded at the central vertical position of the low impedance of this resonator, respectively. Within the UWB spectrum, five modes are allocated under weak coupling, and to increase filter selectivity, two transmission zeros are added. It is possible to extend the upper stopband and provide sufficient external coupling by utilizing interdigital-coupled lines. To demonstrate the design theory, a prototype is designed and manufactured on a 0.8 mm thick substrate of the affordable F4B-2, and its performance is verified. Measurements show a 3-dB bandwidth span from 2.8 to 9.5 GHz, insertion loss of 0.36 dB, and return loss better than 13 dB.

***Index Terms* –** Bandpass filter, stepped-impedance resonator (SIR), stub-loaded, ultra-wideband (UWB).

I. INTRODUCTION

One of the essential elements of wireless communication systems that operate in the ultra-wideband (UWB) spectrum is the UWB bandpass filter (BPF). The attention of pertinent scholars has always focused on its properties of low insertion loss and good selectivity since it can simultaneously pick up the anticipated signal and filter out junk. The Federal Communications Commission (FCC) authorized the allocation of unlicensed frequency bands in the range of 3.1-10.6 GHz in 2002 in order to realize several novel commercial communication applications of ultra-wideband (UWB) technology [1]. This encourages UWB BPF [2–3] to thrive in an atmosphere supporting UWB technology. In recent years, a number of approaches for designing UWB BPFs have been put forward.

The cascaded high-low pass filter or the cascaded band-stop and band-pass filter is a straightforward way for designing UWB filters [4–5]. While these filters offer a sufficiently broad stop band, there are a few issues, including a big circuit size and a significant insertion loss. A multimode resonator (MMR) that has a rectangular stepped impedance stub, two open-circuit stubs, and two high-impedance lines for input and output feeders is used to create the UWB filter [6]. A novel MMR made of interdigital-coupled lines that are cascaded and stepped impedance stubs that are loaded with short circuits is also suggested in [7], and UWB filters may be created by implementing it further. [8] proposes a stub-loaded UWB filter based on MMR. In the design, there are three open-circuit stubs: one step impedance stub in the center and two open-circuit stubs in symmetrical places on each side. Stepped impedance stubs enable the construction of two transmission zeros (TZs) and great selectivity. In these publications [9–11], filters with this kind of MMR design are also investigated. These MMR-based filters seek to attain ultra-wideband features by using several resonant modes in a resonant structure. The defect ground structure (DGS) is suggested in [12], which comprises a square ring etched into the ground and a metal film. While the electrical performance is compromised, this design offers improved fractional bandwidth (FBW) and frequency characteristics.

To create UWB filters in [13–14], both step impedance resonators (SIRs) are employed. Wide bandwidth features are achieved by varying the resonant frequency. Nevertheless, [15–16] also use an asymmetric, irregular SIR to produce the BPF. Another method is to employ coplanar waveguide and hybrid microstrip technology [17–18], which requires a substrate with a relatively high dielectric constant and results in lower circuit size. Unfortunately, such BPFs may not have good harmonic rejection. Furthermore, ring resonators are often

Submitted On: June 28, 2023
Accepted On: September 17, 2023

https://doi.org/10.13052/2023.ACES.J.380705

1054-4887 © ACES

used in the construction of UWB filters. To build UWB filters with excellent passband selectivity and broad upper stopband, the square ring resonator utilized in the literature [19] has the benefits of simple construction and good passband performance. In [20], the two ring resonator provides a broader fractional bandwidth for increased channel capacity in addition to enabling a UWB filter with a wide upper rejection band.

In this article, a new design of the UWB bandpass filter is proposed based on the short-circuit stepped-impedance ring resonator. Two types of stubs are put on the short-circuit resonator to produce a quintuple mode. First, the model evolution description of the designed filter is carried out. The resonant properties of this resonator are then analyzed theoretically and accurately using the odd- and even-mode approach. The analysis allows the odd- and even-mode frequencies to be tuned such that they are uniformly distributed across the UWB spectrum. Strong coupling is obtained by feeding the proposed resonator with interdigital-coupled lines at the input and output ports to produce excellent bandwidth. The suggested structure is manufactured on an F4B-2 substrate with a height of 0.8 mm. The relative permittivity (ε_r) is 3.38, and the loss tangent is 0.003. The BPF is fabricated and its measurements are validated.

II. DESIGN EVOLUTION

This section illustrates the structural design evolution of the proposed UWB BPF. Figure 1 depicts four configurations and their corresponding frequency responses. Initially, for better impedance matching, the stepped-impedance ring resonator (SIRR) is fed by a 50 ohm microstrip line at the ports, designated as case 1, as shown in Fig. 1 (a). It provides a wider bandwidth and a deeper attenuation zero. It resonates at 6 GHz and provides good return loss, but the 4-8 GHz passband bandwidth is narrow.

To widen the bandwidth, a short-circuit metallized hole was added to the bottom half of the SIRR, forming a short-circuit SIRR (case 2). Figure 1 (b) shows a wider bandwidth than case 1, but poor insertion loss at the passband edges. Figure 1 (c) shows multiple passband poles but poor return loss.

To adjust the passband cutoff frequencies, short- and open-circuit stubs were added to the upper half of the short-circuit SIRR. The short-circuit stub (case 3) improved the lower cutoff frequency, as shown in Figs. 1 (b) and (c). An open-circuit stub could similarly adjust the upper cutoff frequency, simplified here.

The final filter (case 4), offers a 2.8-9.5 GHz passband, a 108.9% fractional bandwidth at 6.15 GHz, and the attenuation poles are located at $f_{p1} = 3.2$, $f_{p2} = 3.8$, $f_{p3} = 4.2$, $f_{p4} = 6.1$, $f_{p5} = 7.2$, $f_{p6} = 8.3$, and $f_{p7} = 9.2$. Figure 1 (d) shows excellent in-band performance.

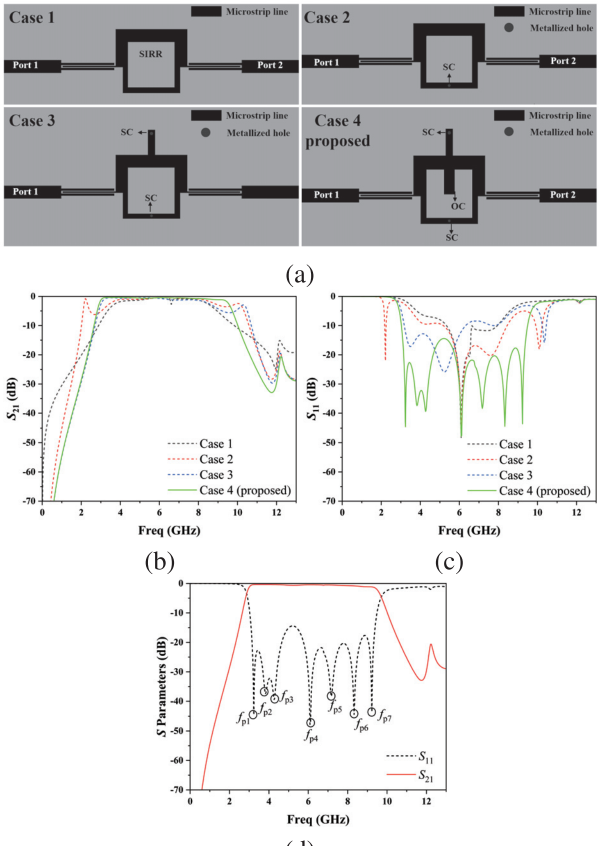

(a)

(b) (c)

(d)

Fig. 1. (a) Evolution layout of the proposed filter, (b) and (c) frequency response for different cases, (d) S-parameter response for case 4.

III. ANALYSIS OF THE PROPOSED UWB FILTER

Figure 2 depicts the structure of the proposed microstrip line UWB-BPF. We introduce a new short-circuit stub-loaded stepped-impedance ring resonator that has been thoroughly analyzed. This innovative design deviates from the traditional ring resonator by integrating a short-circuit stub and an open-circuit stub above the central position of the resonator. Additionally, a metalized hole structure is loaded on the microstrip line beneath its symmetric position. The ring resonator also features a pair of coupled transmission lines on both sides for feeding, each with a length of one-quarter

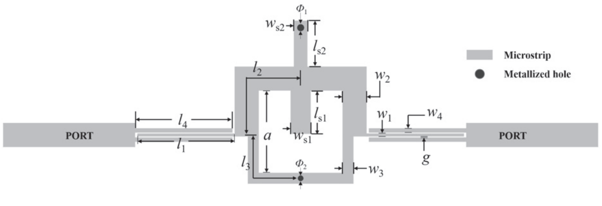

Fig. 2. Architecture of the proposed UWB-BPF.

wavelength (λ_g/4) and admittance Y_1. The resonator is divided into two parts from the horizontal position of the coupled transmission lines. The upper part measures one-half wavelength (λ_g/2) and has admittance Y_2, while the lower part is the same half wavelength (λ_g/2) and has admittance Y_3.

The symmetry of the resonator allows us to utilize the odd- and even-mode approach to study its resonance characteristics, where the odd and even modes can be calculated in the same way as in [21]. Figure 3 illustrates the equivalent transmission line circuit for both odd and even modes. Y_{ino} represents the odd-mode input admittance and Y_{ine} represents the even-mode input admittance. For odd-mode excitation, the odd-mode input admittance can be expressed as

$$Y_{ino} = Y_1 \frac{(Y_{o1}+Y_{o2}) + jY_1 \tan\theta_1}{Y_1 + j(Y_{o1}+Y_{o2})\tan\theta_1}, \tag{1}$$

where

$$Y_{o1}+Y_{o2} = -jY_2 \cot\theta_2 - jY_3 \cot\theta_3. \tag{2}$$

According to the resonance condition Y_{ino} = 0, we can get

$$j(Y_1 \tan\theta_1 - Y_2 \cot\theta_2 - Y_3 \cot\theta_3) = 0. \tag{3}$$

When the even mode is excited, the resonant modes are derived:

$$Y_{ine} = Y_{e1} + Y_{e3} = Y_{e1} - jY_3 \cot\theta_3, \tag{4}$$

where

$$Y_{e1} = Y_2 \frac{j(Y_{s1}/2\tan\theta_1 - Y_{s2}/2\cot\theta_2) + jY_2 \tan\theta_2}{Y_2 - (Y_{s1}/2\tan\theta_1 - Y_{s2}/2\cot\theta_2)\tan\theta_2}. \tag{5}$$

Similarly, the resonance condition Y_{ine} = 0.

Using equations (1)-(5), we can explicitly determine all even- and odd-mode resonant frequencies. Equations (3) and (5) reveal that θ_{s1} and θ_{s2} (or l_{s1} and l_{s2}) solely impact the even-mode frequencies and do not affect the odd-mode frequencies.

Where $\theta = 2\pi f = \beta l$, the electrical length ratio: $\theta_{\text{s1}}/\theta_1 = l_{\text{s1}}/l_1$, $\theta_{\text{s2}}/\theta_1 = l_{\text{s2}}/l_1$. According to the designed center frequency f_{c} = 6.85 GHz and the effective dielectric constant of the substrate, it is easy to determine that the value of l_1 is λ_g/4 (λ_g is the guided wave wavelength at the f_{c}). Therefore the physical length is chosen to be 7.4 mm. Assume here that the width of w_1 is 0.2 mm, then Z_1 = 127.4 Ω. According to [22], it can be determined that the impedance values of Z_2 and Z_3 are 50.3 Ω and 77.8 Ω, respectively. In this way, we can calculate w_2 = 1.5 mm and w_3 = 0.8 mm.

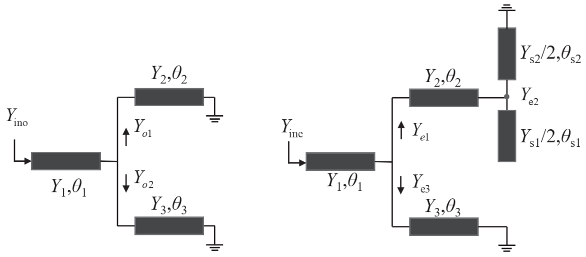

Fig. 3. Equivalent circuits of the proposed resonator: (a) odd-mode equivalent circuit, (b) even-mode equivalent circuit.

When θ_{s1} and θ_{s2} are equal to 0° (there are no open-circuit and short-circuit stubs), we determine the odd-mode and even-mode frequencies under weak coupling, as shown in Fig. 4. At this time, we set $\theta_{\text{s1}}/\theta_1$ = 0/7.4 (1.1/7.4, 2.2/7.4, 3.3/7.4). In Fig. 4 (a), the even-mode frequencies ($f_{\text{e1}}, f_{\text{e2}}, f_{\text{e3}}$) decrease from high to low frequencies as the electrical length ratio $\theta_{\text{s1}}/\theta_1$ shifts from 0 to 0.86. f_{e2} and f_{e3} experience the sharpest drop.

When $\theta_{\text{s2}}/\theta_1$ changes from 0/7.4 to 0.9, and it is observed that the even-mode frequencies (f_{e1}, f_{e2}, f_{e3}) are significantly lower at an electrical length ratio $\theta_{\text{s2}}/\theta_1$ of 0 than at 0.1. Between electrical length ratio $\theta_{\text{s2}}/\theta_1$ of 0.1 to 0.9, the three even-mode frequencies transition gradually to lower frequencies. According to Fig. 4, we choose $\theta_{\text{s1}}/\theta_1$ equal to 0.44 and $\theta_{\text{s2}}/\theta_1$ equal to 0.47. So

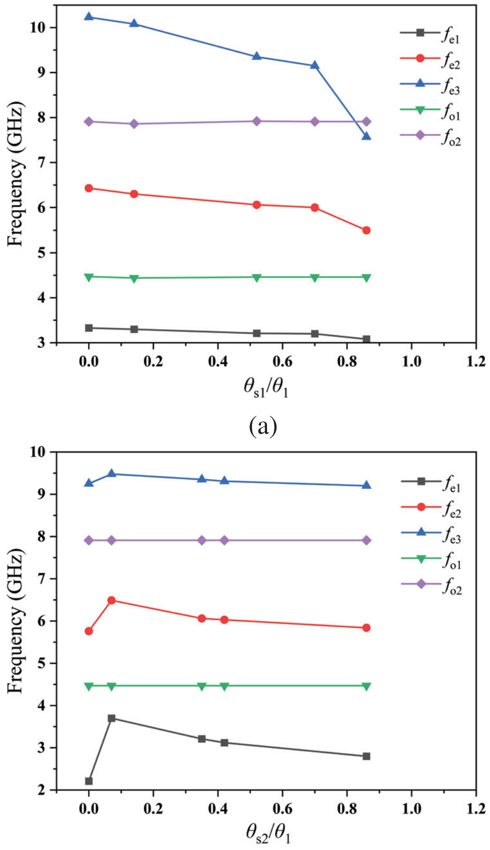

(a)

(b)

Fig. 4. (a) Even- and odd-mode frequencies ($f_{\text{e1}}, f_{\text{e2}}, f_{\text{e3}}, f_{\text{o1}}, f_{\text{o2}}$) under variation of θ_{s1}; (b) even- and odd-mode frequencies ($f_{\text{e1}}, f_{\text{e2}}, f_{\text{e3}}, f_{\text{o1}}, f_{\text{o2}}$) under variation of θ_{s2}.

we can get $l_{s1} = 3.3$ mm and $l_{s2} = 3.5$ mm. While keeping l_{s1} and l_{s2} unchanged, by increasing the stub width, it is found that when $Z_{s1} = 56\ \Omega$ and $Z_{s2} = 69.8\ \Omega$, the five resonant frequencies have a good frequency distribution.

After analyzing the five resonant frequencies, we can further achieve the required passband by varying the length of each stub of the proposed resonator. Figure 5 (a) depicts the variation of the five odd-even mode frequencies with the length l_1, indicating that l_1 has an effect on both odd- and even-mode frequencies. Furthermore, we studied the impact of l_{s1} and l_{s2} on the even-mode frequencies in the passband, as shown in Figs. 5 (b) and (c). We found that l_{s1} has a greater effect on the even-mode frequency f_{e3}, whereas l_{s2} has a greater effect on the even-mode frequency f_{e1}. By tuning these two parameters, we can expand the frequency range to meet the UWB passband requirements. The five frequencies of the resonator are 3.24 GHz, 4.42 GHz, 6 GHz, 7.86 GHz, and 9.45 GHz. Hence, the first five resonant frequencies can be assigned over a broad range, making it advantageous for UWB filter design. According to the above analysis, the optimal value of the short-circuit SIRR here is as follows: $l_2 = 8.5$, $Z_2 = 51\ \Omega$, $l_3 = 6.78$, $Z_3 = 78.2\ \Omega$, $l_{s1} = 3.3$, $Z_{s1} = 56.5\ \Omega$, $l_{s2} = 3.5$, $Z_{s2} = 70.2\ \Omega$. To achieve the necessary frequency range for UWB, the interdigital-coupled lines structure has been utilized. This structure effectively shifts the attenuation zero of the lower stopband, resulting in a tighter coupling. However, the current manufacturing methods present a limitation on the coupling strength. The minimum coupling gap that can be achieved is only 0.1 mm.

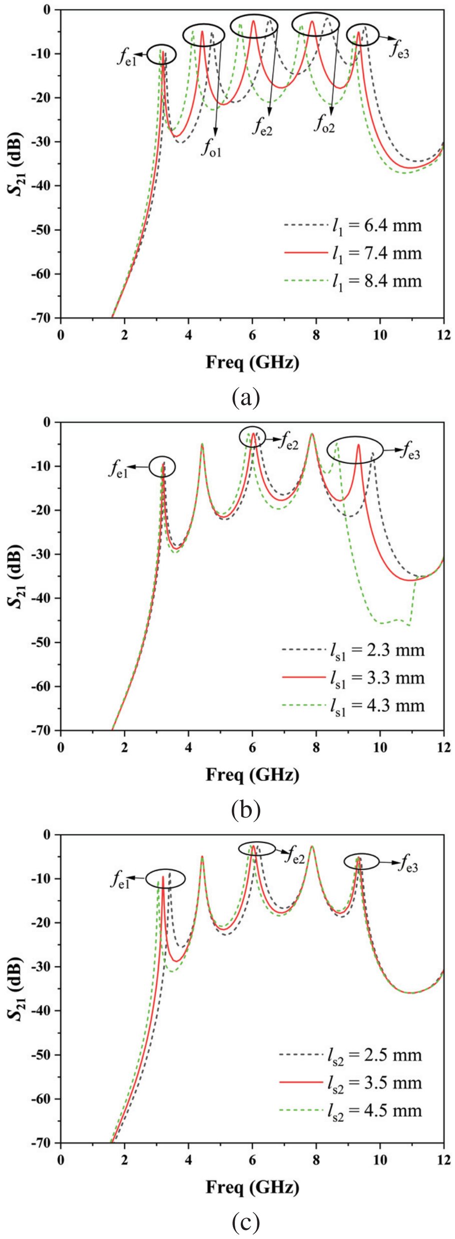

Fig. 5. Simulated response of the proposed resonator under weak coupling: (a) l_1 length variation, (b) l_{s1} length variation, (c) l_{s2} length variation.

After conducting the aforementioned analysis, we have successfully optimized the fundamental structure of the filter. The simulation S-parameters of the UWB bandpass filter are illustrated in Fig. 6. Considering factors such as impedance matching and reflection effects, the passband of 2.8-9.5 GHz is finally selected. An additional pole in the passband may be due to the strong coupling of the interdigital-coupled lines. It is worth noting that there exists a transmission zero at both the lower and upper passband edges, specifically located at 0.2 GHz and 11.74 GHz, respectively. Moreover, the insertion loss and return loss are both better than 0.5 and 14.3 dB, respectively, in the passband. Furthermore, additional transmission zeros present in the upper stopband contribute to extending the stopband to 16 GHz.

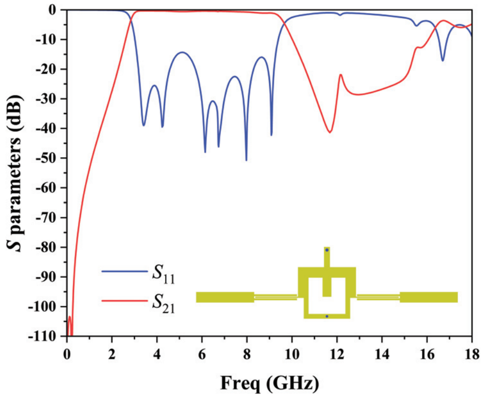

Fig. 6. Simulated response of the basic UWB filter for the range 0-17 GHz.

As demonstrated in Figs. 7 (a-d), we may also modify additional parameters (l_2 and l_3) to improve the frequency characteristics of the filter. The location of the

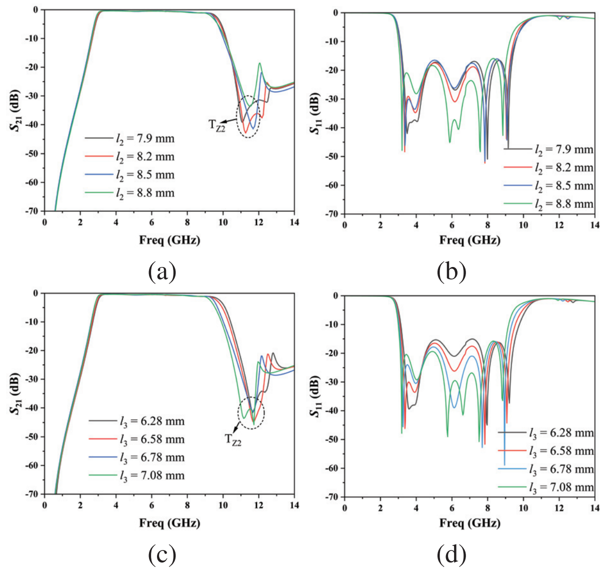

(a) (b)

(c) (d)

Fig. 7. Filter frequency response S-parameters: (a) and (b) variation of l_2, (c) and (d) variation of l_3.

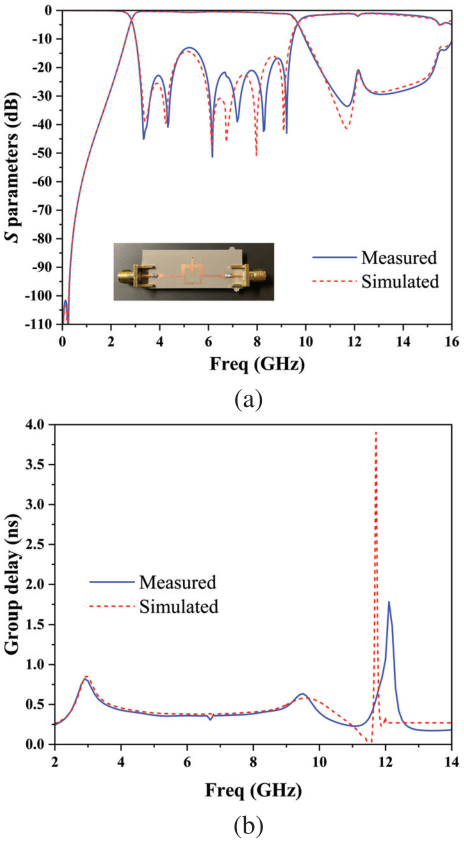

(a)

(b)

Fig. 8. The measured and simulated (a) S-parameters and (b) group delays.

transmission zero on the passband's edge and the passband return loss are both impacted by the length of the stepped impedance ring short-circuit resonator. Changing the lengths of l_2 and l_3 will move the transmission zeros, as seen in Figs. 7 (a) and (c), which will affect the passband bandwidth. The filter may adhere to the UWB spectrum restriction and provide outstanding roll-off characteristics by optimizing the lengths of both. As illustrated in Figs. 7 (b) and (d), changing the resonator length further reduces the passband insertion loss, and fine-tuning the corresponding length may further enhance in-band performance. As the passband in this instance exhibits a reflection characteristic larger than -13 dB and the passband edge transmission zero is better than the suppression of 30 dB, the ideal values utilized here are $l_2 = 8.5$ mm and $l_3 = 6.78$ mm. The suggested structure's final optimal dimension values are (in millimeters): $l_1 = 7.4$, $w_1 = 0.2$, $l_2 = 8.5$, $w_2 = 1.8$, $l_3 = 6.78$, $w_3 = 0.8$, $l_4 = 7.4$, $w_4 = 0.3$, $l_{s1} = 3.3$, $w_{s1} = 1.5$, $l_{s2} = 3.5$, $w_{s2} = 1$, $\Phi_1 = 0.5$, $\Phi_2 = 0.4$, $a = 6.3$, $g = 0.1$.

IV. EXPERIMENTAL VERIFICATION

The results of testing the manufactured filter on a Vector Network Analyzer ZNB40 are shown in Fig. 8. The experimental findings are fundamentally consistent with the simulation outcomes. The passband, with a 3 dB threshold, spans from 2.8 GHz to 9.5 GHz, denoting a relative bandwidth of 108.9%. The highest level of insertion loss within the band is measured at 0.36 dB. The proposed filter exhibits an in-band return loss that exceeds 13 dB. Moreover, it demonstrates out-of-band suppression of over 110 dB at the lower stopband and attenuation greater than 20 dB at the upper stopband, which extends to approximately 15 GHz. The measured group delay, which exhibits excellent linearity, remains flat and varies from 0.38 to 0.85 ns within the passband. Discrepancies between the measured data and the simulation outcomes can be attributed to human error in fabrication and measurement, restricted substrate area, and possible connector reflections. Our ultra-wideband (UWB) bandpass filter is compared with existing examples found in the current literature, as presented in Table 1. The major benefit compared to materials of the same level is its

Table 1: Comparison of the proposed filter with other reported UWB bandpass filters

Ref.	**3 dB FBW (%)**	**Stopband (GHz)/Attenuation (dB)**	**Size ($\lambda_g \times \lambda_g$)**	**Material**
[4]	95	14/>20	1.24×0.67	Copper
[9]	110	18/>12	0.8×0.3	Copper
[10]	110	20/>10	0.74×0.67	Copper
[16]	109.6	17/>17	0.95×0.78	Copper
[20]	109.4	27.6/>20	0.514×0.312	Copper
[21]	125.3	16/>20	1.57×1.18	HTS
This work	108.9	15/>20	0.84×0.41	Copper

lower insertion loss. The size has a minor benefit over different material levels.

V. CONCLUSION

A compact UWB bypass filter employing interdigital-coupled lines and a multi-stub-loaded stepped-impedance ring resonator is presented and implemented. By adjusting the corresponding stub electrical length and impedance ratio, the distribution of two odd mode frequencies and three even mode frequencies within the passband can be readily achieved. The implementation of a interdigital-coupled line as the feed for the filter is preferred due to its ability to offer optimal reflection and bandwidth. The proposed resonator possesses inherent characteristics that result in the generation of multiple transmission zeros at the upper and lower edge of the passband. This feature enhances the filter selectivity, rendering the proposed filter an attractive choice for ultra-wideband wireless communication systems.

ACKNOWLEDGMENT

This work was supported by the Research on Ultra Wideband Filters Based on Multimode Resonators under Grant China West Normal University Talent Research Fund Project 17YC054.

REFERENCES

[1] Federal Communications Commission. Revision of part 15 of the commission's rules regarding ultra-wideband transmission systems. Tech. Rep., ET-Docket 98-153, FCC02-48, April 2002.

[2] L. Zhu, S. Sun, and R. Li, *Microwave Bandpass Filters for Wideband Communications*, John Wiley & Sons, pp. 116-148, Jan. 2011.

[3] J.-S. Hong and M. J. Lancaster, *Microstrip Filters for RF/microwave Applications*, second edition, John Wiley & Sons, pp. 123-153, 2011.

[4] C.-W. Tang and M.-G. Chen, "A microstrip ultra-wideband bandpass filter with cascaded broadband bandpass and bandstop filters," *IEEE Transactions on Microwave Theory and Techniques*, vol. 55, no. 11, pp. 2412-2418, Nov. 2007.

[5] C.-L. Hsu, F.-C. Hsu, and J.-K. Kuo, "Microstrip bandpass filters for ultra-wideband (UWB) wireless communications," *IEEE MTT-S International Microwave Symposium Digest*, Long Beach, CA, USA, pp. 679-682, 2005.

[6] P. P. Shome, T. Khan, S. K. Koul, and Y. M. M. Antar, "Compact UWB-to-C band reconfigurable filtenna based on elliptical monopole antenna integrated with bandpass filter for cognitive radio systems," *IET Microw. Antennas Propag.*, vol. 14, no. 10, pp.1079-1088, Aug. 2020.

[7] Z. Zhang and F. Xiao, "An UWB bandpass filter based on a novel type of multi-mode resonator," *IEEE Microwave and Wireless Components Letters*, vol. 22, no. 10, pp. 506-508, Oct. 2012.

[8] Q.-X. Chu, X.-H. Wu and X.-K. Tian, "Novel UWB bandpass filter using stub-loaded multiple-mode resonator," *IEEE Microwave and Wireless Components Letters*, vol. 21, no. 8, pp. 403-405, Aug. 2011.

[9] P. P. Shome and T. Khan, "A compact design of circular ring-shaped MMR based bandpass filter for UWB applications," *IEEE Asia-Pacific Microwave Conference (APMC)*, Singapore, pp. 962-964, Dec. 2019.

[10] G. Saxena, P. Jain, and Y. K. Awasthi, "Design and analysis of a planar UWB bandpass filter with stop-band characteristics using MMR technique," *Int. J. Micro. and Wireless Tech.*, vol. 13, no. 10, pp. 999-1006, 2021.

[11] G. Y. Wei, Y. X. Wang, J. Liu, Y. Gao, and X. T. Yao, "A novel highly selective UWB bandpass filter using quad-mode stub-loaded resonator," *Pro. Electromagnet. Research Lett.*, vol. 109, pp. 57-63, 2023.

[12] J. Liu, W. Ding, J. Chen, and A. Zhang, "New ultra-wideband filter with sharp notched band using defected ground structure," *Pro. Electromagnet. Research Lett.*, vol. 83, pp. 99-105, 2019.

[13] Q.-X. Chu and X.-K. Tian, "Design of UWB bandpass filter using stepped-impedance stub-loaded resonator," *IEEE Microw. and Wireless Compon.Lett.*, vol. 20, pp. 501-503, 2010.

[14] C. Y. Hung, M. H. Weng, and Y. K. Su., "Design of compact and sharp rejection UWB BPFs using interdigital stepped-impedance resonators," *IEICE Transactions on Electronics*, vol. 90, pp. 1652-1654, 2017.

[15] X. H. Luo, X. Cheng, J. A. Han, L. Zhang, F. J. Chen, Y. J. Guo, and X. J Deng, "Compact dual-band bandpass filter using defected SRR and irregular SIR," *Electronics Letters*, vol. 55, pp. 463-465, 2019.

[16] Y.-C. Chang, C.-H. Kao, M.-H. Weng, and R.-Y. Yang, "Design of the compact wideband bandpass filter with low loss, high selectivity and wide stop-band," *IEEE Microw. and Wireless Compon. Lett.*, vol. 18, pp. 770-772, 2008.

[17] M. Sazid, N. S. Raghava, and A. N. Ghazali, "UWB-BPF based on broadside coupled technology with triple-notched passband," *Microw. Opt. Technol. Lett.*, vol. 65, no. 7, pp. 1910-1916, July 2023.

[18] A. N. Ghazali, M. Sazid, and B. Virdee, “A compact UWB-BPF based on microstrip-to-CPW transition with multiple transmission zeros,” *Microw Opt. Technol. Lett.*, vol. 60, no. 8, pp. 1925-1928, Aug. 2018.

[19] C. H. Kim and K. Chang, “Ultra-wideband (UWB) ring resonator bandpass filter with a notched band,” *IEEE Micro. and Wire. Compon. Lett.*, vol. 21, no. 4, pp. 206-208, April 2011.

[20] H. Zhu and Q.-X. Chu, “Ultra-wideband bandpass filter with a notch-band using stub-loaded ring resonator,” *IEEE Micro. and Wire. Compon. Lett.*, vol. 23, no. 7, pp. 341-343, July 2013.

[21] Z. Long, M. Tian, T. Zhang, M. Qiao, T. Wu, and Y. Lan, “High-temperature superconducting multimode dual-ring UWB bandpass filter,” *IEEE Transactions on Applied Superconductivity*, vol. 30, no. 2, pp. 1-4, March 2020.

[22] C. H. Kim and K. Chang, “Ring resonator bandpass filter with switchable bandwidth using stepped-impedance stubs,” *IEEE Transactions on Microwave Theory and Techniques*, vol. 58, no. 12, pp. 3936-3944, Dec. 2010.

Guangyong Wei was born in Chongqing. He received a bachelor’s degree in engineering. He received a bachelor’s degree in electronic information from Panzhihua University in 2021. He is currently studying for a master’s degree.

His research interests are RF microwave devices, UWB antennas.

Yunxiu Wang was born in Kaizhou, Chongqing, in 1967. In December 2008, she graduated from the School of Physics and Electronics, University of Electronic Science and Technology of China with a doctorate in science. From August 2012 to August 2013, she was a visiting scholar at Nanyang Technological University, Singapore. Current research fields mainly include electromagnetic field and microwave technology, scientific research, and teaching of microwave passive devices. She participated in 4 National Natural Science Foundation projects and 1 University Doctoral Fund project. She presided over 1 Sichuan Provincial Key Project, 1 Sichuan Provincial Scientific Research Fund Project, 1 Sichuan Provincial Department of Education Teaching Reform Project, 1 school project Doctoral start-up project, 1 school-level overseas returnee project, and 2 school-level excellent courses.

Jie Liu was born in Sichuan, China, in 1999. In 2021, he will receive a bachelor’s degree from China West Normal University. He has won several Blue Bridge Electronic Design Awards at the school. In September 2021, he will continue to study for a master’s degree at China West Normal University. He graduated from the School of Electronic Information Engineering, China West Normal University, Nanchong, China.

His main research directions include computational electromagnetics, bandpass filters, and numerical calculations.

Haiping Li was born in 1998 in Bazhong City, Sichuan Province, China. In 2021, he graduated from Panzhihua University, majoring in electronic information engineering, with a bachelor’s degree. He is currently studying for a master’s degree in optical fiber sensing at the School of Electronic Information Engineering, China West Normal University, and his current research interest is optical fiber technology.

Edge Hole Effect on Isolation of UWB MIMO RDRA for 5G Outdoor Applications

Tamer G. Abouelnaga and Esmat A. Abdallah

Microstrip Circuits Department, Electronics Research Institute ERI, Cairo, Egypt
Tamer@eri.sci.eg

***Abstract* –** For 5G sub-6 GHz outdoor applications, a highly isolated two-port rectangular dielectric resonator antenna (RDRA) with UWB MIMO is presented in this research. For isolation enhancement purposes at the lower frequency band (2.27 GHz-2.62 GHz), a longitudinal slot is inserted at the ground plane. For isolation enhancement at the higher frequency band (3.9 GHz-5.73 GHz), an edged hole is inserted in the RDRA. Investigations are conducted on the impacts of slotted ground as well as edged hole radius on isolation. The orthogonal feeding scheme of UWB MIMO RDRA considering both edged hole and slotted ground plane effects are investigated. For the edged hole MIMO RDRA with a slotted ground plane, isolation is better than -24.7 dB at a higher frequency band and is better than -15.5 dB at a lower frequency band. This isolation improvement is explained by the surface current density distribution. The use of an edged hole RDRA and an aperture-coupled orthogonal feeding allows UWB bandwidth and good efficiency performances on the 5G operating bands. To justify the MIMO performance, the envelope correlation coefficient (ECC) and diversity gain (DG) are applied.

***Index Terms* –** 5G, co-polarization, cross-polarization, DG, DRA, ECC, MIMO antenna, UWB.

I. INTRODUCTION

The primary requirements of wireless 5G communication networks are extremely high data rates, improved spectral efficiency, lower latency, and high quality of service (QoS) [1–3]. The millimeter wave frequencies (more than 24 GHz) are used for interior coverage, whereas the 5G sub-6 GHz channels are used for outdoor applications [4]. According to the most recent edition of the 3GPP technical standard (TS 38.101), the sub-6 GHz bands for 5G communications are divided into new radio bands such as n46 (5.150- 5.925), n47 (5.855-5.925), n53 (2.483.5-2.495), n77 (3.3 GHz-4.2 GHz), and n79 (4.4 GHz-5 GHz) [5]. The multiple input, multiple output (MIMO) antenna system takes into account many antenna elements on a single substrate, which worsens the isolation properties. Low isolation (below 10 dB) between antenna components with constrained spacing is therefore extremely difficult [6]. There have been many different isolation techniques used, but it has been found that decoupling networks [7–9], parasitic methods [10–12], flawed ground structures [13–15], neutralization lines [16–18], metamaterials [19–20], the self-isolated antenna [21], and orthogonal polarization [22] all resulted in better isolation. Although some of the previously suggested antennas had certain shortcomings, overall, they had a positive influence on MIMO antenna isolation. For instance, a decoupling network-used antenna [7] suffered from an increase in envelope correlation coefficient (ECC) from 0.01 and 0.19 to 0.12 and 0.29, respectively, with and without the use of a dual-band decoupling network. Frequency shifting from 5.8 GHz to 5.5 GHz was a problem for parasitic approaches [11] when electromagnetic band gap (EBG) structures were present. Due to H-shaped defected ground structures (DGS), DGS [14] only experienced little radiation profile distortion. Wider lower-frequency bandwidth as opposed to upper-frequency bandwidth was a problem for neutralization lines [18]. The susceptibility of resonators to the horizontal movement was a problem for metamaterials [19]. Hence, a mutual coupling decrease was not seen. Narrow bandwidth was a problem for orthogonal polarization and self-isolated antenna techniques [21, 22].

With isolation greater than -24.7 dB at higher frequency bandwidth (3.9 GHz to 5.73 GHz) and isolation better than -15.5 dB at lower frequency bandwidth (2.27 GHz to 2.62 GHz), a high isolated dual-port ultra-wideband (UWB) MIMO rectangular dielectric resonator antenna (RDRA) is suggested in this research. This is accomplished by using an orthogonal feeding system, an edged hole at the RDRA, and a longitudinal slot at the ground. An investigation is done into how orthogonal feeding and the effects of edged hole radius and slotted ground affect isolation. A microstrip-matched stub feed is utilized for impedance matching. An etched Z-shape aperture at the ground plane connects a dielectric resonator to a feed stub. Calculated ECC and DG both fall within the permitted range. The suggested

Submitted On: October 22, 2022
Accepted On: June 16, 2023

https://doi.org/10.13052/2023.ACES.J.380706

1054-4887 © ACES

MIMO antenna is a candidate for sub-6 GHz outdoor 5G applications since the measured -6 dB operating frequency bandwidth is adequate for the n46, n47, n53, n77, n78, and n79 5G frequency bands.

The proposed edged hole MIMO RDRA with a slotted ground plane achieves -15.53 dB and -24.7 dB at lower and higher frequency bands, respectively. That is achieved without using DGS or EBG structures, or parasitic methods that may cause radiation distortion or frequency shift. Also, ECC is kept lower than 0.01 all over the operating lower and higher bandwidths. The proposed edged hole MIMO RDRA with a slotted ground plane has wider upper-frequency bandwidth as compared to lower-frequency bandwidth.

II. RDRA's ORTHOGONAL FEEDING METHOD

This section introduces the RDRA both without and with the slotted ground plane. The perspective view, top view, and bottom view of the MIMO RDRA are displayed in Fig. 1. It uses a low-cost FR4 substrate with a 1.6 mm thickness, a dielectric constant ε_r of 4.65, and a loss tangent $tan(\delta)$ of 0.02. On the substrate's top surface, two Z-slots and two 50 Ω matching stubs are etched into the ground plane. On the top surface of the substrate, two rectangular-shaped dielectric resonators made of alumina are positioned. The RDRA's TE_{111} mode presence is based on [23–25]. The DRA with the dimension's width w, length l, and height h emits magnetic dipole radiation. The following formulas can be used to calculate the resonant frequency:

$$f_o = \frac{c}{2\pi\sqrt{\varepsilon_r}}\sqrt{k_x^2+k_y^2+k_z^2} \tag{1}$$

$$k_x = \pi/l, k_z = \pi/2h \tag{2}$$

$$w = \frac{2}{k_y} tanh\left(\frac{k_{yo}}{k_y}\right), k_{yo} = \sqrt{k_x^2+k_z^2}, \tag{3}$$

where c represents the vacuum-bound speed of light. You may get the resonance frequency f_o by knowing the length l and height h and solving for k_y and w. The computed resonance frequency of a DRA with identical dimensions of length and breadth of 25 mm and various heights h values is shown in Table 1.

Table 1: The resonant frequency of various height levels of RDRA

h (mm)	10	15	20	25
f_o(GHz)	3.23	2.71	2.22	2.39

A dielectric cube with a 25 mm edge length is employed as a starting point. The suggested MIMO RDRA is modeled, simulated, and optimized using the CST electromagnetic solver taking into account the feeding scheme impact; the MIMO RDRA optimized dimensions are shown in Table 2. The resonance frequency for an RDRA with equal dimensions of 21.5 mm in width, length, and height is discovered to be 2.39 GHz. Without taking into account the impact of the feeding mechanism, the predicted resonant frequency is discovered to be 2.99 GHz. Figure 1 depicts the isolation between the two ports of the MIMO RDRA aerial. It is noted that at the lower operating bandwidth (2.25 GHz to 2.52 GHz), the isolation between the two ports is maintained below -9.5 dB, while at the higher operating frequency bandwidth, it is maintained below -16 dB. (3.6 GHz to 5.7 GHz).

Table 2: MIMO RDRA dimensions (mm)

L_{DRA}	S_{1H}	S_{2H}	S_{3H}	S_{1V}
21.5	18.9	17.9	7.9	9.25
S_{2V}	L_S	w_S	H_{DRA}	$L_{1\ Slot}$
11.25	80	40	15.24	11
$L_{2\ Slot}$	$L_{3\ Slot}$	$w_{1\ Slot}$	$w_{2\ Slot}$	$L_{3\ Feed}$
5	11	6	6.3	13
$L_{2\ Feed}$	$L_{1\ Feed}$	$w_{1\ Feed}$	$w_{2\ Feed}$	S_{4H}
6	7	2.7	2.7	17.3
L_{s1}	L_{s2}			
38	38			

For the lower frequency band isolation enhancement, a longitudinal slot at the ground is inserted. The obtained isolation is better than -13.2 dB, while the higher frequency band is better than -17 dB, as shown in Fig. 1 (g). The rectangular slot is etched and centered at the ground plane with dimensions of 40 mm width and

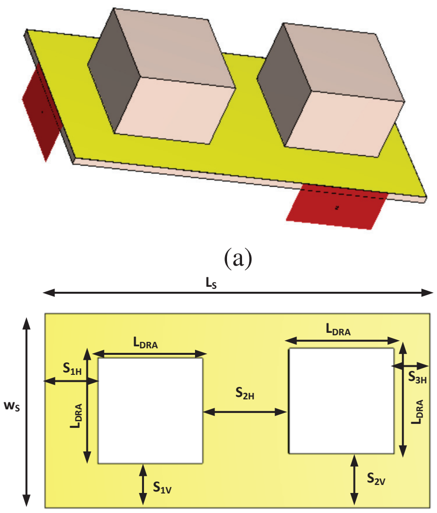

Fig. 1. *Continued*

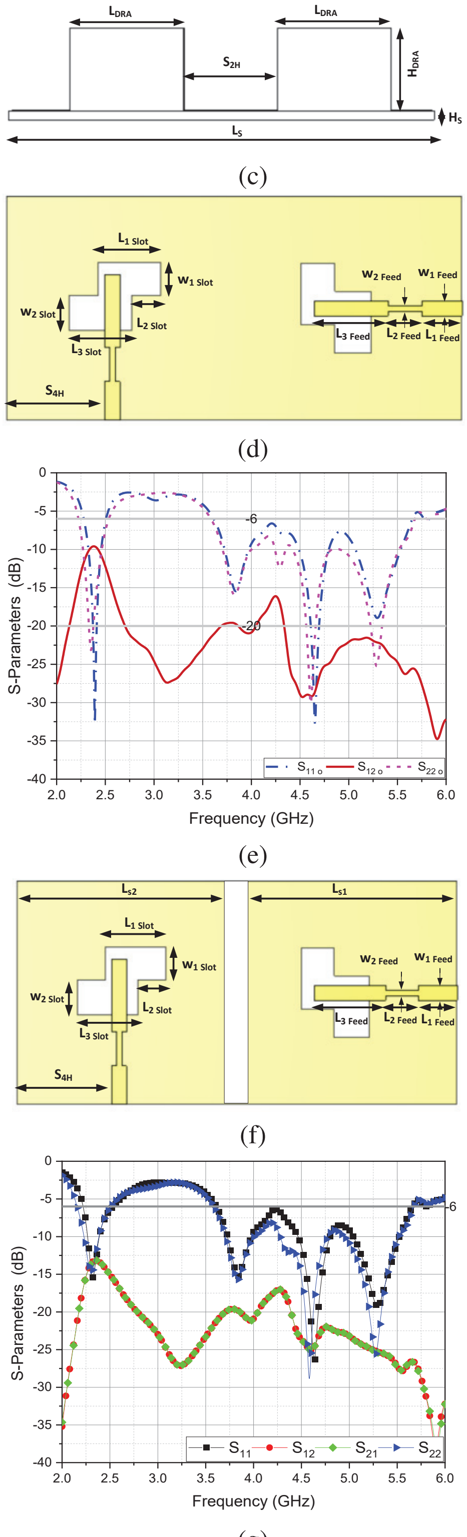

(c)

(d)

(e)

(f)

(g)

Fig. 1. The suggested MIMO RDRA: (a) perspective view, (b) top view, (c) side view, (d) bottom view, (e) S-parameters, (f) bottom view of the MIMO RDRA with the slotted ground plane, and (g) S-parameters of the MIMO RDRA with the slotted ground plane.

8.1 mm length. Its position is tuned using the CST simulator and is shown in Fig. 1 (f). Table 2 shows the dimensions of the bottom view of the slotted ground plane.

III. AN EDGED HOLE RDRA ORTHOGONAL FEEDING TECHNIQUE

This section introduces the edged hole RDRA both without and with the slotted ground plane. An edged hole of 4 mm radius is created at the RDRA edge, as illustrated in Figs. 2 (a) and (b) to improve isolation at the higher frequency band. At a higher frequency range, in Fig. 2 (c), more isolation is achieved. In comparison to -9.5 and -19.6 dB, with the same orthogonal feeding but without an edged hole and slotted ground plane, the isolation is retained below -10.5 dB and -22.3 dB at the lower and higher working bands, respectively.

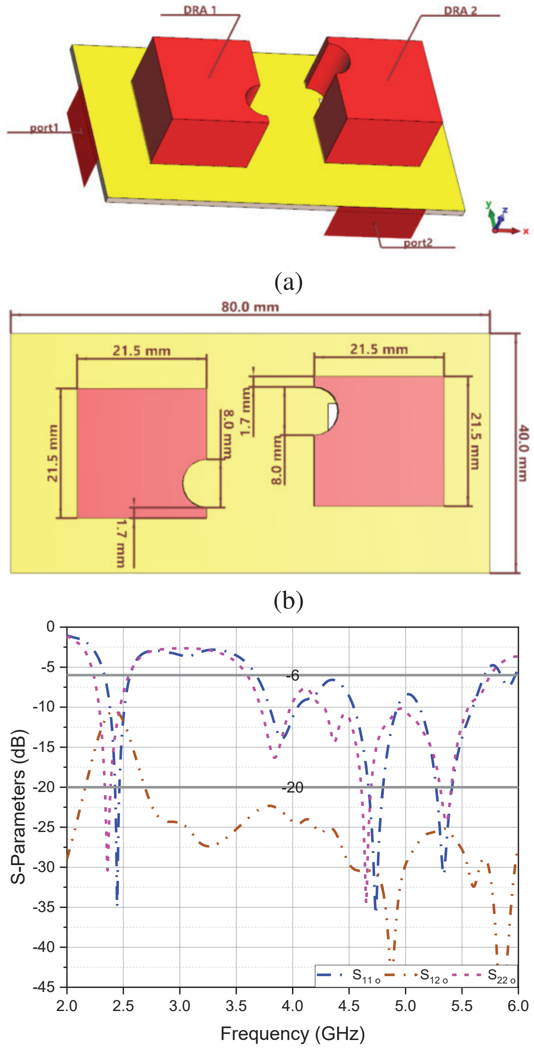

(a)

(b)

(c)

Fig. 2. The edged hole MIMO RDRA: (a) perspective view, (b) top view, and (c) S-parameters.

The impact of hole radius on isolation is seen in Fig. 3 (a). For the lower frequency range, the isolation is maintained below -9.6 dB at a hole radius of 1 mm and below -10.96 dB at a hole radius of 5 mm. Moreover, the isolation is maintained below -16.5 dB at a 1 mm hole radius and below -23.5 dB at a 5 mm hole radius at the higher frequency spectrum. At a hole radius of 1 mm, the lower bandwidth changes from 2.29 GHz-2.51 GHz to 2.36 GHz-59 GHz. According to Fig. 3 (b), the higher bandwidth changes from 3.62 GHz to 5.66 GHz at a 1 mm hole radius to 3.69 GHz to 5.74 GHz at a 5 mm hole radius.

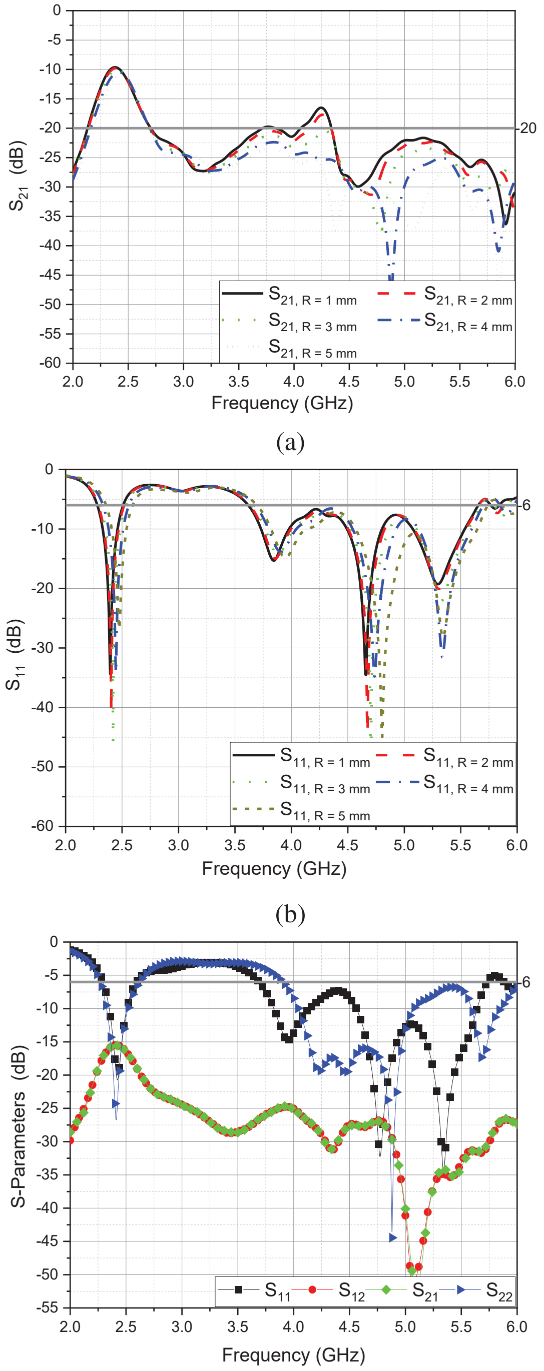

(a)

(b)

(c)

Fig. 3. MIMO edged hole RDRA: (a) S_{21}, (b) S_{11} as the hole radius varies, and (c) S-parameters with the slotted ground plane.

To achieve better isolation at the lower frequency band, the slotted ground plane is used. The same dimensions and position as Fig. 2 (f) are considered. The isolation of the higher bandwidth is kept below -24.7 dB and the lower bandwidth is kept below -15.53 dB, Fig. 3 (d). Table 3 shows the lower and the higher bandwidths along with the obtained isolation for the four previous MIMO RDRA configurations. The lower frequency band shifts from 2.25 GHz-2.52 GHz to 2.27 GHz-2.62 GHz and isolation shifts from -9.5 dB to -15.53 dB for the RDRA without the slotted ground plane and the edged hole RDRA with the slotted ground plane, respectively. Also, the higher frequency band shifts from 3.6 GHz-5.7 GHz to 3.9 GHz-5.73 GHz, and isolation shifts from -16 dB to -24.7 dB for the RDRA without the slotted ground plane and the edged hole RDRA with the slotted ground plane, respectively.

Table 3: The bandwidths and the isolations of the four MIMO RDRA configurations

Antenna	BW (GHz)	Min Isolation (dB)
RDRA without slotted ground	2.25-2.52	-9.5
	3.6-5.7	-16
RDRA with slotted ground	2.22-2.5	-13.2
	3.58-5.67	-17
Edged RDRA without slotted ground	2.33-2.56	-10.5
	3.68-5.7	-22.3
Edged RDRA with slotted ground	2.27-2.62	-15.53
	3.9-5.73	-24.7

A. Distribution of surface current

The surface current density distribution at 2.48 GHz (lower frequency band) and 4.2 GHz (higher frequency band) for both MIMO RDRA without slotted ground and MIMO edged hole RDRA with the slotted ground plane, where port 1 is excited, is shown in Fig. 4 to examine the isolation properties of the MIMO RDRA antennas. It has been noted from Fig. 4 (a) that the coupling current among MIMO components is quite weak in the case of only left MIMO RDRA excitation. The difference between the surface current density near the left RDRA and near the right RDRA, seen in Fig. 4 (a), is also higher than the difference between the surface current density near the left RDRA and near the right RDRA, shown in Fig. 4 (b). So, both surface current distribution characteristics back up the conclusion that the suggested orthogonal MIMO RDRA's self-isolation with an edged hole structure is superior to that of the proposed orthogonal MIMO RDRA without an edged hole structure. That explains the isolation improvement that is gained when orthogonal MIMO RDRA with an edged hole structure is applied. The same outcomes have been seen when just right MIMO RDRA excitation is used, as illustrated in Fig. 4 (c) and (d).

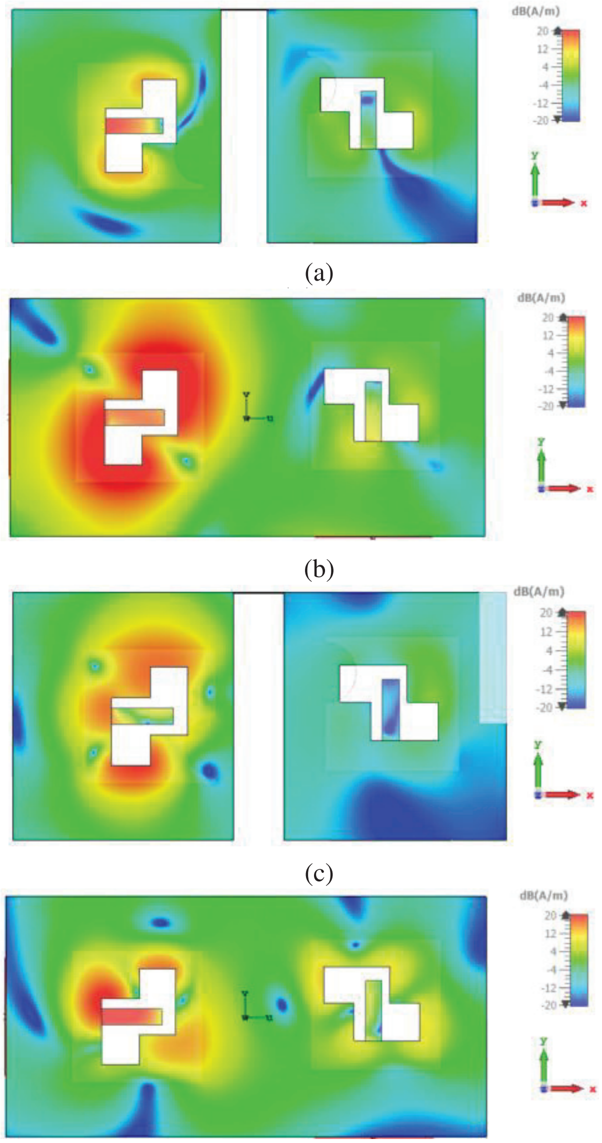

(a)

(b)

(c)

(d)

Fig. 4. Surface current distribution of MIMO RDRA: (a) with edged hole and slotted ground at 2.4 GHz, (b) without the edged hole and slotted ground at 2.4 GHz, (c) with edged hole and slotted ground at 4.2 GHz, and (d) without the edged hole and slotted ground at 4.2 GHz.

B. Co-polarized and cross-polarized radiation pattern

Resonance frequencies at 2.39 GHz, 3.84 GHz, 4.65 GHz, and 5.27 GHz are provided by the MIMO RDRA without an edged hole and slotted ground. Figure 5 shows that the proposed antenna's E-plane and H-plane radiation patterns are directional at a frequency of 2.39 GHz. (the same performance at other resonant frequencies). Moreover, Fig. 6 shows the predicted radiation pattern for the MIMO-edged hole RDRA with the slotted ground. With its slotted ground and MIMO-edged holes, the RDRA offers resonance frequencies of 2.4 GHz,

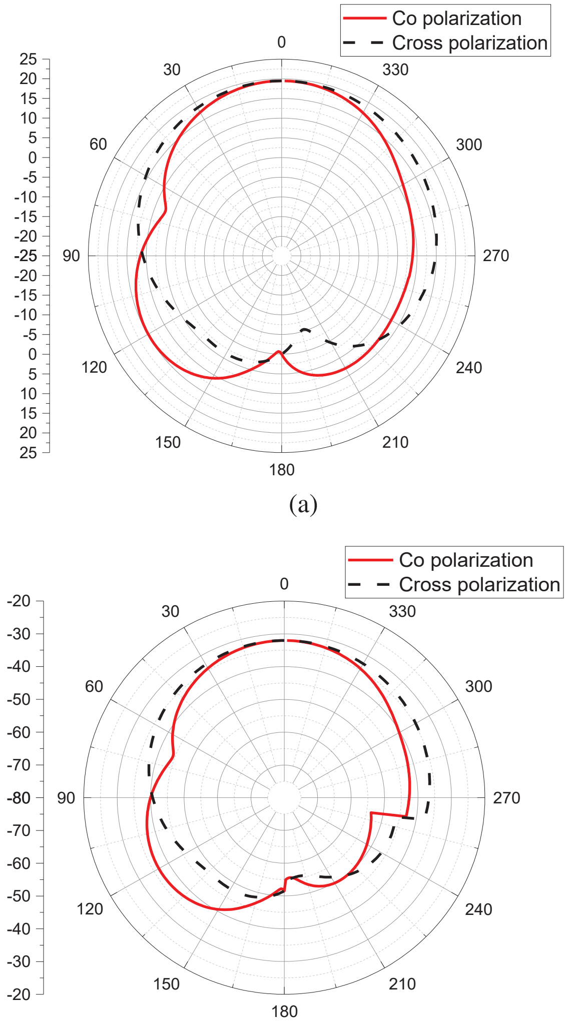

(a)

(b)

Fig. 5. MIMO RDRA antenna's simulated radiation pattern (without the edged hole and slotted ground): (a) E-plane Co and cross-polarization dB (V/m) at 2.39 GHz, and (b) H-plane Co and cross-polarization dB (A/m) at 2.39 GHz.

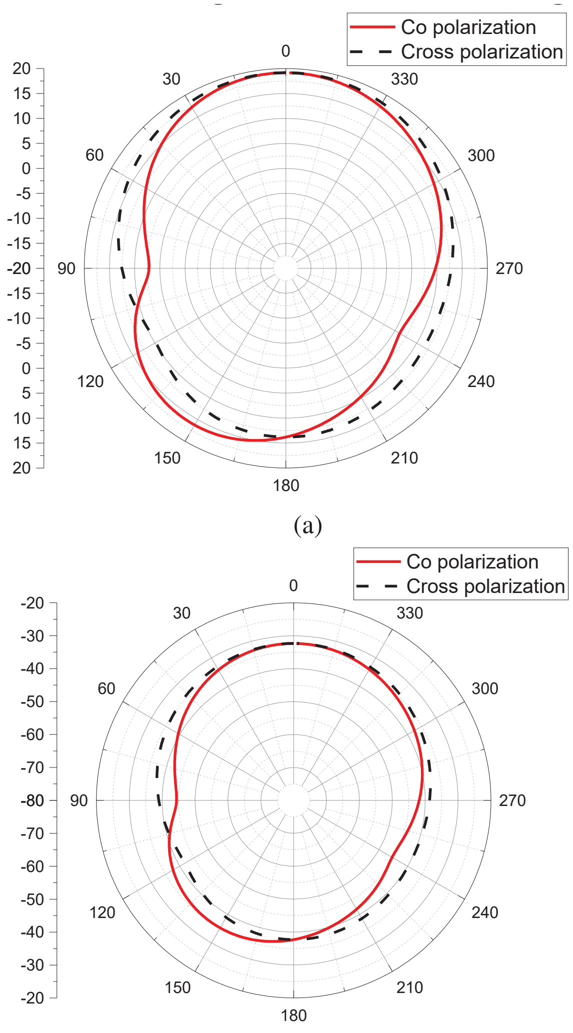

(a)

(b)

Fig. 6. MIMO RDRA antenna's simulated radiation pattern (with edged hole and with slot): (a) E-plane Co and cross-polarization dB (V/m) at 2.4 GHz, and (b) H-plane Co and cross-polarization dB (A/m) at 2.4 GHz.

3.95 GHz, 4.78 GHz, and 5.34 GHz. Co-polarization and cross-polarization are only displayed for the left MIMO-edged hole RDRA at 2.4 GHz. The radiation patterns show that the proposed antenna's E- and H-planes are directional at these resonance frequencies. Both MIMO-edged hole RDRA with and without slotted ground structures can receive signals in both directions.

In Figs. 7 (a) and (b), respectively, the simulated gain and radiation efficiency of MIMO RDRA with slotted ground and MIMO edged hole RDRA without slotted ground are shown. The radiation efficiency for MIMO RDRA without slotted ground is better than 84% for the lower operating frequency bandwidth (2.25 GHz to 2.55 GHz) and higher than 75% for the higher operating frequency bandwidth (3.6 GHz to 5.7 GHz). Radiation efficiency is better than 85% for MIMO-edged hole RDRA with the slotted ground for the lower operating frequency bandwidth (2.27 GHz to 2.62 GHz) and higher than 76% for the higher operating frequency bandwidth (3.9 GHz to 5.73 GHz). The gain for MIMO RDRA without slotted ground is higher than 4.7 dB for the lower operating frequency bandwidth (2.25 GHz to 2.55 GHz) and higher than 3.6 dB for the larger operating frequency bandwidth (3.6 GHz to 5.7 GHz). The gain is larger than 4.5 dB for MIMO-edged hole RDRA with the slotted ground for the lower operating frequency bandwidth (2.27 GHz to 2.62 GHz) and greater than 4 dB for the higher operating frequency bandwidth (3.9 GHz to 5.73 GHz).

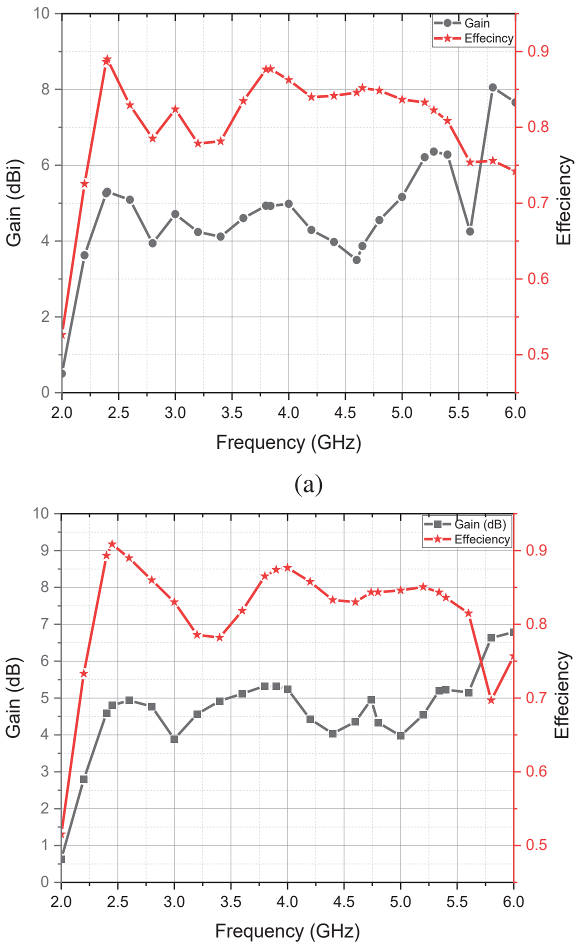

(a)

(b)

Fig. 7. Gain and radiation efficiency of MIMO RDRA: (a) without, and (b) with an edged hole and slotted ground.

C. Performance of diversity

By computing the diversity performance parameters (ECC, DG), the performance of the orthogonal MIMO

RDRA with and without edged holes is presented. Equation (4) is used to calculate the ECC based on the S-parameters calculation [25].

$$ECC = \frac{|S_{nn}^{*}S_{nm} + S_{mn}^{*}S_{mm}|^{2}}{\left(\left(1-(|S_{nn}|^{2}+|S_{mn}|^{2})\right)\left(1-(|S_{mm}|^{2}+|S_{nm}|^{2})\right)\right)}. \quad (4)$$

According to the International Telecommunication Union (ITU) standard, the ECC value should be smaller than 0.5 to provide optimal MIMO aerial performance. Throughout the whole operational lower and higher frequency bands, the correlation values for the MIMO RDRA without slotted ground and the edged hole RDRA with slotted ground are less than 0.04 and 0.02, respectively, making it a viable MIMO antenna for the authorized bands. Equation (5) is used to determine diversity gain [26]. Close to 10 is the acknowledged diversity gain value. Based on Fig. 8, it can be shown that for both the lower and higher operating frequency bands, MIMO RDRA without ground slot and MIMO edged hole RDRA with grounded slot both exhibit a diversity gain of almost 10.

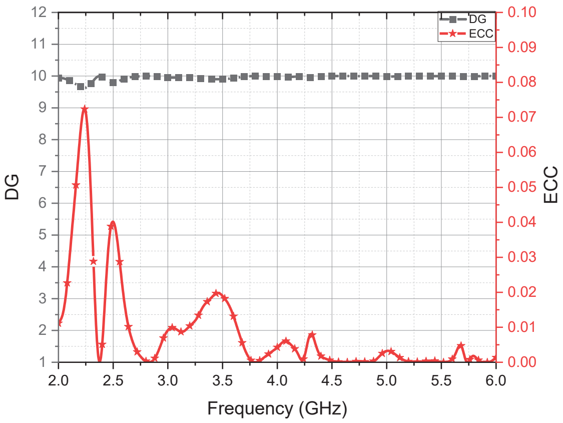

(a)

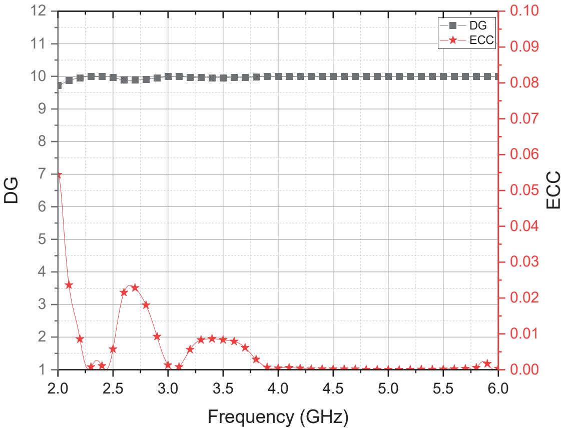

(b)

Fig. 8. ECC and DG versus frequency plot of MIMO RDRA: (a) without the slotted ground, and (b) with the edged hole and slotted ground.

$$DG = 10\sqrt{1-|0.99ECC|^{2}}. \quad (5)$$

Table 4 shows a comparison of the proposed edged hole MIMO RDRA with a slotted ground plane considering bandwidth, isolation, ECC, and diversity gain.

Table 4: Comparison of the proposed edged hole MIMO RDRA with the previous MIMO structure

Antenna	−6 dB BW (GHz)	Min Isolation (dB)	Max ECC	Min DG
Edged RDRA with slotted ground	2.27–2.62	15.53	0.01	10
	3.9 – 5.73	24.7	0.002	10
[1]	3.38–3.78	26	0.04	-
	4.95–	25	0.06	-
[4]	5.58			
[8]	3.3 – 5	19	0.018	-
[15]	2.6 – 3.6	14	0.21	10

IV. PROTOTYPE OF ANTENNA

An orthogonal MIMO RDRA (without an edged hole) antenna is selected to be manufactured and tested for verification, as shown in Fig. 9. Figures 9 (a) and (b) show images of the manufactured rectangular MIMO antenna. Figure 9 (c) also displays a picture of the experimental setup. For experimental validation, a Rohde & Schwarz ZVP 20 Vector Network Analyzer is employed. Figure 10 displays the predicted and observed scattering characteristics for the suggested orthogonal MIMO-RDRA (without edged hole). The findings of the measured and simulated S-parameters coincide rather well. The relevant difference results from manufacturing flaws, soldering effects, glue effects, and an alignment issue with both the feeding system and RDRA. The RDRA block is just an alumina layer that is stacked one to another using glue. Compared to its simulated counterpart's lower frequency -6 dB bandwidth of 2.25 GHz to 2.52 GHz, the measured lower -6 dB frequency bandwidth is enlarged from 2.54 GHz to 2.79 GHz. In contrast to its simulated equivalent, which has a high-frequency -6 dB bandwidth of 3.6 GHz to 5.7 GHz, the measured -6 dB high-frequency bandwidth is expanded to 3.77 GHz to 6 GHz.

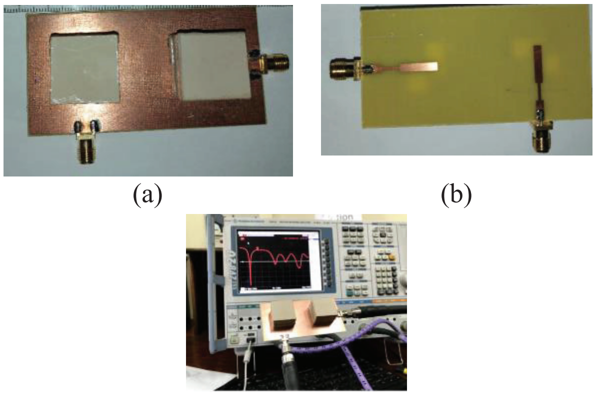

(a) (b)

(c)

Fig. 9. Fabricated rectangular MIMO RDRA prototype (without edged hole): (a) top view, (b) bottom view, and (c) experimental setup.

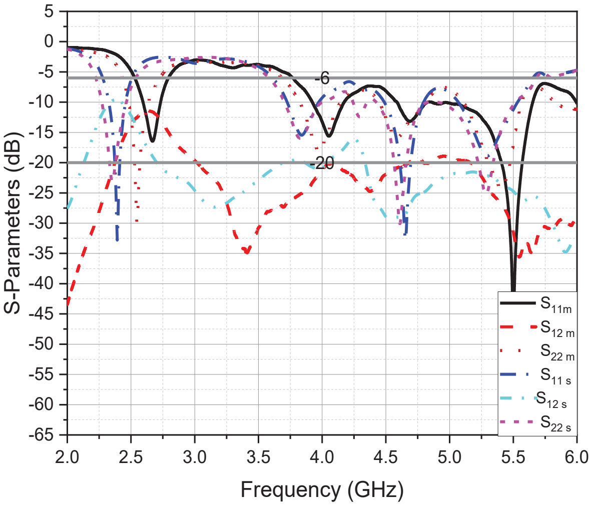

Fig. 10. Simulated and measured S-parameters of MIMO RDRA (without edged hole).

V. CONCLUSION

In this paper, MIMO RDRA with and without a slotted ground plane and MIMO edged hole RDRA with and without a slotted ground plane are investigated for an orthogonal feeding scheme. For isolation enhancement at the lower frequency band, the slotted ground plane was used, while the isolation enhancement at the higher frequency was achieved by using the edged hole RDRA.

Without a slotted ground plane, the MIMO RDRA featured two -6 dB impedance bandwidths, a lower operating frequency band (between 2.25 and 2.52 GHz), and a higher operating frequency band (3.6 GHz to 5.7 GHz). A lower operating frequency bandwidth (2.27 GHz to 2.62 GHz) and a larger operating frequency bandwidth were available for the MIMO edged hole RDRA with the slotted ground plane (3.9 GHz to 5.73 GHz). It was looked into how hole radius affected everything. Structures using MIMO RDRA have a minimum efficiency of 75%. The suggested MIMO RDRA antennas were excellent candidates for outdoor 5G applications due to the diversity of 10 throughout the working frequency bands.

REFERENCES

[1] T. G. Abouelnaga, I. Zewail, and M. Shokair, “Design of 10 × 10 massive MIMO array in a sub-6 GHz smartphone for 5G applications,” *Progress in Electromagnetics Research B*, vol. 91, pp. 97-114, 2021.

[2] I. Al-Mejibli and S. Al-Majeed, “Challenges of using MIMO channel technology in 5G wireless communication systems,” *IEEE Majan International Conference (MIC)*, pp. 1-5, 2018.

[3] L. Zhang, Q. Feng, and M. K. Khan, “Design of a novel circularly polarized MIMO antenna with enhanced isolation for ultra-wideband communication,” *Applied Computational Electromagnetics Society (ACES) Journal*, vol. *37*, pp. 607-618, 2022.

[4] B. Arumita and V. Gupta, “Design and development of low-profile MIMO antenna for 5G new radio smartphone applications,” *Wireless Personal Communications,* vol. 111, pp. 1695-1706, 2020.

[5] *5G NR specifications*, document TS 38.101-1 V15.4.0, (3GPP Release 15, 2018).

[6] L. Yixin, Y. Luo, and G. Yang, “Multiband 10-antenna array for sub-6 GHz MIMO applications in 5-G smartphones,” *IEEE Access,* vol. 6, pp. 28041-28053, 2018.

[7] L. Kai-Chi, C. Wu, C. Lai, and T. Ma, “Novel dual-band decoupling network for two-element closely spaced array using synthesized microstrip lines,” *IEEE Transactions on Antennas and Propagation*, vol. 60, pp. 5118-5128, 2012.

[8] C. Hassan, “Compact high isolation wideband 4G and 5G multi-input multi-output antenna system for handheld and internet of things applications,” *International Journal of RF and Microwave Computer-Aided Engineering*, vol. 29, 2019.

[9] K. Saeed, A. Capobianco, A. Najam, I. Shoaib, E. Autizi, and M. Shafique, “Compact ultra-wideband diversity antenna with a floating parasitic digitated decoupling structure,” *IET Microwaves, Antennas and Propagation*, vol. 8, pp. 747-753, 2014.

[10] S. Li, S. W. Cheung, and T. I. Yuk, “Compact MIMO antenna for portable UWB applications with band-notched characteristic,” *IEEE Transactions on Antennas and Propagation*, vol. 63, pp. 1917-1924, 2015.

[11] D. Helena, M. R. Subasree, S. Susithra, S. S. Keerthika, and B. Manimegalai, “Mutual coupling

reduction in MIMO antenna system using EBG structures," *International Conference on Signal Processing and Communications (SPCOM)*, pp. 1-5, 2012.

[12] B. Anandrao and M. S. Kumbharm, "Wideband circularly polarized conformal strip fed three-layer hemispherical dielectric resonator antenna with parasitic patch," *Microwave and Optical Technology Letters*, vol. 56, pp. 72-77, 2014.

[13] Y. Chenyin, S. Yang, Y. Chen, W. Wang, L. Zhang, B. Li, and L. Wang, "A super-wideband and high isolation MIMO antenna system using a windmill-shaped decoupling structure," *IEEE Access*, vol. 8, pp. 115767-115777, 2020.

[14] I. Tariqul and M. Alam, "Compact EBG structure for alleviating mutual coupling between patch antenna array elements," *Progress in Electromagnetics Research*, vol. 137, pp. 425-438, 2013.

[15] K. Vasu and B. Anuradha, "Design of UWB MIMO antenna to reduce the mutual coupling using defected ground structure," *Wireless Personal Communications*, vol. 118, pp. 3469-3484, 2021.

[16] L. Yingsong, W. Li, C. Liu, and T. Jiang, "Two UWB-MIMO antennas with high isolation using sleeve coupled stepped impedance resonators," *IEEE Asia-Pacific Conference on Antennas and Propagation*, pp. 21-22, 2012.

[17] W. Yan and Z. Du, "A wideband printed dual-antenna system with a novel neutralization line for mobile terminals," *IEEE Antennas and Wireless Propagation Letters*, vol. 12, pp. 1428-1431, 2013.

[18] H. Jian-Rong and J. Li, "Compact microstrip antennas using CSRR structure ground plane," *Microwave and Optical Technology Letters*, vol. 56, no. 1, pp. 117-120, 2014.

[19] D. Chandu, S. Karthikeyan, and K. Kumar, "Reduction of mutual coupling in a two-element patch antenna array using sub-wavelength resonators," *Twenty-First National Conference on Communications (NCC)*, pp. 1-5, 2015.

[20] Y. Hui, J. Ding, C. Guo, Y. Qu, and Y. Song, "A wideband dual-polarized printed antenna based on complementary split-ring resonators," *IEEE Antennas and Wireless Propagation Letters*, vol. 14, pp. 410-413, 2014.

[21] Z. Anping and Z. Ren, "Multiple-input and multiple-output antenna system with self-isolated antenna element for fifth-generation mobile terminals," *Microwave and Optical Technology Letters*, vol. 61, pp. 20-27, 2019.

[22] S. Libin, H. Feng, Y. Li, and Z. Zhang, "Tightly arranged orthogonal mode antenna for 5G MIMO mobile terminal," *Microwave and Optical Technology Letters*, vol. 60, pp. 1751-1756, 2018.

[23] T. G. Abo-Elnaga, D. A. Salem, E. A. F. Abdallah, and H. El-Hennawy, "Wideband rectangular dielectric resonator antenna for S-band applications," *International Symposium on Antennas and Propagation*, pp. 1-6, 2006.

[24] E. Abdallah, T. G. Abo-Elnaga, and H. El-Hennawy, "Ground slotted phi shape UWB stacked circular polarized antenna for 5.8 GHz RFID reader," *Progress in Electromagnetics Research*, vol. 231, 2010.

[25] E. Abdallah, T. G. Abo-Elnaga, and H. El-Hennawy, "Ground slotted landa shape single feed UWB circular polarized antenna for 2.4 GHz RFID reader," *Progress in Electromagnetics Research*, vol. 225, 2010.

[26] S. Mohammad, "Printed multi-band MIMO antenna systems and their performance metrics," *IEEE Antennas and Propagation Magazine*, vol. 55, pp. 218-232, 2013.

[27] N. Jamal, M. Jamaluddin, M. Khalily, M. Kamarudin, I. Ullah, and R. Selvaraju, "A reduced size dual port MIMO DRA with high isolation for 4G applications," *International Journal of RF and Microwave Computer-Aided Engineering*, vol. 25, pp. 495-501, 2015.

Tamer Gaber Abouelnaga was born in Nov. 1976. He received his B.Sc. degree (1994-1999, honors degree) in electronics engineering from Menofiya University, Egypt, M.Sc. degree (2002-2007), and Ph.D. degree (2007-2012) in electronics and communications from Ain Shams University. He works as a researcher (2012-2017) and an associate professor (2018-now) in Microstrip Circuits Department, Electronics Research Institute, Egypt. He works as students affairs vice dean (2018-2019) and community service and environmental development vice dean (2019 till now) at the Higher Institute of Engineering and Technology, Kafr Elsheikh City. He has published 29 papers in peer-refereed journals, and 13 papers in international conferences regarding antennas, couplers, filters, and dividers for different microwave applications.

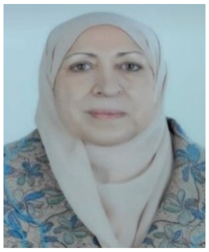

Esmat A. Abdallah (Senior Member, IEEE) graduated from the Faculty of Engineering, Cairo University, Giza, Egypt in 1968. She received her M.Sc. and Ph.D. degrees from Cairo University in 1972, and 1975, respectively. She was nominated as assistant professor, associate professor, and professor in 1975, 1980, and 1985, respectively. In 1989, she was appointed president of the Electronics Research Institute ERI, Cairo, Egypt, a position she held for about ten years. She became the Head of the Microstrip Department, ERI, from 1999 to 2006. Currently, she is at the Microstrip Department, Electronics Research Institute, Cairo, Egypt. She has focused her research on microwave circuit designs, planar antenna systems, and nonreciprocal ferrite devices, and recently on EBG structures, UWB components, and antenna and RFID systems. She acts as a single author and as a co-author on more than 285 research papers in highly cited international journals and proceedings of international conferences. She has six books and seven patents. She supervised more than 85 Ph.D. and M.Sc. theses. She is a member of the National Council of Communication and Information Technology.

Nanoarray of Vivaldi Rectenna for Infrared-energy Harvesting

Wided Amara[1], Abdelaziz Alzahrani[1,2], Ameni Mersani[3], Donia Oueslati[1], Ahmed Elsharabasy[4], Bandar Hakim[1], Hatem Rmili[1,2*], and Atef Elsherbeni[5]

[1]Electrical and Computer Engineering Department, Faculty of Engineering, King Abdulaziz University
P.O. Box 80204, Jeddah 21589, Saudi Arabia
hmrmili@kau.edu.sa

[2]K. A. CARE Energy Research and Innovation Center
King Abdulaziz University, Jeddah 21589, Saudi Arabia

[3]ESPRIT School of Business
ZI. Chotrana II, Tunis P.O. Box 160, Tunisia

[4]Electrical and Computer Engineering Department
McMaster University, Hamilton, ON L8S 4K1, Canada

[5]Electrical Engineering Department
Colorado School of Mines, Golden, Colorado 80401, USA
aelsherb@mines.edu

Abstract – This article presents the design of an array of rectennas operating at 28.3 THz for infrared (IR) energy harvesting applications. The basic element of the array consists of a Vivaldi-dipole rectenna composed of two arms made with different conductors (gold and titanium). A metal-insulator-metal (MIM) tunnel diode is used to rectify the THz ac current. The proposed MIM diode consists of a very thin layer of Al_2O_3 sandwiched between the two metal electrodes. Arrays of two, three, and four rectennas are investigated. The improvement of the energy captured by coupling several elements in the same structure with a common gap is also investigated. This array architecture, without feeding network, may reduce the number of rectifying diodes and, therefore, decrease losses and increase the overall efficiency. Finally, it has been found that the four-elements rectenna array has a maximum electric field intensity of 62.4×10^4 V/m at 28.3 THz.

Index Terms – Energy harvesting, infrared (IR) energy, MIM diode, rectenna, THz, Vivaldi antenna array.

I. INTRODUCTION

Nowadays, wireless sensor networks are widely used in several applications related to industry, surveillance, monitoring of people and objects, home automation, scientific research, etc. This rapid expansion in using wireless systems is due, among other reasons, to the considerable developments and advances made in microelectronics. These advances have enabled the integration of more and more functionalities in an increasingly smaller volume [1].

Unfortunately, research and development in energy storage technologies have not followed the same rapid trend. As a result, portable communications systems are finding themselves increasingly penalized regarding autonomy. To make these communication systems and objects more self-sufficient in energy and to increase the battery life, efficient electromagnetic energy harvesting systems are required. Collecting energy from the surrounding environment and converting it into usable electrical energy is a very interesting alternative to traditional usage of replaceable batteries [2]. These energy sources can be recovered from artificial devices or available natural sources [3–4].

The most direct and abundant source of energy comes from the Sun. Photovoltaic energy harvesting is a promising technology that converts solar energy in the visible spectrum into usable electrical energy [5], but this received energy from the sun is used in the visible region during the day only.

The energy released at night is in the infrared (IR) region within the spectral range 7-17 µm with a maximum power peak centred around the wavelength 10.6 µm (28.3 THz) [6–7]. In order to harvest and convert this available infrared energy, we need new devices to capture, convert, and store this energy. One solution that can exploit this abundant infrared energy from the

Submitted On: July 8, 2020
Accepted On: September 11, 2023

https://doi.org/10.13052/2023.ACES.J.380707

1054-4887 © ACES

Earth's surface is to use energy harvesting based on nano-rectennas [4, 8]. A rectenna-based system, is composed of a receiving antenna with integrated rectifying diode [9–11].

Harvesting energy in the IR domain requires efficient design of the antenna and the rectifying diode, with deep understanding of the dielectric properties of materials in the optical band, especially in the infrared range [4, 12, 13].

The continuous technological evolution of electronic and optical materials at the nano-metric scale quickly leads to the design of devices which were not even possible a few years ago. Plasmonics is one of areas that benefit most from these advances [14–15]. Optical antennas are strongly analogous to their radio frequency counterparts, but there are crucial differences in their physical properties and behavior when scaled. Most of these differences arise because metals are not perfect conductors at optical frequencies, but rather are highly correlated plasmas described as a free electron gas. By definition, an optical antenna is a device that converts freely the radiation of propagating light into localized electromagnetic energy, and vice versa [16]. The fabrication of optical antenna structures is an emerging opportunity for new optoelectronic devices [17]. Optical antennas help to exceed the diffraction limit, making it possible to manipulate, control and visualize optical fields at the nano-metric scale, which offers a wide range of applications [18]. Among these are antenna probes for nanoimaging, non-linear signal conversion, and IR energy harvesting. These nano-antennas require specific studies to develop optical antennas.

Associated with the antenna, IR energy harvesting is based on the use of diodes as rectifiers. In the terahertz domain, the use of diodes and more particularly of Schottky and MIM diodes, is very useful at the level of the rectifier block. MIM diodes are very attractive and promising candidates for energy recovery in the infrared spectrum. The MIM diodes are a good candidate for infrared (IR) applications of the electromagnetic spectrum because of their high-speed characteristics and their compatibility with integrated circuits [4, 19].

Usually, a single rectenna element cannot supply sufficient captured wireless power. To increase the power recovered by the system, we must maximize the power captured. One way to achieve this is by increasing the surface area of the antennas; however, this will shift the omni-directional bandwidth toward the low frequencies. Another approach is to combine several elements in an array configuration. Several configurations of the second approach are already presented in literature, but they all suffer from some limitations: In [20], a rectenna array based on a 2-by-4 misaligned bowtie antenna is presented. Four spiral elements composed of three gold-based square spiral nano-antennas resonate near 13 μm [21] with dimensions of 750 × 750 nm of each element. The system arrays have been coupled together in one structure with one common gap by using a feeding line. In both configurations cited in [20] and [21], the size of the feeding network is large compared to the array causing high ohmic losses, which reduce the intensity of the total collected electric field within the gap.

To increase further the captured electric field in arrays of nano-rectennas, authors in [22] optimized both the metal thickness of a bowtie nano array, (the optimal thickness was equal to 95 nm) in addition to the incident angle.

In this paper, we present a new design of nano-rectenna array, based on a Vivaldi rectenna operating at infrared wavelengths, with a maximum peak of collected power situated at 10.6 μm (28.3 THz). The structure is composed of an array of Vivaldi nano-rectennas placed in a configuration to create a hot spot in order to increase the intensity of the collected electric field within this localized zone. The main advantage of the proposed configuration is to remove the complex and lossy feeding network used in [22] and [23], in addition to the concentration of the electric field in one small region (hot spot) where the rectifying diode should be integrated. So, losses will be reduced, the captured electric field within the gap will be enhanced, and the total efficiency of the rectenna will be increased.

This article is organized as follows. Section II describes, respectively, the designs of one, two, three, and four antennas and their performances. The maximum fields captured for each case are presented. In section III, a similar study adds the rectifying MIM diode to form the rectennas. The design parameters of the Vivaldi nanoarrays are optimized to obtain maximum performance. The rectennas were simulated by using computer simulation technology (CST) software [24], where the dielectric properties of the metals (gold and titanium) are calculated based on the Drude-model.

II. VIVALDI NANO-ANTENNA

A. Vivaldi nano-antenna design

Currently, printed antennas are becoming more and more important because of the great variety of geometric shapes they can take, which make them applicable to different integration situations. This is a key property which explains the introduction of printed antennas in energy harvesting applications. This technology responds well to the needs of our application. Therefore, the design of the antennas must respond to compromises in terms of performance and complexity of implementation. The Vivaldi antenna is a simple planar antenna characterized by a wide band and linear polarization. The antenna element as shown in Fig. 1, presents an exponential curve profile in the XY plane. In The gap between the two arms of the antenna is defined by the following function [25]:

$$g(x) = R(e^{Cx} - e^{-Cx}) + \frac{W_{min}}{2}, \tag{1}$$

where the coefficient C is the curvature parameter, W_{min} is the width of the gap line, and R is defined by:

$$R = \frac{\frac{W_{max}}{2} - \frac{W_{min}}{2}}{e^{CL} - e^{C}}. \tag{2}$$

W_{max} is the opening width at the end of the arm and C is the length of the arm. The antenna configuration is symmetric around the x-axis.

The antenna element is composed of two arms: one in gold, with a dielectric constant $\varepsilon_{\mathrm{rg}}$, loss tangent tan δ_{g}, and a thickness h_{g}; and the other in titanium with a dielectric constant $\varepsilon_{\mathrm{rti}}$, loss tangent tan δ_{ti}, and a thickness h_{ti} separated by a gap W_{min}. A detailed parametric study allowed us to obtain the optimal values of the different parameters of the final structure Vivaldi antennas are described in Table 1.

The dielectric properties of gold, used in the simulations are obtained by presenting the experimental data in a Drude model [4]:

$$\varepsilon\,(\omega) = \varepsilon_{\infty} - \frac{{\omega_p}^2}{\omega^2 - i\omega\omega_{\tau}}, \tag{3}$$

where ε_{∞} represents the contribution of electrons linked to the relative dielectric constant, ω_p is the frequency of the plasma (rapid oscillation of the electron density in conductive media such as metals), and ω_{τ} is the amortization frequency.

Table 1: Antenna dimensions and material properties

Parameters	Value (μm)	Parameters	Value (μm)
Wmax	40	$\varepsilon_{\mathrm{rg}}$ at 28.3 THz	6037.7
Wmin	0.05	tan δ_{g} at 28.3 THz	0.4
L	2.7	$\varepsilon_{\mathrm{rti}}$ at 28.3 THz	430
$\mathrm{h_{ti}}$	0.08	tan δ_{ti} at 28.3 THz	0.98
hg	0.08	C	1.8

The advantage of this configuration is that it gives the designer the freedom to vary several antenna parameters in order to increase the electric field received. In addition, it produces a stronger electric field in its gap. Another advantage of Vivaldi's nano-antennas of this form is the ability to build an array by coupling many elements of the Vivaldi antenna in one configuration and combining the electric field of each element at the feed point of the network, where a rectifier can be integrated.

Light is an electromagnetic wave where the electric and magnetic fields are perpendicular to the direction of propagation (z-axis). To study the electric field at the antenna gap, a linear polarized plane wave (along x-axis) with an electric field module equal to 1 V/m (see Fig. 1). The electric field component of the incident field is along the dipole axis y, and the direction of propagation is perpendicular to the dipole (along -z). The maximum value of the collected field is concentrated at the gap with a value 67.2 V/m at 28.3 THz, as shown in Fig. 2.

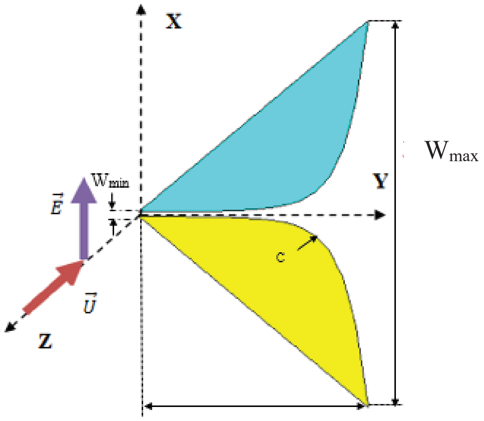

Fig. 1. Configuration parameters of the Vivaldi nano-antenna and direction of incident plane wave.

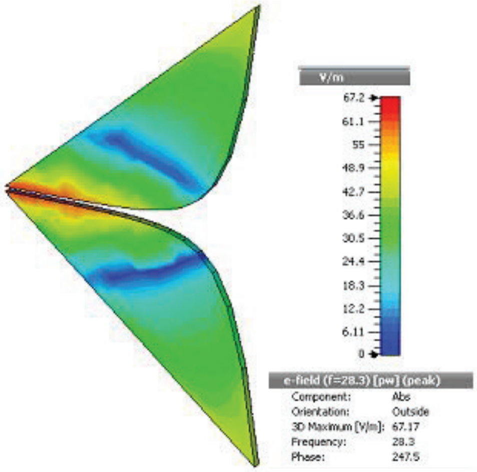

Fig. 2. Field distribution at 28.3 THz.

B. Vivaldi nano-antenna array

Vivaldi nano-antenna arrays have been used and studied due to their suitability for broadband operation and because they offer flexibility to optimize radiation properties by adjusting their configuration [22]. Figure 3 shows the configuration of the studied nano arrays. We started by designing a nanoarray of two elements to increase the captured electric field [26]. This network consists of two nano-antennas with a 30 nm gap to collect the electric field from the elements of the array, as shown in Fig. 3 (a). This simple design offers a higher electric field compared to a single element nano-antenna.

The dimensions of all nano-antennas in this array are the same as those in Fig. 1 with a slot of 30 nm separating the two identical nano-antennas. Figure 3 (b) shows three Vivaldi nano-antenna arrays based on gold and titanium, coupled together in a single network common gap. The nano-antenna arrays have been designed to resonate around 28.3 THz. Then, the four-element planar Vivaldi nanoarray, shown in Fig. 3 (c), has been designed to increase the electric field picked up for IR energy harvesting applications [22]. By coupling numerous elements in the geometry of an array, the far-field characteristics are improved and the output voltage is increased. In previous studies [8], methods of increasing the captured electric field by modifying the geometric parameters of the nano-antenna are presented. From the simulated results, the maximum electric field is produced by a 7 nm gap between the arms of the antenna. In addition, the captured electric field is improved if the size of the gap between the elements of the network at the supply point is reduced. Therefore, for the array of four elements, a Vivaldi nanoarray based on the optimized parameters is constructed to obtain maximum performance.

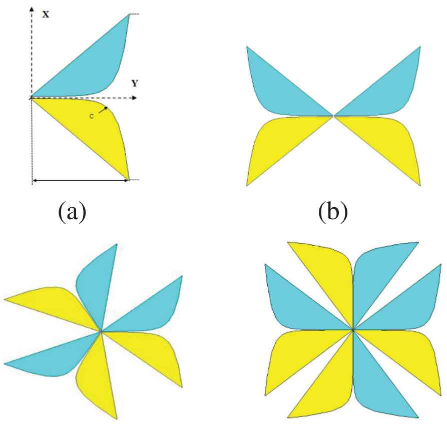

(a) (b)
(c) (d)

Fig. 3. Vivaldi nano-antenna: (a) single structure, (b) two elements array, (c) three elements array, and (d) four elements array.

C. Discussion

Figure 4 compares the solar energy harvesting capacities of the different arrays.

The intensity of single nano-antenna reaches a maximum value of 5×10^3 at 28.3 THz. The captured field is not sufficient with such a single-element antenna. However, this nano-antenna offers the possibility of capturing higher values by using it in a circular or hexagonal network by capturing the fields at the center of the array. In the case of a simple antenna, the received signal is often not sufficient to drive the rectifier. Thus, it is necessary to increase the gain of the receiving antenna by increasing its electrical size. This can be accomplished by assembling the single element antennas in a circular array configuration. The total field captured by the array is determined by the addition of the fields captured by each individual element when the elements interfere constructively. The factors which control the overall performances of an array with identical elements are presented in [26]: the geometrical configuration, the space between the elements, the amplitude and the phase of excitation of the elements, and the contribution of the individual element. As we can see in Fig. 4, it is obvious that the four-antenna nanoarray reaches a maximum value of 10^5 at 28.3 THz, which is better for harvesting the electric field compared to other designs. It can be seen that the field captured at the center increases by increasing the number of nano-antennas integrated into the array.

This significant improvement in the collected field strength obtained with the nanoarray is mainly due to the increase in numbers of dipoles used. and therefore the increase in its electrical size, at the resonant frequency.

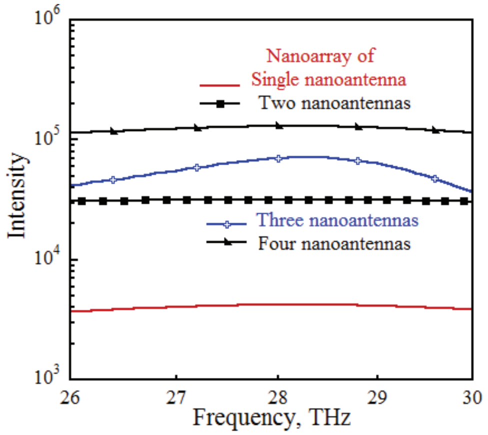

Fig. 4. The intensity variation captured vs. frequency for the different Vivaldi nanoarrays.

III. VIVALDI RECTENNA NANOARRAY

Electromagnetic energy harvesting systems require a wave receiving antenna connected to an RF/DC conversion system, thus forming a rectifier device or “Rectenna.” Currently, many challenges encountered in the design of rectennas for high performance are being studied. It leads to continuous progress in the understanding of light/matter interaction at optical frequencies. Recently, some researchers have shown a new low-cost nano-antenna manufacturing method [22].

Due to the geometric convenience of the dipole, the Vivaldi nano-antenna is chosen in this work to be the main resonator that integrates with the rectifier. However, the electric field picked up at the center of its gap is weak and needs to be further improved. That’s why an auxiliary resonant element is added to the structure, at the center of this nano-antenna, in order to increase the captured field and improve its overall performance.

Regarding diodes, many promising new alternatives are being explored. For example, metal-insulator-metal (MIM) diodes, metal insulator-insulator-metal diodes (MIIM), traveling wave diodes, pointy diodes, and geometric diodes have been considered as potential candidates for these applications.

In this work, firstly, the dipole nano-antenna is simulated. The field picked up at the feed gap level is shown in Fig. 4. After that, the optimized nano-antenna is exploited in the rectenna structure by inserting a MIM diode. In fact, a rectangular dielectric layer of Al_2O_3 with a permittivity equal to $\varepsilon r = 0.309 + j0.618$ at 28.3 THz, thickness 1.5 nm, and size 0.21 μm^2 is placed above the center of the simulated nano-antenna. A rectangular gold conductive layer of length d = 0.35 µm, width c = 0.2 µm, and thickness 0.14 µm is inserted as shown in Fig. 5 (a).

Then, the designed double nano-antenna, composed of four Vivaldi arms forming an array of two dipoles, is used to create a nano-rectenna array. These two elements have been coupled in the form of an array by adding a single diode, as shown in Fig. 5 (b).

A. Nano-rectenna array design

The MIM diode is used for IR rectification with the optical nano-antenna. The diode incorporates an insulator layer between two electrodes, which are sufficiently thin to allow tunnel conduction. To integrate the MIM diode into the nanoarray of two Vivaldi antennas, we followed the same principle of the MIM rectifier, an insulator layer of dimension 0.2 × 0.105 μm^2 and of the same thickness, then a conductive layer of gold of dimension 0.2 × 0.25 μm^2 is inserted in the same area of the diode.

The Vivaldi planar nanoarray (2 × 3) designed to increase the electric field picked up for solar energy collection applications is shown in Fig. 5 (c). The far-field characteristics are improved by coupling numerous elements in the form of an array, and the output voltage is increased. The dimensions of the MIM diode are each time modified in order to reach a maximum value of the field at the frequency of the resonance. A single diode was used for the network of three elements. The insulating layer of Al_2O_3 of dimension 0.2 × 0.215 μm^2 was used in the simulation. We have selected the conductive layer of gold of dimension 0.2 × 0.355 μm^2 in our study. Four Vivaldi elements, coupled together in a single array with a common gap, is shown in Fig. 5 (d). All of the features in Fig. 5 (d) have the same dimensions as the Vivaldi nano-antenna, as depicted in Fig. 1. A single diode was used for the array of three elements.

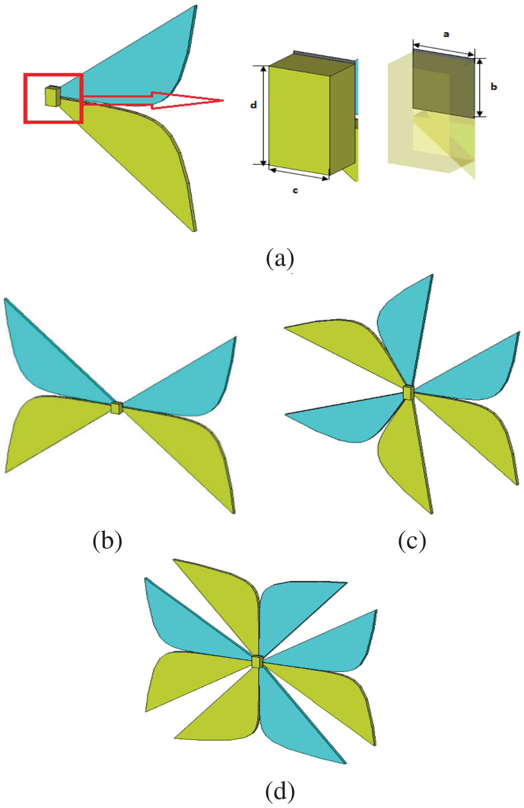

(a)

(b) (c)

(d)

Fig. 5. Nano-rectenna configuration: (a) single array, (b) two elements, (c) three elements, and (d) four elements.

IV. DISCUSSION

The electric fields captured inside the common gap of the one, two, three, and four-element nanoarray are calculated and plotted versus frequency from 26 THz to 30 THz, as shown in Fig. 6.

The Vivaldi nano-antenna array resonates at 13 µm. Furthermore, it is clear that the Vivaldi network with

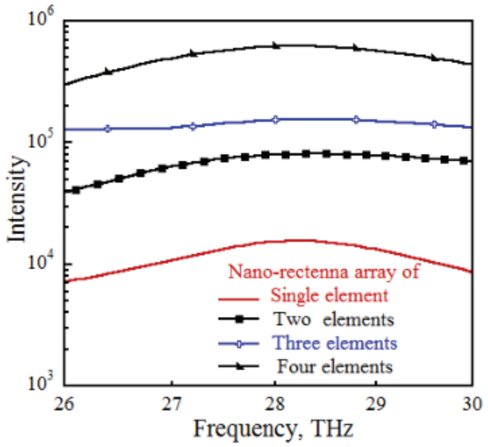

Fig. 6. The intensity variation vs. frequency for different studied nanoarrays.

four elements at the highest captured electric field, which is more than six times greater than that of the array with a single element. The intensity of the electric field increases by increasing the number of elements forming the nanoarray.

Thus, in this approach, the arrays designed have contributed to increasing the field of view at the level of the common gap when a single rectifier is necessary instead of two or more. This means that we have reduced the heat losses in the rectifiers and increased the total efficiency of the rectenna.

Table 2 summarizes the simulation results of the Vivaldi nano-rectennas designed. Vivaldi nano-rectennas resonate at 28.3 THz, and they always operate in the desired infrared band. Furthermore, it is clear that the Vivaldi array with four elements produces the highest captured electric field, which is more than double the highest value for the two-element array, and more than four times the highest value for the single Vivaldi element.

Table 2: Comparison between different Vivaldi nano-rectenna configurations

Array Element	**E-max (V/m)**	**Intensity**
One element	124	1.5×10^4
Two elements	284	8×10^4
Three elements	393	15.4×10^4
Four elements	790	62.4×10^4

V. CONCLUSION

A Vivaldi nano-antenna array for solar energy harvesting application at infrared frequencies 26-30 THz is designed and optimized. The first study is done to examine the captured field at the common gap for the single, double, three, and four nano-antenna with a resonant frequency of 28.3 THz. The second study is done by integrating a MIM diode into the designed arrays. The MIM diode is a very thin device made up of a very thin layer of Al_2O_3 sandwiched between two metal electrodes. It is noted that the resonant frequency for this array is 28.3 THz with a maximum electric field intensity of value 62.4×10^4 J for a nanoarray of four elements.

ACKNOWLEDGMENT

The Deanship of Scientific Research at King Abdulaziz University, Jeddah, Saudi Arabia has funded this project, under grant no. KEP-MSc: 41-135-1443. The authors also acknowledge the support provided by King Abdullah City for Atomic and Renewable Energy (K.A.CARE) under the K.A.CARE-King Abdulaziz University Collaboration Program.

REFERENCES

[1] X. W. Yao, D. B. Ma, and C. Han, “ECP: A probing-based error control strategy for THz-based nanonetworks with energy harvesting,” *IEEE Access*, vol. 7, pp. 25616-25626, 2019.

[2] A. Takacs, H. Aubert, S. Fredon, L. Despoisse, and H. Blondeaux, “Microwave power harvesting for satellite health monitoring,” *IEEE Trans. on Microwave Theory Tech*, vol. 62, no. 4, pp. 1090-1098, April 2014.

[3] F. Yildiz, “Potential ambient energy-harvesting sources and techniques,” *J. Technol. Studies*, vol. 35, no. 1, pp. 40-48, 2009.

[4] W. T. Sethi, “Optical antennas for harvesting solar radiation energy,” Ph.D. Thesis, Rennes University, 2019.

[5] R. Singh, G. F. Alapatt, and A. Lakhtakia, “Making solar cells a reality in every home: Opportunities and challenges for photovoltaic device design,” *IEEE Journal of the Electron Devices Society*, 2013.

[6] A. Yahyaoui, A. Elsharabasy, J. Yousaf, K. Sedraoui, and H. Rmili, “MIIM-based optical log spiral rectenna for efficient IR energy harvesting,” *Alexandria Engineering Journal*, vol. 61, no. 11, pp. 8897-8909, 2022.

[7] W. Amara, D. Oueslati, N. Eltresy, A. Alghamdi, K. Sedraoui, T. Aguili, H. Rmili, and R. Mittra, “Parametric study of modified dipole nano-antennas printed on thick substrates for infrared energy harvesting,” *Int. J. Numer. Model.*, e2704. https://doi.org/10.1002/jnm.2704, 2019.

[8] D. K. Kotter, W. D. Slafer, S. D. Novack, and P. Pinhero, “Solar antenna electromagnetic collectors,” *ASME*, Jacksonville, Florida, USA, 2008.

[9] M. Gadalla, M.-R. Abdelrahman, and A. Shamim, “Design, optimization and fabrication of a 28.3 THz nano-rectenna for infrared detection and rectification,” *Scientific Reports, 4:4270*, DOI: 10.1038/srep04270, Mar. 2014.

[10] W. Haboubi, H. Takhedmit, J.-D. L. S. Luk, S.-E. Adami, B. Allard, F. Costa, C. Vollaire, O. Picon, and L. Cirio, “An efficient dual-circularly polarized rectenna for RF energy harvesting in the 2.45 GHz ISM band. *Progress in Electromagnetics Research,* vol. 148, pp. 31-39, ff10.2528/ PIER14031103ff, 2014.

[11] C. A. Reynaud, D. Duché, J.-J. Simon, E. Sanchez-Adaime, O. Margeat, J. Ackermann, V. Jangid, C. Lebouin, D. Brunel, F. Dumur, D. Gigmes, G. Berginc, C. A. Nijhuis, and L. Escoubas, “Rectifying antennas for energy harvesting from the microwaves to visible light: A review,” *Progress in Quantum Electronics, Elsevier*, vol. 72, p. 100265, 2020.

[12] O. P. Dimitriev, “Harvesting of the infrared energy: Direct collection, up-conversion, and storage,” *Optoelectronics and Optoelectronic Devices*, SPQEO, vol. 22, no. 4, pp. 457-469, 2019.

[13] J. Shank, E. A. Kadlec, D. W. Peters, and P. S. Davids, “Infrared nanoantenna-coupled rectenna for energy harvesting,” IEEE Aerospace Conference, Big Sky, MT, USA, pp. 2-9, March 2019.

[14] P. Biagioni, J. S. Huang, and B. Hecht, “Nanoantennas for visible and infrared radiation,” *Rep. Prog. Phys.*, vol. 75, no. 024402, 2012.

[15] C. De Angelis, A. Locatelli, D. Modotto, S. Boscolo, M. Midrio, F. Sacchetto, A. D. Capobianco, F. M. Pigozzo, and C. G. Someda, “Extending antenna theory to the optical domain,” *2009 European Microwave Conference (EuMC)*, 2009.

[16] G. A. E. Vandenbosch, *Plasmonics - Principles and Applications,* intechOpen, 2012.

[17] M. Mivelle, “Etude et developpement de nanoantennes brees pour la microscopie en champ proche optique et la nano-photonique,” Ph.D. Thesis, September-October 2009.

[18] J. Paparone, “Contrôle de l’émission dans des nano-structures plasmoniques: Nanoantennesmultimères et plasmons long-range,” Optique/photonique, Ph.D. Thesis, Université Lyon 1 – Claude Bernard, 2016.

[19] E. G. Arsoy, M. Inac, A. Shafique, M. Ozcan, and Y. Gurbuz, “The metal-insulator-metal diodes for infrared energy harvesting and detection applications,” *Proc. SPIE 9819, Infrared Technology and Applications XLII*, May 20, 2016.

[20] M. Aldrigo, D. Masotti, V. Rizzoli, and A. Costanzo, “Design rules for innovative nanorectennas in the infrared region,” *2013 European Microwave Conference*, Nuremberg, pp. 1-4, 2013.

[21] A. Sabaawi, C. Tsimenidis, and B. Sharif, *Rectenna Solar Cells. 10.1007/978-1-4614-3716-1_*11, 2013.

[22] A. M. A. Sabaawi, C. C. Tsimenidis, and B. S. Sharif, “Planar bowtie nanoarray for Thz energy detection,” *IEEE Transactions on Terahertz Science and Technology*, vol. 3, no. 5, pp. 1-8, 2013.

[23] A. M. A. Sabaawi, C. Tsimenidis, and B. Sharif, “Bow-tie nano-array rectenna: Design and optimization,” *Antennas and Propagation (EUCAP), 2012 6th European Conference on IEEE*, pp. 1975-1978, 2012.

[24] CST Microwave Studio, ver. 2012, *Computer Simulation Technology*, Framingham, MA, 2012.

[25] C. A. Balanis, *Antenna Theory: Analysis and Design*, 2005.

[26] A. W. A. Sabaawi, C. C. Tsimenidis, and B. S. Sharif, “Infra-red nano-antennas for solar energy collection,” *Loughborough Antennas and Propagation Conference (LAPC)*, pp. 1-4, 2011.

Wided Amara has received her B.S. in industrial electronics engineering in October 2015, and the M.S. in smart systems for communication in November 2016, from the National Engineering School of Sousse (ENISO, Tunisia). She received her Ph.D. in tele-communications within the SysCom laboratory, ENIT, Tunis, Tunisia, in 2021. Her field of interest is infrared energy harvesting.

Abdulaziz Alzahrani was born in Abha, Saudi Arabia, May 1988. He received the MSc. degree in iElectronic / communication engineering with the Department of Electrical Engineering, King Abdul- Aziz University, Jeddah, Saudi Arabia, in 2023. His research interests include energy harvesting, renewable energy, nano-technology, and green power generation.

Ameni Mersani received a degree in electronics, computer and information science from the University Tunis El Manar, Tunisia, in 2009 and the master thesis in electronics from the Faculty of Science of Tunis, Tunisia, in 2012. She received a Ph.D. in engineering sciences (electronics) from the University of Tunis El Manar, 2018. From September 2018, she has been working as a research assistant in ISET’COM (Department of Telecommunication). From December 2019, she has been a post-doctoral researcher with King Abdulaziz University, Saudi Arabia. Her research mainly focuses on the development of the design of wearable antennas for wireless applications and metamaterials, dipole antennas, and infrared energy harvesting.

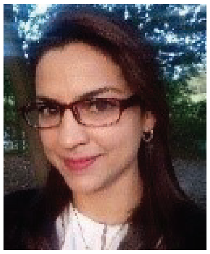

Donia Oueslati received a degree in electronics, computer and information science from the University Tunis El Manar, Tunisia, in 2008 and the Master thesis in system of communications from National Engineering School of Tunis, Tunisia, in 2011. She received the Ph.D. in engineering sciences from Université Catholique de Louvain, Belgium, and in telecommunication from UTM in 2017. From April 2017 to August 2018, she was a post-doctoral researcher with Antenna Lab, Université Catholique de Louvain, in collaboration with HEC research center, EMC Lab, University of Central Florida, Orlando, Florida, USA, and ECE Department, King Abdulaziz University, Saudi Arabia. Since September 2018, she has been working as research assistant at University Catholique de Louvain. Her research mainly focuses on the development of a modal analysis methods for printed structures based on the Method of Moments and singular decomposition to identify a chipless radio frequency identification (RFID) and to localize a reader. Her research interests include ultra-wideband (UWB) optical rectennas for solar energy harvesting, investigation of irregular fractal antennas, and low-profile antenna array and array optimization for 5G applications.

Ahmed Y. Elsharabasy received a B.Sc. degree in electronics and communications engineering from Cairo University, Egypt, in 2004 with distinction (honors). He joined the Department of Engineering Mathematics and Applied Physics, Cairo University as a teaching and research assistant. In 2012, he received a Master's degree in engineering mathematics from Cairo University. His master focused on yield optimization of EM-based structures. In this research he carried out statistical optimization using space-mapping surrogates, and utilized HFSS to simulate the microwave circuit performance. In 2014, he joined the Electrical and Computer Engineering Department at McMaster University, Canada, as a Ph.D. researcher on IR and THz energy harvesting. His research focused on design, modeling, optimization, fabrication, and characterization of rectenna devices for ambient (waste) thermal energy harvesting and detection applications. He also introduced novel designs of optical antennas and perfect metamaterial absorbers. Additionally, he succeeded in tuning the performance of metal-mesh THz filters via topology optimization to fit with specific applications. He received the McMaster International Excellence Award in 2016, 2017, and 2018. In 2020, Ahmed joined the University of Toronto, Canada, as a postdoctoral research fellow to develop low-power, large-area optical phased array for free-space optical communication in satellite and space applications.

Ahmed is a member of IEEE, OSA, SPIE. He is currently a visiting scholar in the Electrical and Computer Engineering Department at McMaster University, Canada. Elsharabasy is author/coauthor of 17 journal and conference papers and presentations. His research interests include nano-antennas, MIM diodes, plasmonics, photonics, energy harvesting, and optimization.

Bandar Hakim is an assistant professor of electrophysics at KAU. He received his Ph.D. degree in electrophysics from the University of Maryland. He worked with the Medical Robotics group at the École Polytechnique Fédérale de Lausanne in Switzerland, the Center for Devices and Radiological Health at the Food and Drug Administration in Washington, DC, and the Neurology department at Mount Sinai School of Medicine in New York, NY. He served as an industrial consultant in the US, Switzerland, and Germany.

Hatem Rmili received the B.S. degree in general physics from the Science Faculty of Monastir, Tunisia, in 1995, and the DEA diploma from the Science Faculty of Tunis, Tunisia, in quantum mechanics, in 1999. He received the Ph.D. degree in physics (electronics) from both the University of Tunis, Tunisia, and the University of Bordeaux 1, France, in 2004. From December 2004 to March 2005, he was a research assistant in the PIOM laboratory at the University of Bordeaux 1. From March 2005 to March 2007, he was a postdoctoral fellow at the Rennes Institute of Electronics and Telecommunications, France. From March to September 2007, he was a postdoctoral fellow at the ESEO Engineering School, Angers, France. From September 2007 to August 2012, he was an associate professor with the Mahdia Institute of Applied Science and Technology (ISSAT), Department of Electronics and Telecommunications, Tunisia. He is associate professor with the Electrical and Computer Engineering Department, Faculty of Engineering, King Abdulaziz University, Jeddah, Saudi Arabia.

Rmili's research interests concern applied electromagnetic applications involving antennas, metamaterials, and métasurfaces. The main targeted applications are reconfigurable antennas for multi-standard wireless communications systems, security of chipless RFID systems with fractal tags, terahertz photoconductive antennas for infrared energy harvesting, UWB nanorectennas for collection of solar energy, phase shifters for low-cost 5G communication systems, and microwave absorbing materials for stealth technologies.

Atef Z. Elsherbeni started his engineering career as a part-time software and system design engineer from March 1980 to December 1982 at the Automated Data System Center, Cairo, Egypt. From January to August 1987, he was a post-doctoral fellow at Manitoba University. He joined the faculty at the University of Mississippi in August 1987 as an assistant professor of Electrical Engineering. He advanced to the rank of associate professor in July 1991 and the rank of professor in July 1997. He was the director of The School of Engineering CAD Lab from August 2002 to August 2013, and the director of the Center for Applied Electromagnetic Systems Research (CAESR) from July 2011 to August 2013. He was appointed Associate Dean of Engineering for Research and Graduate Programs from July 2009 to July 2013 at the University of Mississippi. Elsherbeni became the Dobelman Distinguished Chair and Professor of Electrical Engineering and Computer Science at the Colorado School of Mines in August 2013. He was appointed as adjunct professor, at the Department of Electrical Engineering and Computer Science of the L.C. Smith College of Engineering and Computer Science at Syracuse University, in January 2004. He spent a sabbatical term in 1996 at the Electrical Engineering Department, the University of California at Los Angeles (UCLA) and was a visiting professor at Magdeburg University during the summer of 2005 and at the Tampere University of Technology in Finland during the summer of 2007. In 2009, he was selected as Finland Distinguished Professor by the Academy of Finland and TEKES. Elsherbeni is a fellow member of the Institute of Electrical and Electronics Engineers (IEEE) and a fellow member of The Applied Computational Electromagnetic Society (ACES). He is the editor-in-chief for ACES Journal and a past associate editor to the Radio Science Journal.

THz Microstrip Antenna for Terabit Wireless Local Area Networks

V. Koushick,[1] C. Divya,[2] M. Vinoth,[3] E. A. Mohamed Ali,[4] and M. Sugadev[5]

[1]Department of Electronics & Communication Engineering
Vel Tech Rangarajan Dr. Sagunthala R&D Institute of Science and Technology, Avadi, Chennai, Tamilnadu
koushickvenkat@gmail.com

[2]Centre for Information Technology & Engineering
Manonmaniam Sundaranar University, Tirunelveli, Tamilnadu
cdivyame@gmail.com

[3]Department of Electronics & Communication Engineering
K. Ramakrishnan College of Engineering, Samayapuram, Trichy, Tamilnadu
vinothmecs@outlook.com

[4]Department of Electronics & Communication Engineering
JP College of Engineering, Tenkasi
mummarabi2011@gmail.com

[5]Department of Electronics & Communication Engineering
Sathyabama Institute of Science and Technology, Chennai
Sugadev74@gmail.com

***Abstract* –** In order to replace millimetre wave communication for extremely fast terabit wireless local and personal area network connectivity, researchers have been looking into the possibilities of the terahertz band for establishing wireless data communication at terabit rates. The IEEE 802.15 WPAN Terahertz Interest Group (IGTHz) has been created to encourage research in the terahertz bands and set standards for their use, in order to facilitate progress and advancement in this area. The specific objective of this study is to design and analyze a microstrip antenna working at 3.5 THz resonant frequency. The proposed novel antenna includes three layers: a top layer that represents the patch, a second layer that represents the substrate, and a bottom layer that represents the ground plane. It is designed using a 32 nm thin FR-4 substrate with a permittivity of 4.4. Using HFSS simulations, it was found that the proposed antenna has an overall efficiency greater than 85% within the working frequency range of 3.5 THz. Additionally, it exhibited an extremely low reflection coefficient (S_{11}) of -43.61 dB at 3.5 THz, with an efficiency exceeding 80%. This simple and broadband antenna design could have relevance in high-speed data transmission networks.

***Index Terms* –** Microstrip patch antenna, multilayer technique, terahertz frequency band, *THz antenna*.

I. INTRODUCTION

Over the past few years, the manner in which individuals consume, exchange, and generate information has changed, leading to significant growth in wireless data traffic. This has led to an increasing demand for faster wireless connections that can be used anytime, anywhere. Over the last 30 years, the speed of wireless data has increased twofold every 18 months, and it is now reaching the point where it can match the capacity of conventional communication networks. If present trends persist, it is anticipated that wireless networks capable of transmitting terabits of data per second (Tbps) will be present in the next 10 years [1]. Nevertheless, to cope with such exceedingly high data rates, innovative physical layer technologies and novel spectral bands will be needed [2].

"Terahertz (THz) communication" and "sub-THz communication" relate to the usage of frequencies falling within the ranges of 0.1-10 THz and 0.1-0.3 THz [1]. As a result of the need for rapid data transmission over short distances, these frequency ranges have become increasingly important. The terahertz spectrum is capable of transmitting data at high speeds within a range of 10 metres, making it useful for tiny cell cellular networks. Terahertz communication has the ability to be utilized

Submitted On: June 23, 2022
Accepted On: February 23, 2023

https://doi.org/10.13052/2023.ACES.J.380708

1054-4887 © ACES

by both stationary and mobile users, as well as in indoor and outdoor settings. Terabit wireless LAN (T-WLAN) offers a way to connect personal computers and tablets to high-speed fiber optic connections. Both cable and wireless channels move data at the same speed in THz communication [2]. Despite the advantages of THz frequencies, communication at these frequencies is challenged by high path loss, which places a severe constraint on communication durations. Further challenges involved in developing dense, high-power transceivers that operate in the THz band include effective radiators that work across an ultra-broadband of THz frequencies, characterizing frequency-selective route loss in the THz band channel, and devising new modulations, transmission strategies and communication protocols that are optimized for the unique features of this band. The THz spectrum is currently unregulated due to these challenges and because many of them are also shared by millimetre wave (mmW) communication systems [3]. However, the radiator size can be decreased to less than a millimetre, which is a huge benefit of THz and sub-THz frequencies.

Recent advancements in photonic and semiconductor devices have led to the realization of systems operating at Terahertz (THz) frequencies. In such systems, antennas are often fabricated on small substrates before being integrated with active components. However, the integration of on-chip radiators with lossy substrates results in lower efficiency. To address this issue, substrate integration technology has been proposed as a solution, which involves transforming nonplanar antenna designs into planar forms.

While research into achieving Tbps data rates is still in the initial stages, THz communication has the capability of achieving data rates in the Gbps range [4]. Some studies have suggested that polarization multiplexing could be used to achieve Tbps data rates [5]. A newly proposed frequency range in the electromagnetic wave spectrum of THz, which lies between microwaves and infrared light, could enhance data transmission rates [6].

After the ITU World Radiocommunication Conference in 2019, where the frequency band of 275-450 GHz was designated for fixed and land mobile services, researchers have become more interested in THz wireless communication technology. The frequency range of THz waves is defined by the IEEE standard as 0.3-10 THz [7], with a corresponding wavelength range of 0.03-3 mm. These electromagnetic waves have a frequency band of 0.1-10 THz. The THz wave exhibits the following remarkable characteristics:

A. Low damage

Compared to X-rays, THz waves have a lower single photon energy by approximately one part in a million. Consequently, THz waves do not pose a threat to living organisms and can be used for various biomedical applications, such as body scanning for skin cancer, to aid in medical treatment [8].

B. High spectral resolution

Several important compounds have their spectra in the THz range, and analyzing the THz radiation spectrum is necessary to detect harmful objects such as viruses, toxins, and grenades, among others [9].

C. Visualization

Due to their short wavelengths, THz waves can penetrate through different non-metallic or non-polar materials. They can also be converted from opaque to visible opaque objects by THz wave scanning, which can provide higher-resolution images. As a result, THz waves have a significant potential for use in sensing applications, including typical full-body scanners at airports.

D. Wide bandwidth

A THz wave is the electromagnetic wave with the broadest frequency range in electronics. Using THz waves as the signal carrier can significantly increase the speed of information transmission, potentially up to Tbps. The field of THz wave sensing applications has advanced rapidly, but THz antenna applications are not yet fully developed. Due to the limited availability of spectrum resources, antennas are being constructed at higher frequency bands. Compared to typical antennas, THz band antennas provide much higher bandwidth, owing to the broadband performance of the THz spectrum. THz waves offer several advantages over millimetre and light waves, including a wider effective frequency band, stronger beam direction, improved secrecy, and anti-interference performance. THz waves are also more efficient and can penetrate deeper than light waves [11].

The broad operational bandwidth of THz antennas is a result of the distinct features of THz waves and plays a crucial role in maximizing performance. The development of THz antennas is required for the usage of THz waves in wireless networks. The operating bandwidth and antenna gain of the system are both directly impacted by the performance of these antennas. The throughput, imaging resolution, and detecting capacities of the system are also highly related to how THz antennas perform. Due to the special characteristics of THz waves, such as their wideband spectrum, high precision, remarkable directivity, and low cost, THz antennas have a variety of benefits. However, designing THz antennas is challenging due to the limitations of materials and manufacturing techniques that restrict the size of THz antennas. Additionally, THz antennas face additional difficulties compared to microwave antennas, such as establishing successful radiating techniques [12]. When it comes to THz antennas, stricter requirements must be followed for the type of antenna, materials used, and manufacturing techniques employed. Sophisticated microfabrication methods, such as slot array, reflector, horn, dipole, and leaky wave antennas, are used to design THz antennas. For sub-THz systems, compact form factor, high gain, and wide bandwidth designs are preferred.

Previous research has reported several methods for reducing link noise, including a multilayer rectangular cavity design on an InP substrate. This design produced a broad impedance bandwidth of 38 GHz at 300 GHz with only 4 dBi gain [13]. Another study utilized CMOS on-chip technology to create a microstrip patch antenna with four resonators on top. This method resulted in a broadband sub-THz antenna with a central frequency of 10% fractional bandwidth and 15% radiation efficiency [14]. However, both studies faced challenges with antenna size and trade-offs between bandwidth, gain, and structure complexity.

The challenges in developing sub-THz antennas arise from the high precision required during manufacturing and measuring. Despite the existence of numerous techniques for constructing sub-THz antennas at 300 GHz, obtaining high gains, wide bandwidths, and complex structures remains challenging. To tackle this issue, the authors propose an antenna design strategy that achieves high gains and wide bandwidth at sub-THz frequencies. Their approach involves a dipole-based single-element design with significantly increased bandwidth and adequate gain. The authors plan to incorporate alternative radiating directors and array designs to enhance the structure's gain, while still maintaining its compact form and wide bandwidth.

II. NUMERICAL ANALYSIS

The authors were not able to access the expensive equipment required to fabricate and test THz antennas at such high frequencies when this study was conducted. Even with the adoption of specific methods, such as batch processing, the fabrication of a highly efficient coupling port between the source and the antenna is still challenging, especially for thin substrates. Therefore, the authors employed numerical analysis to validate the antenna's performance. As a result of its availability and lower cost, FR4 was selected as the substrate for the designed antenna.

The increasing amount of mobile traffic, projected to reach 327 petabytes by 2015, highlights the need for practical and high-speed wireless networks. As the ITU has not allocated frequencies above 275 GHz for any specific purpose, the THz frequency band is a promising option for high-speed communication. Although still in its early stages, THz communication technology has a promising future [15], as demonstrated by the hypothetical wireless personal area network design with THz connections proposed by the U.S. Federal Communications Commission (Fig. 2) and the secure military wireless THz communication network depicted in Fig. 1. Increasing carrier frequencies has been the primary approach to achieve higher data rates, with rates of 10-100 Gbps translating to frequencies of around 100-500 GHz [16]. Additionally, using frequencies over 300 GHz results in smaller antenna sizes that are sub-millimetre in scale.

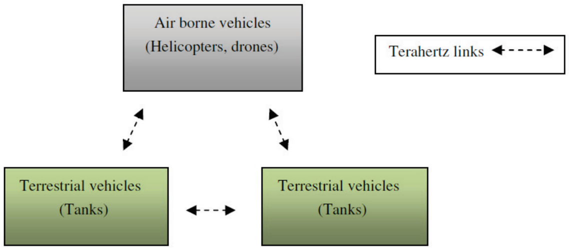

Fig. 1. Wireless THz communication network.

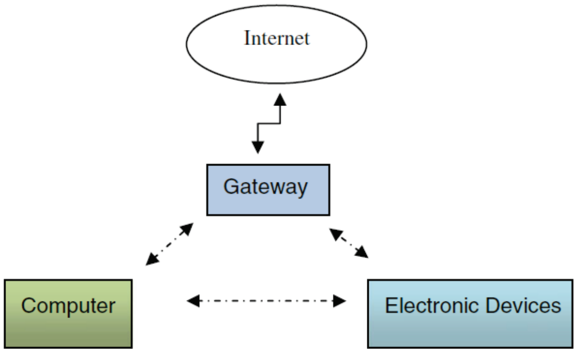

Fig. 2. WPAN design with THz connections.

Due to recent advancements in photonic and semiconductor technology, it is now possible to deploy terahertz-based systems. The development of Si-based VLSI control systems, MEMS-based devices, and metamaterials for antennas are essential for THz communications [17]. A high-frequency photodiode capable of producing frequencies between 300 and 400 GHz was reported in [18], with a frequency-to-output power ratio determined through heterodyning at 1.55 μm. This photodiode could transmit error-free data at a rate of 2 Gbps at 300 GHz with a transmitted power of 10 W. It had a 140 GHz bandwidth (ranging from approximately 270 to 410 GHz), a maximum output power of 110 W at 380 GHz, and a photocurrent of 20 mA, which is equivalent to a peak output power of 440 W. These are the features described in the article. Because THz frequencies are highly attenuated by atmospheric conditions, outdoor data transmission is not feasible, making it suitable only for short-range indoor applications [18]. The properties of short-range linkages can be estimated using the Friis formula in Equations (1) and (2) as given below:

$$P_r = P_t + G_t + G_r + 20 \cdot \log\left(\frac{\lambda_c}{4 \cdot \pi \cdot d}\right) - L_{\text{additional}} - \{\alpha \cdot f_c \cdot d\}. \quad (1)$$

$$SNR\ (dB) = P_r - \{N_0 + 10.\log B + NF + M\}. \quad (2)$$

P_r stands for received power, P_t for transmitted power, and G_t and G_r, respectively, for the transmitter and receiver antenna gains. The wavelength is represented by λ, distance by d, and the air attenuation by α. The system's noise figure, noise margin, and bandwidth are NF, M, and B, respectively. The THz band, which is made up of tiny cells in a cellular network, can be used for high-speed data transmission within a 10 m radius. THz communication can be used to serve stationary and moving users both inside and outside. T-WLAN enables fast communication between personal electronics like tablets, laptops, and fiber optic cables. In THz communication, both wireless and wired lines communicate at the same speed, enabling bandwidth-concentrated services like wireless data distribution and excellent video conferencing in small spaces. Additionally, THz communication is ideal for military and defence applications utilizing encrypted communication networks.

Massive antenna arrays are required in the THz band to overcome coverage area limitations and transmission losses due to atmospheric attenuation. This results in narrow antenna beams that decrease the likelihood of eavesdropping. Additionally, multiple spread spectrum techniques can be employed to counteract signal jamming attempts. Consequently, the proposed THz antenna is ideal for high-speed communication networks. A typical microstrip patch antenna (MPA) consists of three layers: the top layer, substrate layer, and ground plane. The rectangular patch is created on the top layer and is supported by the substrate layer in the middle. The operating frequency for the proposed terahertz MPA is 3.5 THz, and the thickness of the microstrip patch layer is usually much smaller than the wavelength. However, in this case, the operating frequency is higher, so the thickness value is very small. Therefore, to avoid the design and production constraints depicted in Fig. 3, the thickness value is increased. The proposed THz microstrip patch antenna uses a flame retardant (FR4) substrate and has a geometric design size of 1800 × 1800 × 36 nm^3. The antenna being suggested has dimensions that are mainly in the nanometre range. Table 1 shows the calculated design parameters. The transmission bandwidth of THz waves is much wider than that of mobile communication, as their frequency range is about 1000 times greater.

Numerous research teams and organizations have shown interest in THz technology as a potential solution for achieving high data rates in wireless communication systems [19–21]. Compared to mmW systems, THz systems offer a significantly higher capacity and faster data transfer rate, making it a promising candidate for ultra-high-speed wireless communication. THz communication is mainly used for short-distance terrestrial applications and space communication. Despite the fascination of THz waves in the environment, their high transmission rate and strong secrecy meet current demands. Due to its potential for high-speed data transfer, the THz communication system has garnered the attention of many nations, resulting in numerous studies. THz antennas have progressed rapidly and are available in a variety of shapes, such as dielectric lens photoconductive antennas, planar antennas, bowtie dipoles, pyramid-shaped cavities with dipoles, angle reflector arrays, carbon material-based THz antennas, and many more. Conductive antennas, hydrophobic antennas, and innovative technological antennas based on the material used in their development are the three main types of THz antennas. A dielectric antenna consists of a substrate material and an antenna radiator, achieving impedance matching with the detector through proper design and providing a simple, easy integration, and low-cost approach.

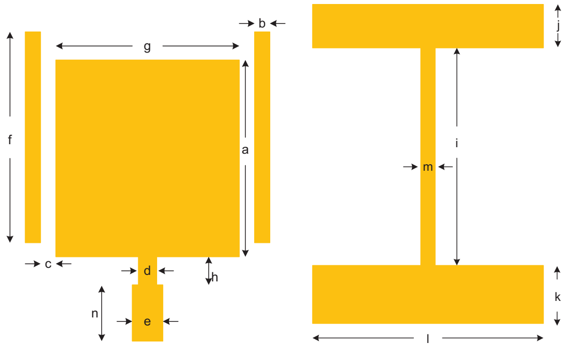

(a) (b)

Fig. 3. Proposed 3.5 THz MPA structure: (a) radiating layer, (b) bottom layer.

Using the patch antenna cavity model, the following formula can be used to determine the resonant frequency of the propagation modes (TMmn) in the microstrip [22].

Table 1: Size of the proposed MPA

Dimensional Parameter	Dimension	Description
a	1100 nm	Width of the patch
b	200 nm	Width of parasitic patch
c	150 nm	Gap between active patch and parasitic patch
d	200 nm	Width of feedline
e	300 nm	Width of stub
f	900 nm	Height of parasitic patch
g	700 nm	Length of the patch
h	800 nm	Length of feedline
i	1000 nm	Tapered line of the patch
j	300 nm	
k	500 nm	
l	1800 nm	
m	200 nm	
n	500 nm	Length of stub

The proposed MPA can be designed using equations (3) and (4) as follows:

$$f_{mn} = \frac{c}{2\sqrt{\varepsilon_{eff}}}\sqrt{\left(\frac{m}{a}\right)^2 + \left(\frac{n}{b}\right)^2}, \tag{3}$$

$$\varepsilon_{eff} = \frac{\varepsilon_r + 1}{2} + \frac{\varepsilon_r - 1}{2}\left[1 + 12\frac{t_1}{a}\right]^{-0.5}. \tag{4}$$

Theoretically, equation (1), which takes into account the rectangular patch's dimensions *a* and *b*, as well as positive integers *m* and *n*, determines the effective relative permittivity (*eff*). When the dimensions *a* and *b* and the permittivity of the substrate layer are known, equation (2) can be used to get the resonant frequency of the dominant mode (TM01). The resonant frequency of TM01 can be altered by adjusting the dimensions *a* and *b* of the patch, which allows for higher modes to propagate within the dominant frequency range. In this research, Section 3 describes the design process for determining the values of *a* and *b*. The proposed design employs an FR4 substrate layer that measures 1800 × 1800 × 36 nm^3.

The Q-factor of MPA for a given resonant frequency is related as:

$$\frac{\Delta f}{f_r} = \frac{1}{Q_{fr}}. \tag{5}$$

The bandwidth is represented by Δf, the resonant frequency is represented by f_r, and the *Q*-factor at the resonant frequency is represented by Q_{fr}. At the dominant mode of the antenna, the gain and quality factors are related as

$$Q_{rf} = \frac{2\omega\varepsilon_r LW}{4hG_{rf}}, \tag{6}$$

where angular frequency, length, and width of the patch and height of the substrate are represented by ω, L, W, and h, respectively.

Due to higher operating frequency in THz range, the dielectric loss of the antenna is significant and is given by the expression

$$\alpha_{dl} = \pi\frac{(\varepsilon_e - 1)\varepsilon_r \tan\delta}{(\varepsilon_r - 1)\varepsilon_e\lambda_g} Np/unit - length, \tag{7}$$

where α_{dl} is the dielectric attenuation loss in nepers (Np) due to the substrate, λ_g is the guide wavelength, and δ is loss tangent. To reduce the effect of dielectric loss, the thickness of the substrate is kept very small.

The conductor loss of the proposed antenna is expressed as

$$\alpha_{cl} = \frac{R_s}{Z_c W_m}\text{Np/unit-length}, \tag{8}$$

where $\alpha_{cl}$is the conducting loss, $R_s$is the surface resistance, $Z_c$is the characteristic impedance, and W_m is the width of the conducting region in the antenna. To reduce conducting losses, the thickness of the conducting copper layer is kept below 15 μm.

III. RESULTS AND DISCUSSION

The proposed THz MPA was simulated in HFSS with a frequency range of 3.5 THz. The simulation results are presented in Fig. 4, showing the plotted S parameters (transmission and reflection coefficients) versus the operating frequency. The simulation indicates a maximum return loss value of approximately -43.61 dB and a voltage standing wave ratio (VSWR) of 1.013, as illustrated in Fig. 5. Based on Fig. 5, the VSWR value is less than 2 in the 3.5 THz working frequency region. The return loss is a function of VSWR [23], which indicates how effectively the radiator is matched to the transmission line or microwave to which it is coupled. A VSWR value between 1 and 2 [22–26] is considered optimal for minimal reflection losses. Antenna values are generally reported with some degree of optimism and accuracy.

The amount of power given to the radiator doesn't always get radiated, and matching the antenna with transmission lines is made easier by a low VSWR value. To evaluate the performance of an antenna, the ratio of power sent to a reference antenna compared to that

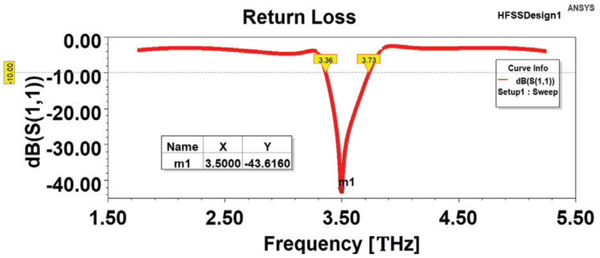

Fig. 4. Simulated return loss value at 3.5 THz.

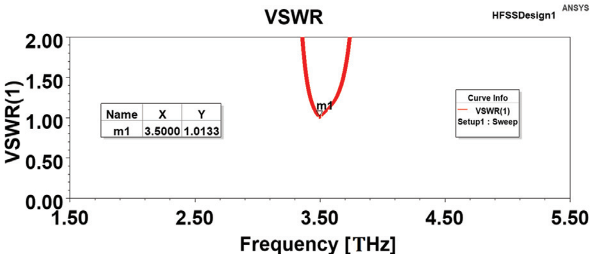

Fig. 5. Simulated VSWR value at 3.5 THz.

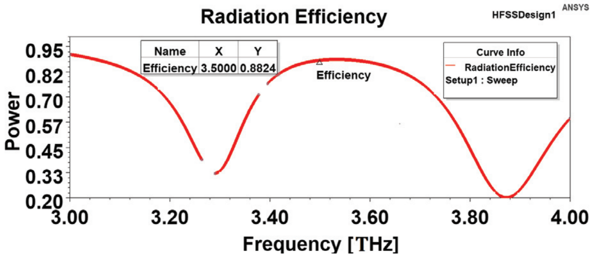

Fig. 6. Simulated efficiency value at 3.5 THz.

received from an isotropic antenna is used. Most of the power present at the radiator input will be emitted by a high-efficiency radiator. On the other hand, low efficiency causes the majority of the power to be lost within the radiator or reflected due to a mismatched device. The HFSS simulator was used in this study to simulate the proposed THz MPA at a frequency of 3.5 THz. Figure 6 depicts how the simulation results demonstrated that the suggested MPA was successfully radiated in the resonance frequency of 3.5 THz and attained an efficiency of 88.24%. From Fig. 7, the proposed MPA's impedance is 1.0-0.01 Ω. When compared to current antenna systems, this high efficiency at 3.5 THz performs well [12–14, 30, 35].

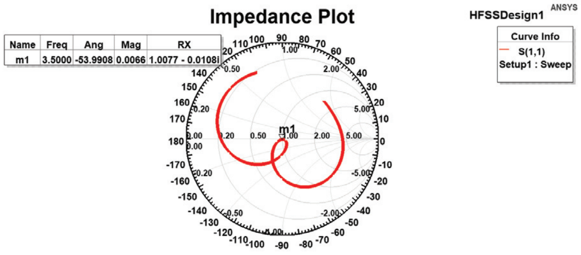

Fig. 7. Impedance plot at 3.5 THz.

IV. COMPARISON

This section aims to evaluate and contrast the electrical characteristics of the proposed THz MPA with other high-performance MPAs that have been reported in the literature. Recently, microstrip patch antennas have gained significant attention for their compact size, planar design, and low-cost fabrication, especially for operating at mmW and THz frequencies [12, 13]. In [14], a small-sized MPA for THz applications has been presented. Designing multiband THz antennas has become a new research area, and [30] proposes a dual-band MPA for surveillance systems. [31] suggests a strategy to improve manufacturing tolerance at millimetre and terahertz frequencies by increasing the size of microstrip patches. [34, 35] discusses two innovative ways of feeding microstrip patches and MPA arrays. The electrical characteristics of these MPAs, along with their uses and core values, are summarized in Table 2. The electrical properties of these structures are compared to those of the proposed antenna [38–42].

Table 2: Comparative result analysis

Ref No	Antenna Structure	Dimensions (mm)	Applications	Frequency (THz)	VSWR	S11 (dB)	Efficiency (%)	Substrate
[12]	Multi	1130 × 1130 × 610	THz comm.	3	1.56	-27	-	-
[13]	Multi Array	2550 × 1217 × 18	THz comm.	3	-	-23	-	InP
[14]	Multi	2000 × 2000 × 100	THz comm.	3	1.87	<-10	-	quartz
[30]	Dual Patch	NA	sub-THz radiation detector	1	-	-17	93.76	RT-Duroid
[34]	Novel Feed Microstrip	NA	NA	3	1.89	-18	-	RT-Duroid 5880
[35]	Patch Array Feed Source	NA	THz comm.	3	1.73	-20	-	PDMS
Proposed	Microstrip Feed	1800 × 1800 × 36	high-speed comm.	3.5	1.013	-43.6	88.24	FR4

V. CONCLUSION

The study unveiled a novel, incredibly thin, flexible MPA design that functions at 3.5 THz. The impact of the microstrip patch's symmetrical structures on its electrical performance was investigated by the researchers. The antenna's actual performance was in line with the design analysis's theoretical expectations. The antenna has an exceptionally wide bandwidth for its operational frequency range. Its compact size makes it an attractive option for use in THz applications, especially high-speed communications.

DECLARATIONS

Funding

The authors did not receive any financial support.

Conflicts of interest / competing interests

The authors declare that they have no conflicts of interest or competing interests that could have influenced the conduct or reporting of this research.

Availability of data and material

The datasets and materials used in this study are available upon request to the corresponding author.

Code availability

The custom codes and software applications developed for this research are available upon request to the corresponding author.

Authors' Contributions

[A.B]: Conceptualization, methodology, and data curation. Designed the study, collected and analyzed the data, and contributed to the interpretation of the results.

[C]: Writing. Original draft preparation and formal analysis. Drafted the initial version of the manuscript and performed statistical analyses.

[D]: Investigation and visualization. Conducted experiments, created figures, and visualized the data.

[E]: Writing. Revision and editing. Revised the manuscript for important intellectual content, grammar, and formatting.

All authors reviewed the manuscript.

REFERENCES

[1] P. H. Siegel, "THz instruments for space," *IEEE Transactions on Antennas and Propagation*, vol. 55, no. 11, pp. 2957-2965, [Available]: https://doi.org/10.1109/TAP.2007.908557, 2007.

[2] P. H. Siegel, "Terahertz technology in biology and medicine," *IEEE transactions on microwave theory and techniques*, vol. 52, no. 10, pp. 2438-2447, [Available]: https://doi.org/10.1109/TMTT.2004.835916, 2004.

[3] J. Zhang, X. Ge, Q. Li, M. Guizani, and Y. Zhan, "5G millimeter-wave antenna array: Design and challenges," *IEEE Wireless Communications*, vol. 24, no. 2, pp. 106-112, [Available]: https://doi.org/10.1109/MWC.2016.1400374RP, 2016.

[4] H. J. Song and T. Nagatsuma, "Present and future of terahertz communications," *IEEE Transactions on Terahertz Science and Technology*, vol. 1, no. 1, pp. 256-263, [Available]: https://doi.org/10.1109/TTHZ.2011.2159552, 2011.

[5] T. Nagatsuma, "Advances in terahertz communications accelerated by photonics technologies," *2019 24th OptoElectronics and Communications Conference (OECC) and 2019 International Conference on Photonics in Switching and Computing (PSC),* pp. 1-3, [Available]: https://doi.org/10.23919/PS.2019.8818026, July 2019.

[6] K. Guan, G. Li, T. Kürner, A. F. Molisch, B. Peng, R. He, and A. Zhong, "On millimeter wave and THz mobile radio channel for smart rail mobility," *IEEE Transactions on Vehicular Technology*, vol. 66, no. 7, pp. 5658-5674, [Available]: https://doi.org/10.1109/TVT.2016.2624504, 2016.

[7] G. Chen, J. Pei, F. Yang, X. Y. Zhou, Z. L. Sun, and T. J. Cui, "Terahertz-wave imaging system based on backward wave oscillator," *IEEE Transactions on Terahertz Science and Technology*, vol. 2, no. 5, pp. 504-512, [Available]: https://doi.org/10.1109/TTHZ.2012.2210282, 2012.

[8] H. Tabata, "Application of terahertz wave technology in the biomedical field," *IEEE Transactions on Terahertz Science and Technology*, vol. 5, no. 6, pp. 1146-1153, 2015.

[9] N. V. Petrov, M. S. Kulya, A. N. Tsypkin, V. G. Bespalov, and A. Gorodetsky, "Application of terahertz pulse time-domain holography for phase imaging," *IEEE Transactions on Terahertz Science and Technology*, vol. 6, no. 3, pp. 464-472, [Available]: https://doi.org/10.1109/TTHZ.2016.2530938, 2016.

[10] J. Grade, P. Haydon, and D. van der Weide, "Electronic terahertz antennas and probes for spectroscopic detection and diagnostics," *Proceedings of the IEEE*, vol. 95, no. 8, pp. 1583-1591, [Available]: https://doi.org/10.1109/JPROC.2007.898900, 2007.

[11] W. Choe and J. Jeong, "Broadband THz CMOS on-chip antenna using stacked resonators," *2017 IEEE International Symposium on Radio-Frequency Integration Technology (RFIT),* pp. 208-210, [Available]: https://doi.org/10.1109/RFIT.2017.8048251, Aug. 2017.

[12] M. Jenning and D. Plettemeier, "Multilayer and multidirectional linearly-tapered slot antenna for

300 GHz applications," *Proceedings of the Fourth European Conference on Antennas and Propagation,* pp. 1-5, April 2010.

[13] H. Kanaya, T. Oda, N. Iizasa, and K. Kato, "300 GHz one-sided directional slot array antenna on indium phosphide substrate," *2015 International Symposium on Antennas and Propagation (ISAP),* pp. 1-2, Nov. 2015.

[14] A. Dyck, M. Rösch, A. Tessmann, A. Leuther, M. Kuri, H. Maßler, and O. A. Ambacher, "300 GHz microstrip multilayered antenna on quartz substrate," *2018 International Workshop on Antenna Technology (iWAT),* pp. 1-3, [Available]: https://doi.org/10.1109/IWAT.2018.8379183, Mar. 2018.

[15] H. J. Song and T. Nagatsuma, "Present and future of terahertz communications," *IEEE transactions on terahertz science and technology*, vol. 1, no. 1, pp. 256-263, [Available]: https://doi.org/10.1109/TTHZ.2011.2159552, 2011.

[16] K. C. Huang and Z. Wang, "Terahertz terabit wireless communication," *IEEE Microwave Magazine*, vol. 12, no. 4, pp. 108-116, [Available]: https://doi.org/10.1109/MMM.2011.940596, 2011.

[17] T. Nagatsuma, H. J. Song, and Y. Kado, "Challenges for ultrahigh speed wireless communications using terahertz waves," *Terahertz Science and Technology*, vol. 3, no. 2, pp. 55-65, [Available]: https://doi.org/10.11906/TST.055-065.2010.06.05, 2010.

[18] P. H. Siegel, P. de Maagt, and A. I. Zaghloul, "Antennas for terahertz applications," *2006 IEEE Antennas and Propagation Society International Symposium,* pp. 2383-2386, [Available]: https://doi.org/10.1109/APS,2006.1711074, July 2006.

[19] J. Federici and L. Moeller, "Review of terahertz and subterahertz wireless communications," *Journal of Applied Physics*, vol. 107, no. 11, [Available]: https://doi.org/10.1063/1.3386413, 2010.

[20] T. Kleine-Ostmann and T. Nagatsuma, "A review on terahertz communications research," *Journal of Infrared, Millimeter, and Terahertz Waves*, vol.32, pp. 143-171, [Available]: https://doi.org/10.1007/s10762-010-9758-1, 2011.

[21] X. Yu, T. Ohira, J. Y. Kim, M. Fujita, and T. Nagatsuma, "Waveguide-input resonant tunnelling diode mixer for THz communications," *Electronics Letters*, vol. 56, no. 7, pp. 342-344, [Available]: https://doi.org/10.1049/el.2019.3682, 2020.

[22] J. D. Kraus and R. J. Marhefka, *Antennas: For all Applications*, third edition, Beijing, China, 2017.

[23] Y. Lo, D. Solomon, and W. Richards, "Theory and experiment on microstrip antennas," *IEEE Transactions on Antennas and Propagation*, vol. 27, no. 2, pp. 137-145, [Available]: https://doi.org/10.1109/TAP.1979.1142057, 1979.

[24] T. Kosako, Y. Kadoya, and H. F. Hofmann, "Directional control of light by a nano-optical Yagi–Uda antenna," *Nature Photonics*, vol. 4, no. 5, pp. 312-315, [Available]: https://doi.org/10.1038/nphoton.2010.34, 2010.

[25] Constantine A. Balanis, *Antenna Theory Analysis and Design*, 3rd edition, Wiley India, 2005.

[26] John D Kraus, *Antennas*, 2nd edition, Tata McGraw Hill Company Limited, 1997.

[27] Pramod Dhande, "Antenna and its Applications," *DRDO Science Spectrum*, March 2009.

[28] M. He and X. Xu, "Closed-form solutions for analysis of cylindrically conformal microstrip antennas with arbitrary radii," *IEEE Transactions on Antennas and Propagation*, vol. 53, no. 1, pp. 518-525, [Available]: https://doi.org/10.1109/TAP.2004.838772, 2005.

[29] S. S. Kashyap and V. Dwivedi, "Compact microstrip patch antennas for terahertz applications," *2015 9th Asia Modelling Symposium (AMS),* pp. 157-163, [Available]: https://doi.org/10.1109/AMS.2015.33, Sept. 2015.

[30] M. S. Rabbani and H. Ghafouri-Shiraz, "Improvement of microstrip antenna's bandwidth and fabrication tolerance at terahertz frequency bands," IET, [Available]: https://doi.org/10.1049/ic.2015.0146, 2015.

[31] P. Kopyt, B. Salski, P. Zagrajek, D. Obrębski, and J. Marczewski, "Modeling of silicon-based substrates of patch antennas operating in the sub-THz range," *IEEE Transactions on Terahertz Science and Technology*, vol. 7, no. 4, pp. 424-432, [Available]: https://doi.org/10.1109/TTHZ.2017.2706026, 2017.

[32] R. Bhatoa and E. Sidhu, "Novel terahertz microstrip patch antenna design for detection of biotin applications," *2017 International Conference on Big Data Analytics and Computational Intelligence (ICBDAC),* pp. 289-292, [Available]: https://doi.org/10.1109/ICBDACI.2017.8070850, Mar. 2017.

[33] K. R. Jha and G. Singh, "Dual-band rectangular microstrip patch antenna at terahertz frequency for surveillance system," *Journal of Computational Electronics*, vol. 9, pp. 31-41, [Available]: https://doi.org/10.1007/s10825-009-0297-8, 2010.

[34] M. S. Rabbani and H. Ghafouri-Shiraz, "Size improvement of rectangular microstrip patch antenna at MM-wave and terahertz frequencies," *Microwave and Optical Technology Letters*, vol. 57, no. 11, pp. 2585-2589, [Available]: https://doi.org/10.1002/mop.29400, 2015.

[35] K. R. Jha and S. K. Sharma, "Waveguide integrated Microstrip patch antenna at THz frequency," *2014 IEEE Antennas and Propagation*

Society International Symposium (APSURSI), pp. 1851-1852, [Available]: https://doi.org/10.1109/APS.2014.6905252, July 2014.

[36] K. R. Jha and S. K. Sharma, "Waveguide integrated microstrip patch array feed source for a reflector antenna at THz frequency," *2014 IEEE Antennas and Propagation Society International Symposium (APSURSI),* pp. 1465-1466, [Available]: https://doi.org/10.1109/APS.2014.6905058, July 2014.

[37] C. A. Balanis, *Modern Antenna Handbook*, John Wiley & Sons, 2011.

[38] D. M. Pozar, *Microwave Engineering*, John Wiley & Sons, 2009.

[39] R. Vallikannu, M. Vinoth, V. Koushick, and E. M. Ali, "A miniaturized defected ground patch antenna for ITS 5G-V2x-C applications," *2022 International Conference on Computer Communication and Informatics (ICCCI),* pp. 1-6, [Available]: https://doi.org/10.1109/ICCCI54379.2022.9741033, Jan. 2022.

[40] C. Divya and V. Koushick, "Design and implementation of slotted metamaterial stacked microstrip patch antenna for broadband applications," *Journal of Physics: Conference Series*, IOP Publishing, vol. 1432, no. 1, p. 012067, [Available]: https://doi.org/10.1088/1742-6596/1432/1/012067, 2020.

[41] V. Koushick, C. Divya, and G. Lakshmi, "L/C/X triple band compact dipole array antenna for RADAR application," *Journal of Physics: Conference Series,* IOP Publishing, vol. 1432, no. 1, p. 012082, [Available]: https://doi.org/10.1088/1742-6596/1432/1/012082, 2020.

[42] M. Kavitha, T. D. Kumar, A. Gayathri, and V. Koushick, "28GHz printed antenna for 5G communication with improved gain using array," *International Journal of Scientific and Technology Research*, vol. 9, no. 3, pp. 5127-5133, 2020.

V. Koushick received his B.E degree (ECE) from Anna University Tiruchirappalli in 2011. He received his Post graduate Diploma in VLSI design from Annamalai University Chidambaram in 2011. He received his M.E. degree (communication systems) from Anna University Chennai in 2014. He received his Ph.D., degree (communication systems - information technology (interdisciplinary)) in the field of RF & microwave antennas from Manonmaniam Sundaranar University, Tirunelveli, in 2022. From 2011 to 2012 he worked as lecturer and from 2014 to till date he is working as assistant professor in electronics and communication engineering. Currently, he is working as assistant professor in the Department of Electronics and Communication Engineering at Vel Tech Rangarajan Dr. Sagunthala R&D Institute of Science and Technology, Avadi, Chennai. He published 12 papers in international journals, indexed by UGC CARE List, Scopus, Web of Science, and 9 papers in international conferences organized by IEEE. He received best presenter award from University of Perlis, Malaysia, and best paper award from Ramco Institute of Technology, Virudhunagar, Tamilnadu, sponsored by AICTE, New Delhi. He published 4 Indian patents and 1 German patent. He published 3 book chapter articles and submitted 2 book chapters in Taylor and Francis. He serving as member educationist in Sigma CBSE School, Tiruchirappalli. He is a member in IAENG, IRED, BES, HKCBEES, and INSTICC professional bodies. He is an active reviewer in ACES, IEEE conferences, and reputed journals. His research areas include antennas, RF and microwaves, RADAR and VLSI.

C. Divya received her B.E degree from Anna University Chennai in 2008. She received her M.E. degree from Anna University Chennai in 2010. She received her Ph.D., degree from Manonmaniam Sundaranar University, Tirunelveli, in 2014. From 2010 to date she is an assistant professor in Centre for Information Technology and Engineering, Manonmaniam Sundaranar University, Tirunelveli. She published 14 papers in international journals and 7 papers in international conferences. She published book and chapters in sensor networks and cyber security. She received merit scholarship award from SSN College of Engineering, Chennai. She organized many workshops and seminars funded by UGC. She is an eminent editorial board member and reviewer in various international journals, like RJIOT, JSTEI and IACSIT. She published 2 Indian patents and 1 book chapter. She is an associate member in many professional bodies, like IAENG and UACEE. Her research areas include wireless sensor networks, communication networks, nano devices and low power VLSI.

M. Vinoth received his B.E degree (ECE) from Anna University Tiruchirappalli in 2011. He received his M.E. degree (Communication Systems) from Anna University Chennai in 2015. He received his Ph.D., degree in the field of RF & Microwave Antennas from Hindustan Institute of Technology and Science in 2022. Currently, he is working as Assistant Professor in the Department of Electronics and Communication Engineering at K. Ramakrishnan College of Engineering (Autonomous), Tiruchirappalli. He published 10+ papers in International Journals which is indexed by SCIE, Scopus, Web of Science and 10+ papers in international conference organized by IEEE. He received best paper award from Ramco Institute of Technology, Virudhunagar, Tamilnadu sponsored by AICTE, New Delhi. He published 1 German patent. He has 10 Years of Industrial experience and 3 Years of Teaching experience. His research areas include Antennas, RF and Microwaves, MIMO, 5G Bands Networks etc.,

E.A. Mohamed obtained his Bachelor degree in Electrical and Electonics Engineering from the Manonmaniam Sundaranar University (India), Tirunelveli in 2000. He then pursued a Master degree in Applied Electronics in 2001 from Madurai Kamaraj University and a Ph.D. from Anna University, Chennai. Currently, he holds the position of Associate Professor in the Department of ECE at JP College of Engineering, Tenkasi. His research interests include Systme Engineering, Image and Signal Processing, RF and Wireless Communications, and he is a member of the ISTE, IETE and IAENG. He has authored more than 50 research publications in international journals and conferences.

M. Sugadev received his Bachelor degree in Electronics and Communication Engineering from Institution of Engineers (India), Kolkatta in 2005, Master Degree in VLSI Design in 2008 and Ph.D. from Sathyabama Institute of Science and Technology, Chennai. He is working as Associate Professor in Department of ECE, at Sathyabama Institute of Science and Technology, Chennai. His areas of research include RF and Wireless Communications. He is a member of Institution of Engineers (India) and IETE. He has more than 50 Research publications in International Journals and Conferences.

Balanced Filtering Power Divider based on Odd-mode Hybrid Microstrip and Slotline Spoof Surface Plasmon Polaritons

Yi Song and Anxue Zhang

School of Information and Communications Engineering
Xi'an Jiaotong University, Xi'an 710049, China
yi_song17@hotmail.com, anxuezhang@mail.xjtu.edu.cn

Abstract – In this paper, an ultra-wideband balanced filtering power divider (B-FPD) with high common mode (CM) suppression level is proposed. The B-FPD is designed based on the odd mode spoof surface plasmon polaritons (SSPPs), which are constructed by the hybrid folded microstrip and slotline (HFMS) structure. Firstly, the dispersion characteristic and electric field distribution of the HFMS SSPP unit cell are investigated, which can decrease the upper cut-off frequency for size reduction of nearly 50%. Next, an equal balanced power divider with low cut-off frequency is proposed based on the microstrip-to-slotline transition structure and slotline Y-junction. Then, the balanced power divider is used to excite the odd mode of HFMS SSPP structure. An equal B-FPD with center frequency of 4.0 GHz is implemented, and the 3-dB bandwidth covers 0.9 to 7.0 GHz. Finally, the B-FPD with advantages of high CM suppression level and compact size is fabricated and measured.

Index Terms – balanced filtering power divider, common mode suppression, spoof surface plasmon polariton.

I. INTRODUCTION

With the developments of modern mobile communication, radio frequency (RF) communication systems have attracted extensive attention. Hence, researchers have paid much efforts in implementing excellent RF devices, such as antennas, power dividers, bandpass filters, and phase shifters. Power dividers and filtering power dividers, as the crucial components of RF circuit system, can realize functions of power distribution and frequency selection, respectively [1–5].

Spoof surface plasmon polariton (SSPP) structure can support the surface wave alike surface plasmon polaritons (SPPs) at microwave frequency, and the SSPPs show the similar characteristics of electromagnetic field confinement, upper cut-off frequency with the SPP at optical frequency band [6, 7]. Hence, in recent years, the SSPP transmission lines have been widely adopted for designing microwave filters [8, 9], diplexers [10], phase shifters [11, 12], antennas [13], splitters [14–17], etc.

In particular, some well-designed power dividers are reported based on SSPP structure fed by the coplanar waveguide (CPW) [14–16], and double-sided parallel spoof surface plasmon polariton transmission line (DSP-SSPP-TL) [17]. In [15], a four-way SSPP splitter is designed by the SSPP transmission line. The transition structure constructed by the long axis of a half oval ring is used to match the wave vector between the CPW mode and the SSPP mode. Furthermore, a beam splitter with multi-band rejection is implemented based on SSPP structure with T-shaped decoration [16]. In addition, the DSP-SSPP-TL is also adopted for designing balanced dividers with ultra-wideband isolation by loading the lumped resistors [17].

Recently, the multifunctional integrated devices, such as filtering power dividers (FPDs) have been widely reported, which can not only achieve power distribution and frequency selection functions simultaneously but also avoid the additional power loss and size increase caused by the devices cascade [18–23]. Hence, several FPDs are proposed based on SSPP structure fed by CPW [18], slotline SSPP unit cells [19, 20], and hybrid SSPP and substrate integrated waveguide (SIW) structures [21–23]. In [19], an ultra-wideband FPD is designed based on the quasi Y-junction slotline SSPP transmission line constructed by the corrugated grooves. The odd SSPP mode is excited by the microstrip-to-slotline convertor. Besides, the compact FPD implemented by the hybrid SSPP and SIW achieves independent control of the upper and lower stopbands [23].

Balanced microwave components, such as balanced filters [24] and balanced filtering dividers [25] base on the microstrip resonator, have drawn extensive attention due to the excellent advantages of common mode (CM) noise rejection. It is essential to achieve compact size, good filtering function, and high CM suppression level.

In this paper, a hybrid folded microstrip and slotline (HFMS) SSPP unit cell is proposed, whose fundamental mode is odd mode. The dispersion curves show that the HFMS unit cell can lower the upper cutoff frequency for size miniaturization of nearly 50%. And a highpass balanced power divider is designed

Submitted On: June 23, 2023
Accepted On: September 8, 2023

https://doi.org/10.13052/2023.ACES.J.380709

1054-4887 © ACES

by microstrip-to-slotline transition feeding structure and slotline Y-junction. Then, the balanced power divider is adopted to excite the odd mode of the HFMS SSPP structure. Finally, an equal balanced FPD with high CM suppression level is implemented by the Rogers 5880 substrate with the relative dielectric constant of 2.2, thickness of 0.5 mm, and loss tangent of 0.0009. And the in-band minimum insertion loss is 1.5 dB.

II. CHARACTERISTIC OF THE SSPP UNIT

Figure 1 shows configurations of three types of SSPP unit cells. In Fig. 1 (a), the traditional slotline SSPP unit cell is presented. The orange metal and white strips represent the ground plane at bottom layer and slotline, respectively. Figure 1 (b) shows the hybrid microstrip and slotline (HMS) SSPP unit cell, and the yellow strip represent the metal microstrip on the top layer. To further reduce the physical dimension, the top metal microstrip is folded and the HFMS SSPP unit cell is shown in Fig. 1 (c).

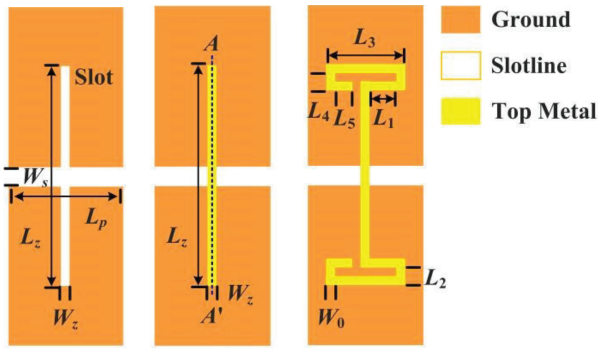

(a) (b) (c)

Fig. 1. Configuration of the SSPP unit cells: (a) Type A: traditional slotline, (b) Type B: Hybrid microstrip and slotline, and (c) Type C: Hybrid folded microstrip and slotline.

The comparisons of simulated dispersion curves of the fundamental mode of three types of SSPP unit cells are shown in Fig. 2. The physical dimensions of SSPP unit cells are as follows: W_z = 0.3, W_0 = 0.3, W_s = 0.8, L_z = 7, L_p = 3.8, L_1 = 0.9, L_2 = 0.6, L_3 = 2.7, L_4 = 0.6, L_5 = 0.6 (unit: mm). The upper cut-off frequencies of traditional slotline SSPP unit cell and HMS SSPP unit cell are 15.7 GHz and 12.9 GHz, respectively. Furthermore, the upper cut-off frequency can be further reduced to 7.8 GHz by the HFMS SSPP unit cell. Hence, a size reduction of nearly 50.0% can be achieved.

The upper cut-off frequency of the HFMS SSPP unit cell can be adjusted by the physical dimensions. The effects of parameters L_T, W_z, and W_s are investigated, and four groups of physical dimensions are listed in Table 1, where $L_T = L_1 + L_2 + L_3 + L_4 + L_5$. Figure 3 shows the simulated dispersion curves with different dimensions. It can be concluded from Fig. 3 that (1) the upper cut-off frequency can be reduced by increasing the length L_T of microstrip transmission line; (2) the upper cut-off frequency can be reduced by decreasing the width W_z of the microstrip; and (3) the increase of width W_s of the slotline can allow upper cut-off frequency shift slightly toward lower frequency. Hence, the upper cut-off frequency can be easily designed.

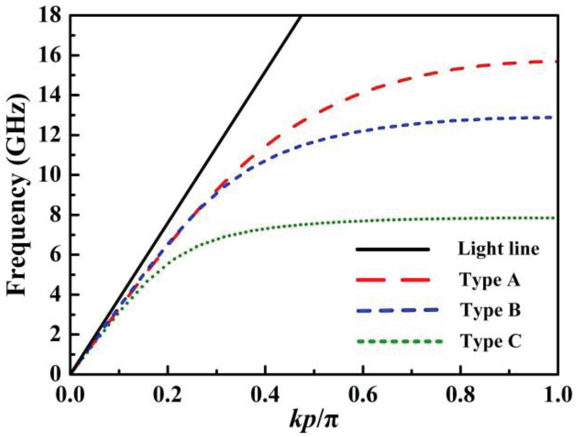

Fig. 2. Simulated dispersion curves of the fundamental mode of three types of SSPP unit cells.

Table 1: Dimensions of HFMS SSPP cells (unit: mm)

Combination	L_T	W_z	W_s	L_p	L_z	W_0
I	**4.0**	**0.3**	0.8	3.8	7.2	0.3
II	5.4	**0.5**	0.8	3.8	7.2	0.3
III	**5.4**	**0.3**	**0.8**	3.8	7.2	0.3
IV	5.4	0.3	**1.0**	3.8	7.2	0.3

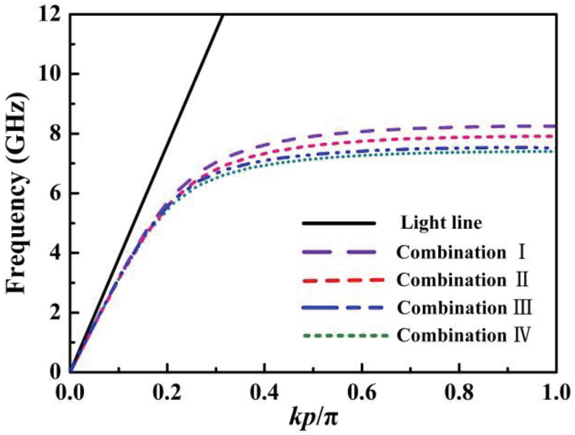

Fig. 3. Comparison of simulated dispersion curves of the HFMS SSPP unit cell with different dimensions.

The differential mode (DM) filtering function can be achieved by the odd mode of the SSPP transmission line. Hence, the electric field distribution of the fundamental mode of HFMS SSPP unit cell is investigated, and its cross-section view is shown in Fig. 4. It can be observed that the electric fields on two sides of the slotline are out-of-phase. Hence, the odd fundamental mode can be used to achieve a DM filtering function with upper cut-off frequency. In particular, the symmetric plane AA' is equivalent to an electric wall, and electric field distribution within the slotline is in phase.

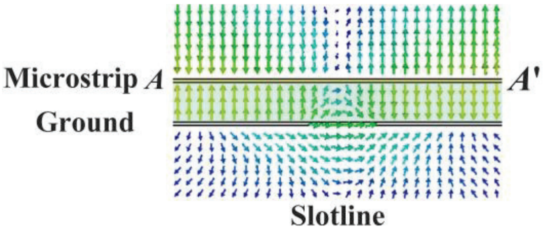

Fig. 4. Cross-section view (AA') of the simulated electric field distribution of the fundamental mode of the HFMS SSPP unit cell.

III. SLOTLINE BALANCED POWER DIVIDER

In this section, a slotline balanced highpass filter is designed based on microstrip-to-slotline transition feeding structure and slotline transmission line. Then, a slotline balanced power divider with highpass characteristic is designed by using the slotline Y-junction, which can separate the common input port into two output ports.

Figure 5 shows the configuration of the slotline balanced highpass filter. The microstrip-to-slotline transition feeding structure is adopted for exciting the slotline stepped impedance transmission line. The corner cut is introduced to reduce the impedance discontinuity and signal reflection. The slotline stepped impedance structure can increase the freedom in adjusting the matching and without affecting the upper cut-off frequency of the SSPP unit cell. The matching of the feeding structure can be controlled by adjusting the length $L_{in/out}$ of slotline, width $W_{in/out}$ of slotline, distance $d_{kin/out}$ between feeding line and circular slotline, and the radius R_s of the circular slotline. Since a balanced FPD with three gradient HFMS SSPP unit cells and three identical SSPP unit cells will be designed in the next section, the lengths of slotline L_{1p}, L_{2p}, and L_{3p} are all set as $3 \times L_p$ mm.

Figure 6 shows a cross-section view of electric field distributions of the feeding structure under DM and CM excitation. As shown in Fig. 6 (a), the electric field distribution under DM excitation is identical to that of the fundamental mode. Hence, the odd mode of the SSPP unit cell can be excited. Under CM excitation, the symmetric plane BB′ corresponds to a magnetic wall. The electric field distribution within the slotline is out of phase, as shown in Fig. 6 (b). Hence, the CM signals will cancel out and the feeding structure exhibits intrinsic CM suppression ability [24].

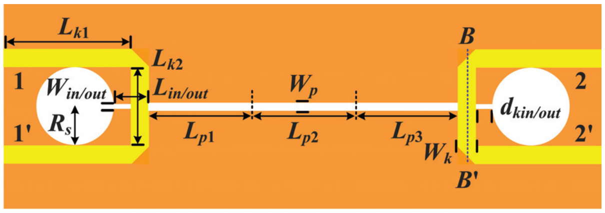

Fig. 5. Configuration of the slotline balanced highpass filter. (All dimensions are in mm: L_{k1} = 23.5, L_{k2} = 14, $L_{in/out}$ = 3, L = 34.8, W_k = 1.5, $W_{in/out}$ = 0.6, W_p = 0.8, R_s = 7, $d_{kin/out}$ = 1.5).

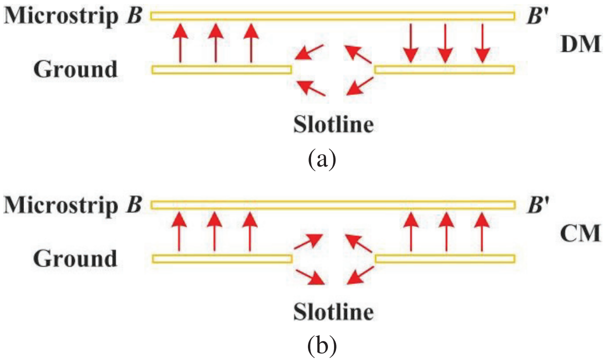

Fig. 6. Cross-section view (BB') of electric field distribution of the transition feeding structure. (a) DM excitation; (b) CM excitation.

Figure 7 presents the simulated transmission and reflection characteristics of the slotline balanced filter.

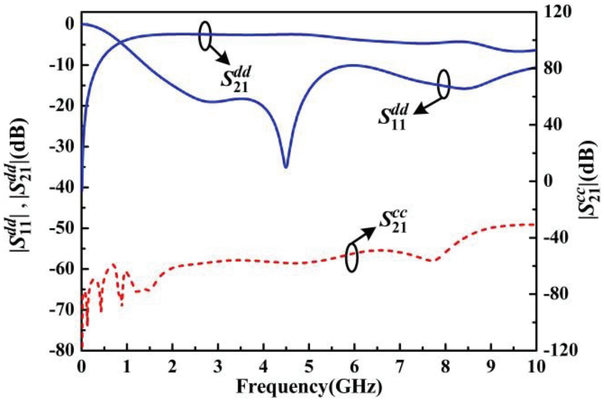

Fig. 7. Simulated results of transmission and reflection characteristics of the slotline balanced highpass filter.

Under DM excitation, a highpass filtering function with low cut-off frequency of 1.0 GHz is achieved duo to the microstrip-to-slotline feeding structure with a highpass characteristic. And the in-band return loss is above 11.5 dB within 7.0 GHz. The in-band minimum insertion loss is 2.5 dB, and the relatively large insertion loss is caused by the radiation loss of the slotline structure. In addition, the low cut-off frequency of the balanced highpass filter can be adjusted by the radius R_s, and it will move toward lower frequency as the value of R_s increases. Under CM excitation, the in-band CM suppression level is above 50.0 dB, the 40.0 dB CM suppression level can be up to 12.0 GHz.

Based on the slotline balanced filter, an equal balanced power divider with low cut-off frequency is implemented, as shown in Fig. 8. The slotline Y-junction is adopted to replace the slotline transmission line L_{p2}. The horizontal length of the slotline Y-junction is equal to L_{p2}. The signals from input port 1/1' will be allocated to ports 2/2′ and 3/3′ with equal power ratio. And the matching between input port 1/1′ and 2/2′, 3/3′ can be adjusted by parameters H_0 and H. The final physical dimensions of balanced power divider are listed in the annotation of Fig. 8.

Figure 9 shows the DM and CM simulated transmission and reflection characteristics of the balanced divider. Under DM excitation, a balanced power divider with low cut-off frequency of 1.5 GHz is achieved. The in-band minimum insertion loss of the balanced power divider is 2.36 dB, with 3-dB power division loss excluded. And the return loss is above 11.2 dB within 7.0 GHz. Under CM excitation, the CM suppression level is above 44.0 dB.

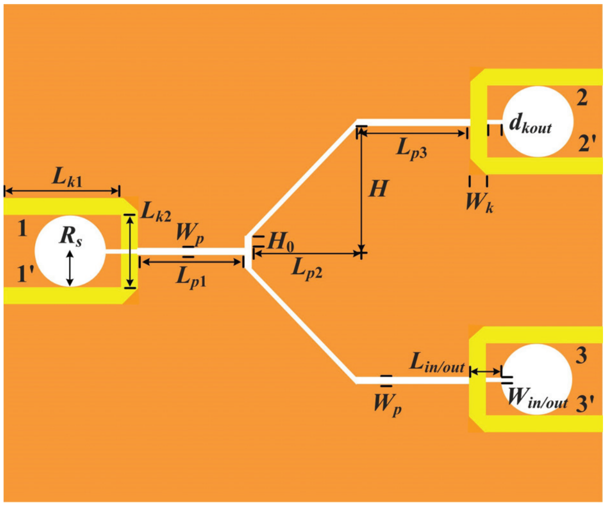

Fig. 8. Configuration of the slotline balanced highpass divider. (All dimensions are in mm: L_{k1} = 23.5, L_{k2} = 14.0, $L_{in/out}$ = 3.0, L_{p1} = L_{p2} = L_{p3} = 11.4, W_k = 1.5, $W_{in/out}$ = 0.6, W_p = 0.8, R_s = 7.0, $d_{kin/out}$ = 1.5, H_0 = 0.8, H = 13.5).

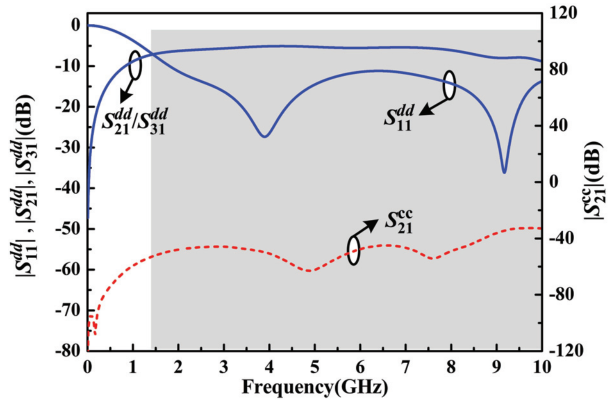

Fig. 9. Simulated results of the slotline balanced highpass divider.

IV. BALANCED FILTERING DIVIDER BASED ON SSPP

On this basis, the balanced filtering power divider (FPD) is implemented, as shown in Fig. 10. Part I is the feeding structure constructed by microstrip-to-slotline transition structure. Part II is momentum matching conversion structure constructed by three gradient HFMS SSPP unit cells, which can match the wave vector between TE mode and SSPP mode. The TE mode transmitted from the feeding structure will be converted to SSPP mode. The matching can be adjusted by the length difference between adjacent SSPP unit cells. Part III is a SSPP transmission line, which consists of three identical HFMS unit cells. The SSPP transmission line can

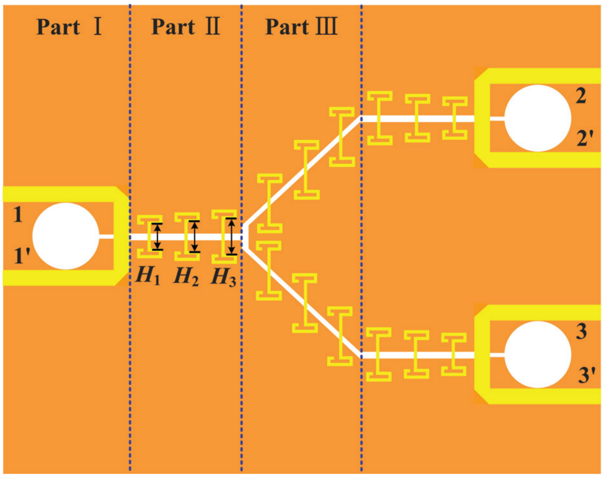

Fig. 10. Configuration of the SSPP-based balanced filtering divider. (All dimensions are in mm: H_1 = 3.4, H_2 = 4.2, H_3 = 5.0).

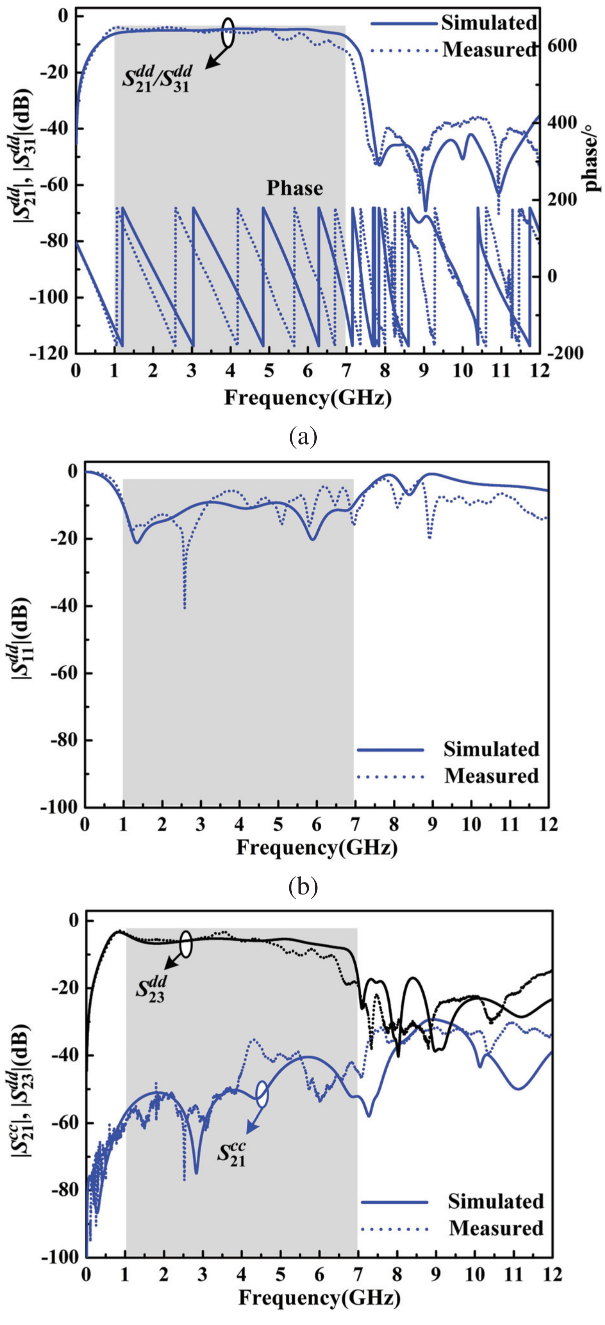

(a)

(b)

(c)

Fig. 11. Transmission and reflection characteristics of the balanced filtering divider: (a) S_{dd21}/S_{dd31}/phase, (b) S_{dd11}, (c) S_{cc21}/S_{dd23}.

support the transmission of SSPP waves and provide the upper cut-off frequency for achieving filtering function.

Figure 11 presents the simulated results of the balanced FPD under DM and CM excitation. Under DM excitation, a balanced FPD with center frequency of 4.0 GHz and 3-dB fractional bandwidth of 152.0% is achieved. The in-band insertion loss is 1.7 dB, with 3 dB power division loss excluded, and the in-band return loss is above 9.2 dB. Benefiting from the field confinement ability of the SSPP structure, the insertion loss is reduced by nearly 0.7 dB. The isolation between two output ports is above 6 dB, which is poor due to the lack of an isolation resistor. Under CM excitation, the in-band CM suppression is above 40.0 dB.

Figure 12 presents the electric field distributions of the balanced FPD under DM and CM operation. Under DM excitation, it can be observed from Fig. 12 (a) that the DM signals can transfer from input port 1/1′ to output ports 2/2′ and 3/3′ within the passband, for example at 1.5 GHz. On the contrary, the DM signals out of the passband cannot transmit to the output ports, as shown in Fig. 12 (b). Under CM excitation, the CM signals are rejected by microstrip-to-slotline transition feeding structure, as shown in Fig. 12 (c).

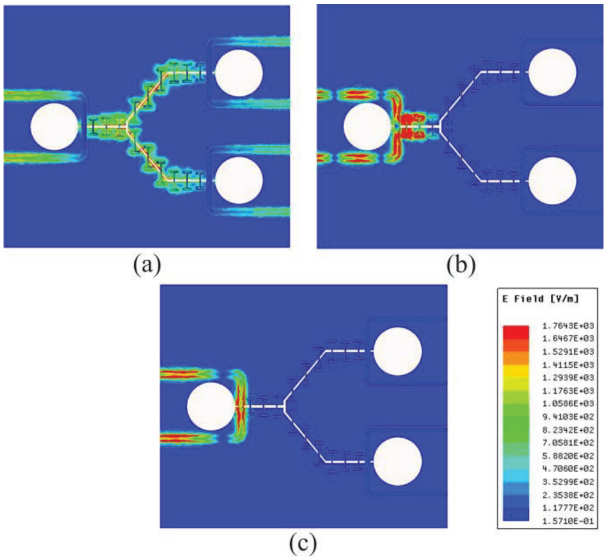

Fig. 12. Simulated E-field distribution of the balanced filtering divider at (a) 1.5 GHz, (b) 8.0 GHz under DM excitation, and (c) 4.0 GHz under CM excitation.

V. IMPLEMENTATION AND MEASUREMENT

In order to verify the methodology, the balanced FPD is fabricated on the Rogers 5880 substrate. The photographs of top and bottom view of the fabricated B-FPD are shown in Fig. 13. The total circuit size is 80.0 mm × 70.0 mm × 0.5 mm, which amounts to $1.45\lambda_g \times 1.27\lambda_g \times 0.006\lambda_g$, where λ_g is the guided wavelength at the center frequency of 4.0 GHz.

The fabricated balanced B-FPD is measured by a four-port vector network analyzer, and the measured results are shown in Fig. 11. Under the DM operation, the

Table 2: Comparisons with previous SSPP-based filtering dividers

Ref.	**Circuit Size (λ_g^2)**	**f_0 (GHz)**	**FBW (%)**	**IL (dB)**	**Structure Type**	**Operation**	**CMRR/dB**
[18]	/	5.3	105.0%	1.8	CPW	Single-ended	No
[20]	0.22	3.6	99.0%	1.4	Slot	Single-ended	No
[22]	/	6.0	66.0%	1.0	SIW	Single-ended	No
[23]	1.5 × 0.67	10.0	40.0%	0.8	SIW	Single-ended	No
This work	1.45 × 1.27	4.0	152.0%	1.7	Microstrip + Slot	Balanced	50

λ_g: wavelength of the guided wave, f_0: center frequency, FBW_{3dB}: 3-dB fractional bandwidth, IL: insertion loss, CMRR: common mode rejection ratio.

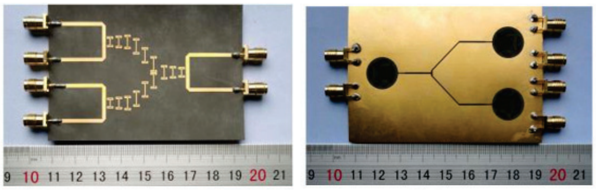

(a) (b)

Fig. 13. Photographs of the (a) top and (b) bottom views of the fabricated balanced filtering divider.

measured minimum insertion loss is 1.6 dB, and in-band return loss is above 5.2 dB. Under the CM operation, the in-band CM suppression level is above 35.0 dB. The differences between measured and simulated results may result from fabrication tolerances, deformations caused by fabrication and test.

Table 2 shows comparisons with the published SSPP-based filtering power divider. The proposed balanced FPD shows the advantages of relatively compact size and good CM suppression level. In addition, the balanced FPD based on SSPP is easier to fabricate.

VI. CONCLUSION

In this paper, an odd-mode SSPP structure constructed by a HFMS structure is investigated. Then, the microstrip-to-slotline transition feeding structure and slotline Y-junction are adopted for designing the balanced power divider, which can achieve controllable low cut-off frequency, equal power distribution ratio, and intrinsic CM suppression ability. Finally, the balanced FPD is designed by adopting the balanced power divider to feed the HFMS SSPP structure. The upper cut-off frequency can be controlled by the physical dimensions of the SSPP unit cell. The balanced FPD shows the advantages of relatively compact size and high CM suppression level.

ACKNOWLEDGMENT

This work was supported in part by the National Key R&D Program of China under Grant 2020YFA0709802, and in part by the "Siyuan Scholar" Fellowship of XJTU.

REFERENCES

[1] G. Dong, B. Zhang, W. Wang, and Y. Liup, "Compact wideband filtering power dividers based on short-circuited stubs," *Applied Computational Electromagnetics Society (ACES) Journal,* vol. 34, pp. 141-147, 2019.

[2] Z. Qiao, Y. Chen, C. Feng, and W. Wang, "Compact multi-mode filtering power divider with high selectivity, improved stopband and in-band isolation," *Applied Computational Electromagnetics Society (ACES) Journal,* vol. 35, pp. 936-940, 2020.

[3] W. J. Shen, Y. Han, W. R. Chen, D. Jiang, S. Luo, and T. M. Bai, "Design of electronically controlled filter power divider based on liquid crystal," *Applied Computational Electromagnetics Society (ACES) Journal,* vol. 37, pp. 93-101, 2022.

[4] S, Roshani, S. I. Yahya, B . M. Alameri, Y. S. Mezaal, L. W. Liu, and S. Roshani, "Filtering power divider design using resonant LC branches for 5G low-band applications," *Sustainability*, vol. 14, Article ID 12291, 2022.

[5] S, Roshani, S. I. Yahya, J. Rastad, Y. S. Mezaal, L. W. Liu, and S. Roshani, "Design of a filtering power divider with simple symmetric structure using stubs," *Symmetry*, vol. 14, Article ID 1973, 2022.

[6] X. Gao, L. Zhou, Z. Liao, H. F. Ma, and T. J. Cui, "An ultra-wideband surface plasmonic filter in microwave frequency," *Appl. Phys. Lett.*, vol. 104, Article ID 191603, 2014.

[7] L. Tian, Z. Zhang, J. Liu, K. Zhou, Y. Gao, and S. Liu, "Compact spoof surface plasmon polaritons waveguide drilled with L-shaped grooves," *Opt. Exp.*, vol. 24, pp. 28693-28703, 2016.

[8] D. F. Guan, P. You , Q. Zhang, K Xiao, and S.-W. Yong, "Hybrid spoof surface plasmon polariton and substrate integrated waveguide transmission line and its application in filter," *IEEE Trans. Microw. Theory Techn.,* vol. 65, pp. 4925-4931, 2017.

[9] Y. Liu and K.-D. Xu, "Bandpass filters using grounded stub-loaded microstrip periodic structure for suppression of modes," *J. Phys. D: Appl. Phys.*, vol. 55, Article ID 425104, 2022.

[10] Y. Cui, K.-D. Xu, Y. Guo, and Q. Chen, "Half-mode substrate integrated plasmonic waveguide for filter and diplexer designs," *J. Phys. D: Appl. Phys.*, vol. 55, Article ID 125104, 2022.

[11] C. Ding, F.-Y. Meng, J.-Q. Han, H.-L. Mu, Q.-Y. Fang, and Q. Wu, "Design of filtering tunable liquid crystal phase shifter based on spoof surface plasmon polaritons in PCB technology," *IEEE Trans. Compon. Packag. Manuf. Technol.*, vol. 9, pp. 2418-2826, 2019.

[12] A. R. Moznebi and K. Afrooz, "Wideband compact phase shifter based on hybrid half-mode substrate integrated waveguide and spoof surface plasmon polariton," *J. Phys. D: Appl. Phys.*, vol. 55, Article ID 155203, 2022.

[13] Q. Li, Y. Yin, X. Chen, and K.-D. Xu, "A frequency-controlled wide-angle scanning antenna based on spoof surface plasmon polariton," *IEEE Photonics Technol. Lett.*, vol. 34, pp. 1300-1303, 2022.

[14] J. Wang, L. Zhao, Z. C. Hao, X. Shen, and T. J. Cui, "Splitting spoof surface plasmon polaritons to different directions with high efficiency in ultra-wideband frequencies," *Opt. Lett.*, vol. 44, pp. 3374-3377, 2019.

[15] S.-Y. Zhou, S.-W. Wong, J.-Y. Lin, L. Zhu, Y. J. He, and Z.-H. Tu, "Four-way spoof surface plasmon polaritons splitter/combiner," *IEEE Microw. Wirel. Compon. Lett.*, vol. 29, pp. 98-100, 2019.

[16] A. Aziz, Y. Fan, P. H. He, H. C. Zhang, I. Ali, W. X. Tang, and T. J. Cui, "Spoof surface plasmon polariton beam splitters integrated with broadband rejection filtering function," *J. Phys. D, Appl. Phys.*, vol. 54, Article ID 335105, 2021.

[17] M. Li, Y. Wu, M. Qu, Q. Li, and Y. Liu, "A novel power divider with ultra-wideband harmonics suppression based on double-sided parallel spoof surface plasmon polaritons transmission line," *Int. J. RF Microw. Comput.-Aided Eng.*, vol. 28, Article ID e21231, 2018.

[18] E. Farokhipour, N. Komjani, and M. A. Chaychizadeh, "An ultra-wideband three-way power divider based on spoof surface plasmon polaritons," *J. Phys. D, Appl. Phys.*, vol. 124, Article ID 235310, 2018.

[19] H.-T. Xu, D.-F. Guan, Z.-B. Yang, Q. Zhang, L. Liu, S. Xu, and S.-W. Yong, "An ultra-wideband out-of-phase power divider based on odd-mode spoof surface plasmon polariton," *Int. J. RF Microw. Comput.-Aided Eng.*, vol. 31, Article ID e22583, 2021.

[20] A. R. Moznebi, K. Afrooz, and A. Arsanjani, "Broadband bandpass filter and filtering power divider with enhanced slow-wave effect, compact size, and wide stopband based on butterfly-shaped spoof SPPs," *AEU Int. J. Electron. Commun.*, vol. 145, Article ID 154084, 2022.

[21] B. C. Pan, P. Yu, B. J. Guo, Y. F. Qiao, and G. Q. Luo, "Unequal bandpass filtering power divider based on hybrid HMSIW-SSPP modes," *Front. Phys.*, vol. 10, Article ID 851150, 2022.

[22] A. R. Moznebi and K. Afrooz, "Bandwidth enhancement of a half-mode substrate integrated waveguide filtering power divider using spoof surface plasmon polariton," *J. Phys. D: Appl. Phys.*, vol. 55, Article ID 025103, 2022.

[23] B. C. Pan, P. Yu, Z. Liao, F. Zhu, and G. Q. Luo, "A compact filtering power divider based on spoof surface plasmon polaritons and substrate integrated waveguide," *IEEE Microw. Wireless Compon. Lett.*, vol. 32, pp. 311-314, 2022.

[24] M. Z. Du, Y. J. Feng, K. Chen, and J. M. Zhao, "Filtering microwave differential signals through odd-mode spoof surface plasmon polariton propagation," *J. Phys. D: Appl. Phys.*, vol. 53, Article ID 165105, 2020.

[25] Q. Liu, J. Wang, L. Zhu, G. Zhang, and W. Wu, "Design of a new balanced-to-balanced filtering power divider based on square patch resonator," *IEEE Trans. Microw. Theory Techn.*, vol. 66, pp. 5280-5289, 2018.

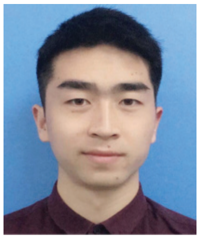

Yi Song received the B.S. degree in communication engineering and the M.S. degree in communication and information system from East China Jiaotong University, Nanchang, China, in 2015 and 2018, respectively. He is currently pursuing the Ph.D. degree in electromagnetic field and microwave technology at Xi'an Jiaotong University, Xi'an, China. His current research interests include microwave passive components.

Anxue Zhang received the B.S. degree in electrical engineering from Henan Normal University, in 1996, and the M.S. and Ph.D. degrees in electromagnetic and microwave engineering from Xi'an Jiaotong University, in 1999 and 2003, respectively. He is currently a professor with Xi'an Jiaotong University. His main research fields include metamaterials, RF and microwave circuit design, antennas, and electromagnetic wave propagation.

Residual Flux Measurement of Single-phase Transformers based on Equivalent Resistance

Qingkun Wang[1,2], Yuzhan Ren[1,2], Youhua Wang[1,2], Chengcheng Liu[1,2], and Shipu Wu[1,2]

[1]State Key Laboratory of Reliability and Intelligence of Electrical Equipment
Hebei University of Technology, Tianjin, 300130, China
wqk1501179683@163.com, 1094500481@qq.com

[2]Key Laboratory of Electromagnetic Field and Electrical Apparatus Reliability of Hebei Province
Hebei University of Technology, Tianjin, 300130, China
wangyi@hebut.edu.cn, 2016020@hebut.edu.cn, 601762376@qq.com

Abstract **–** Due to the presence of transformer residual flux, the magnetic flux of the core rapidly reaches saturation, thus causing an inrush current when the no-load transformer is directly connected to the grid, which affects the safe operation of the grid. Therefore, it is necessary to study the residual flux in the core to reduce the inrush current. However, the residual flux estimation has a large error. In this paper, a method is proposed to measure the residual flux of the transformer core by solving equivalent resistance and determining the direction of residual flux by the difference between the forward and reverse transient currents. In addition, the relationship between residual flux and equivalent resistance is established, and the empirical formula is obtained for calculating the residual flux. To evaluate the effectiveness of the proposed method, the residual flux of the square core is measured on the constructed experimental platform. Compared with the experimental results, the relative error of the residual flux of the core calculated by the proposed method is within 6%, which has higher accuracy and provides a reference for residual flux estimation.

Index Terms **–** Equivalent resistance, field-coupled equivalent circuit, residual flux measurement, transformer.

I. INTRODUCTION

The power transformer is an important part of the modern power system, and the working condition of the transformer is directly related to the operation quality of the power grid. The silicon steel sheet used in the transformer core is a ferromagnetic material, and its unique hysteresis generates residual flux, which will not disappear easily once it is generated. When the transformer is closed at no load, it is easy to cause magnetic saturation inside the core under the joint action of steady-state periodic component, transient bias, and residual flux. The generated inrush current transient values can reach up to several times the no-load current, which can cause transformer winding deformation or current imbalance; or it can lead to incorrect operation of relay protection devices and loss of protection of the transformer [1, 2]. In addition, due to the presence of residual flux, the voltage waveform will be distorted and second harmonics will be generated on the grid, affecting the power quality in the power system and causing great damage to the power electronics in the power system [3]. In engineering practice, residual flux measurement has been a pressing problem. The residual flux is difficult to measure directly in the closed core, so most measurement methods in recent years used the relationship between the residual flux and measurable parameters to indirectly obtain information about the residual flux. Faraday's law of electromagnetic induction calculates the residual flux in the transformer core by port voltage integration of power off, which requires a known value of the port voltage of power off [4, 5]. The fluxgate sensor is used to calculate the residual flux value based on the leakage flux, and the measurement results are easily affected by the measurement accuracy of the sensor itself and the installation location [6]. Similarly, the first peak value of the inrush current is used to explore the residual flux change of the transformer, which makes it difficult to directly determine the magnitude of the residual flux [7]. Meanwhile, the minor hysteresis loop is used to determine the residual flux of the transformer. Since the area enclosed by the minor hysteresis loop is indicated as the residual energy, it is unable to represent the direction of the residual flux. Then the charge (a variable) needs to be introduced to determine the direction of the residual flux, which will lead to more calculation errors [8]. In addition, there are two measurement methods, one of which

Submitted On: March 24, 2023
Accepted On: August 30, 2023

https://doi.org/10.13052/2023.ACES.J.380710

1054-4887 © ACES

is calculated by the relationship between the residual flux and current-related parameters [9–11], and the other is an iterative calculation of the dynamic hysteresis model, which has a more complex calculation process [12]. The use of magnetizing inductance to calculate the residual flux in the transformer core is likely to produce large computational errors due to the many external factors affecting the magnetizing inductance, which makes the fitting of the empirical formula difficult [13].

Considering the deficiencies of the existing measurement methods, a method is proposed to calculate the residual flux of the core by solving equivalent resistance and determining the direction of residual flux by the difference between forward and reverse transient currents. Specifically, a small DC signal excitation is applied to measure the current in the transient process. Meanwhile, the equivalent resistance is calculated in the field-coupled equivalent circuit through the measured transient current. Moreover, the relationship between residual flux and equivalent resistance is established. The empirical formulas of each are then used to calculate the residual flux from the equivalent resistance. Finally, the experimental test platform is built to verify the feasibility of the proposed method. The experimental results show that the proposed method has higher accuracy and provides a reference for residual flux estimation.

II. PRINCIPLE OF RESIDUAL FLUX MEASUREMENT

A. Principle of residual flux generation

Most of the ferromagnetic materials used in power transformers are silicon steel sheets, which consist of numerous magnetic domain structures. They can be spontaneously magnetized in microscopic domains, forming tiny magnetic dipoles. The motion of magnetic domains and domain walls has a significant effect on the hysteresis lines and magnetization curves. The magnetization process is divided into domain wall motion and domain rotation motion, shown in Fig. 1. During the magnetization process, if there is no external magnetic field (point O) in Fig. 2, the internal arrangement of magnetic domains is disordered and the magnetic material does not exhibit magnetic properties externally. The magnetic domain starts to move with domain wall displacement and domain rotation in the direction of the applied external magnetic field when the magnetic field is applied. The magnetic domains occur in reversible domain wall displacement motion when the applied magnetic field is small (O-a). If the magnetic field is removed, the domains will return to the starting magnetization state without hysteresis. When the magnetic field is further enhanced, the magnetization process will reach the next state (a-b), and the domain wall motion turns into an irreversible process, accompanied by a little rotational magnetization. If the magnetic field is removed at this time, the domain wall has reached a new position, the material is still partially magnetized and the magnetic domains are not returned to their initial state. This discontinuous and irregular motion is accompanied by the generation of maximum permeability due to the displacement of the domain walls jumping from one position to another. Meanwhile, noise is generated, which is called "Barkhausen noise." The saturation stage is reached when the applied magnetic field (b-c) increases continuously, the domain wall motion disappears, and the domains are aligned in the same direction as the applied magnetic field. When the magnetization intensity decreases to zero (point d), the magnetic domains and domain walls exhibit the residual flux density because they are unable to fully recover the state before they were magnetized. The hysteresis phenomenon of ferromagnetic materials leads to the residual flux in the core of the power transformer [14].

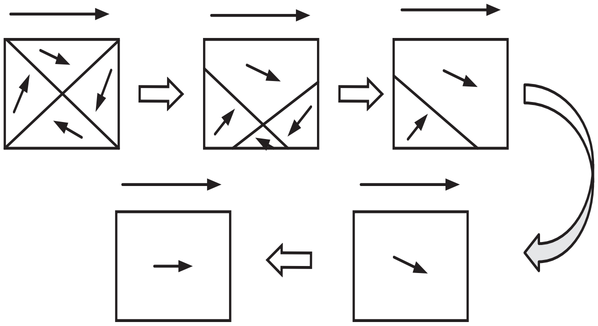

Fig. 1. Structural changes of magnetic domains during magnetization of ferromagnetic materials.

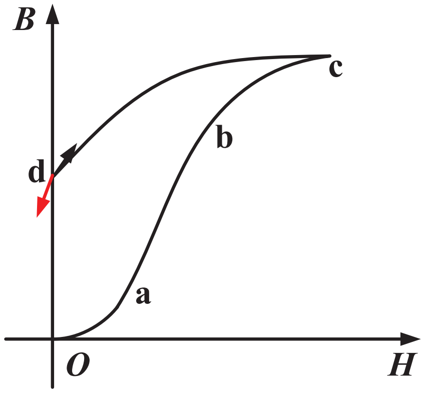

Fig. 2. Hysteresis curve of magnetic material in the transformer core.

B. Forward and reverse current obtainment

Current is obtained by applying a DC voltage of equal amplitude and opposite direction to the transformer winding. When DC excitation is applied to the core, the leakage flux of the transformer is about 0.15% of the flux during no-load operation, as the permeability of the core silicon steel material is much larger than the air gap permeability. Therefore, the influence of the leakage flux is negligible due to the largest proportion of the main flux. According to the field-coupled equivalent circuit of Fig. 3, the difficult and hard-to-measure magnetic field problem is transformed into a circuit problem [15]. In Fig. 2, the external excitation promotes the magnetization of the core when the DC voltage excitation in the direction of the black arrow is applied. The core is demagnetized when the DC voltage excitation in the direction of the red arrow is applied. Figure 4 shows the significant difference between the forward and reverse currents due to the hysteresis characteristics of the ferromagnetic material. In this case, the current indicated by the faster-changing solid line is the forward excitation current, and the slower-changing dashed line is the reverse excitation current. Therefore, the direction of the residual flux density can be determined by the transient process before reaching the steady state.

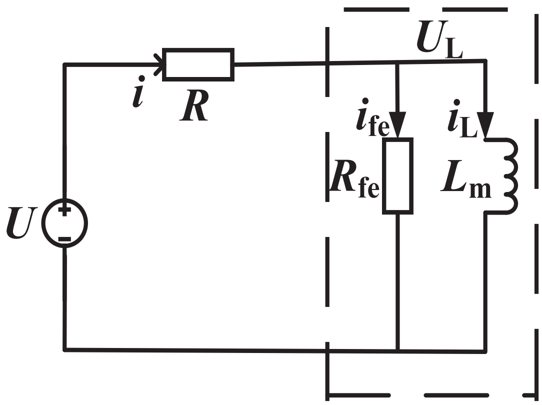

Fig. 3. The equivalent circuit inside the core in the transient process.

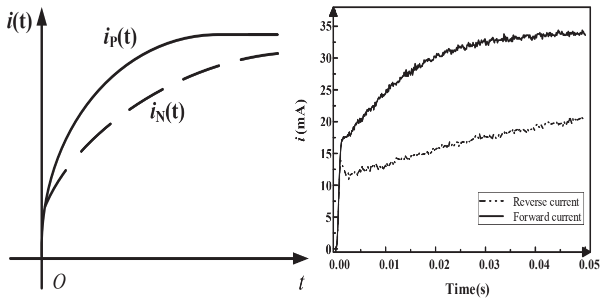

(a) (b)

Fig. 4. Transient current diagram: (a) forward and reverse transient current, (b) forward and reverse currents of residual flux at -624 mT.

C. Equivalent resistance calculation

The measured transient currents are post-processed to obtain the relationship between the residual flux density and the equivalent resistance in the field-coupled equivalent circuit. The core is internally equivalent to the resistance and magnetized inductance, and the magnetization process is reflected using the relative differential permeability, which is defined asμ_{rd}, where

$$\mu_{\mathrm{rd}} = \frac{1}{\mu_0}\frac{dB}{dH}. \tag{1}$$

In the process of establishing the magnetic field, the magnetizing inductance of the transformer is calculated by the equation

$$L_{\mathrm{m}} = \frac{N^2 S \mu_0 \mu_{\mathrm{rd}}}{l_{\mathrm{m}}}, \tag{2}$$

where N is the number of turns of the transformer winding, S is the cross-sectional area of the core, l_m is the effective magnetic circuit length, μ_0 is the air permeability, and μ_{rd} is the relative differential permeability of the core material. The Kirchhoff equation is written for the circuit shown in Fig. 3:

$$U = Ri + L_{\mathrm{m}}\frac{di_{\mathrm{L}}}{dt}, \tag{3}$$

$$U_L = L_{\mathrm{m}}\frac{di_{\mathrm{L}}}{dt}, \tag{4}$$

$$i(t) = \left(\frac{U}{R+R_{\mathrm{fe}}} - \frac{U}{R}\right)e^{-\frac{RR_{\mathrm{fe}}}{L_{\mathrm{m}}(R+R_{\mathrm{fe}})}t} + \frac{U}{R}, \tag{5}$$

where R is the series external resistance and R_{fe} is the equivalent resistance of the field-coupled circuit, L_m, is the magnetizing inductance, i_{fe}, is the current flowing through the equivalent resistance, i_L, is the current flowing through the magnetized inductance, *I,* is the current in the external circuit, U_L is the voltage across the magnetized inductance, and U is the applied DC signal voltage excitation.

As the magnetic flux in the core changes, the equivalent resistance in the core exhibits different characteristics, since the equivalent circuit resistance parameters are determined based on the characteristic parameters of the port current. When a DC voltage excitation is applied to the winding, the transient process value varies with the current [16]. After applying different directions of DC voltage excitation, in the same direction as the residual flux, excitation promotes the magnetization of the core, and reverse excitation demagnetizes. the core. The difference in the equivalent resistance between both is significant.

The change of the forward current is significantly faster than the change of the reverse current after applying DC voltage excitation, due to the difference in the equivalent resistance. Eventually, both reach a steady state, as shown in Fig. 4 (a), and Fig. 4 (b) shows the forward and reverse currents when the residual flux in the transformer core is -624 mT during the experiment.

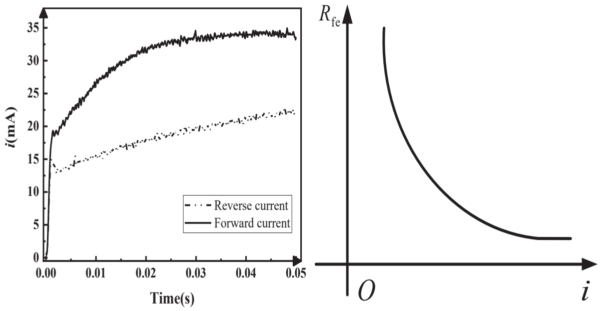

(a) (b)

Fig. 5. (a) Forward and reverse currents of residual flux at 791mT, (b) variation curve of equivalent resistance with measured current.

Due to the nonlinear variation of the equivalent resistance, the transient current is varied with different cases of the core flux, and both interact with each other in Fig. 5 (a). Figure 5 (b) shows that as the current increases, the equivalent resistance decreases and eventually tends to a stable value, so there is an obvious inflection point in the variation of the equivalent resistance. Then, to facilitate the determination of the direction of the residual flux density, a forward and reverse voltage excitation is applied to the transformer winding. Under the same residual flux, the applied forward voltage acts as a magnetizing effect on the residual flux of the core, while the applied reverse voltage acts as a demagnetizing effect. Immediately after employing the equivalent resistance calculated by the forward current, the relationship between the equivalent resistance and the residual flux density can be built, and the empirical equation for both can be fitted.

III. SIMULATION CALCULATION ANALYSIS

A. Parameter analysis

The selection of the appropriate DC voltage excitation and energizing time is particularly important. The measurement process is based on the principle of facilitating the measurement of transient processes and not causing changes in the residual flux density in the core. It is ensured that the applied excitation is within the permissible limits for the core for different residual flux cases.

According to Ampere's circuital theorem, the field intensity corresponding to the positive current in the measurement process is H_1 and the negative current is H_2. When the applied voltage excitation produces a field intensity less than H_1 or H_2, the transient current change is not obvious, and it is not possible to determine the direction of residual flux. Hence, the minimum value of H should be greater than the maximum value of both, and $H_{min} > \max(H_1, H_2)$. Thus the minimum voltage applied is

$$U_{\min} = \frac{H_{\min} R l}{N}, \tag{6}$$

where R is the series resistance, l is the average magnetic circuit length, and N is the number of turns of the measurement winding. Moreover, measured flux with no more than 10% of the minimum residual flux is used as a reference to determine the maximum value of applied DC excitation,

$$U_{\max} = \frac{0.1 H_{\mathrm{c}} R l}{N}. \tag{7}$$

In summary, the selection range of voltage excitation is

$$\frac{H_{\min} R l}{N} < U < \frac{0.1 H_{\mathrm{c}} R l}{N}, \tag{8}$$

where H_c is the coercive force of the material.

In the finite element calculation, it is found that the transient current has reached the steady state when the energizing time reaches 50 ms, while too much time will demagnetize the negative residual flux in the transformer core. Finally, the measurement process was designed with an energization time of 50 ms and a DC voltage excitation of 0.15 V.

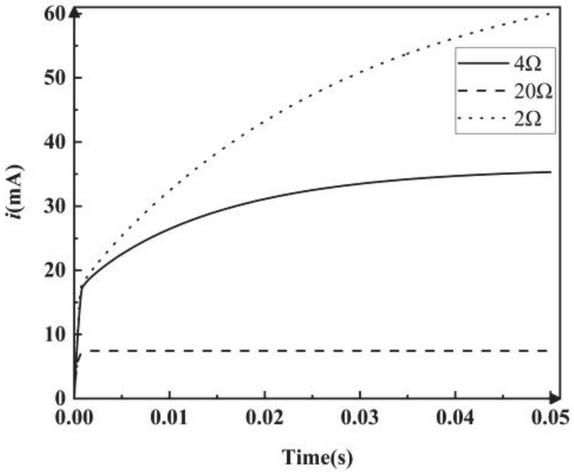

Fig. 6. Transient current under different series resistance.

In the measurement circuits, the magnitude of the current and the time to reach the steady state is more heavily affected by the external series resistance [17]. Therefore, it is necessary to select a suitable series resistance to meet the measurement requirements. Figure 6 shows that when the series resistance is 20 Ω, the value of the current to reach the steady state is small and changes rapidly, which is not conducive to recording the transient process. When the series resistance is 2 Ω, the current has not reached the steady state in 50 ms. Since the series resistor can also play a role in protecting the circuit, the resistance value cannot be chosen too small.

Table 1: Core and circuit parameters

Circuit and Core Parameters	Value
Core material	B30P105
Average magnetic circuit length of the core	1.92 m
Cross-sectional area of the iron core	0.0016 m^2
Density of silicon steel sheets	7.65×10^3 kg/m^3
Square core quality	24 kg
Core saturation magnetic density	1.8 T
Circuit external resistance	4 Ω
Measurement of winding turns	50
Measurement time	50 ms

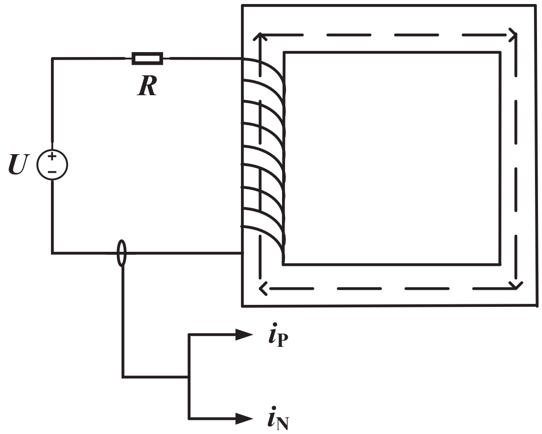

Fig. 7. Schematic diagram of the measurement circuit.

When the 4 Ω resistance is connected in series, the transient process is obvious to record, and the circuit will not be burned due to the small resistance. Finally, for the convenience of analysis and calculation, a series resistance of 4 Ω was chosen.

Based on the design criteria for transformer cores, square cores are used to study transformer cores. The transient characteristics of the equivalent resistance of the transformer core for different residual flux cases are studied. The square core is B30P105 cold-rolled oriented silicon steel sheet, and the model parameters are shown in Table 1. The theoretical saturation magnetic density of the selected B30P105 material is 1.8 T, and the residual flux is generally 0.36 T ~ 1.26 T. According to the measurement theory shown in Fig. 7, the finite element (FEM) calculations in Fig. 8 are performed after selecting the appropriate relevant parameters [18], and the material parameters used in the FEM calculations are derived from the measurements of the constructed experimental platform.

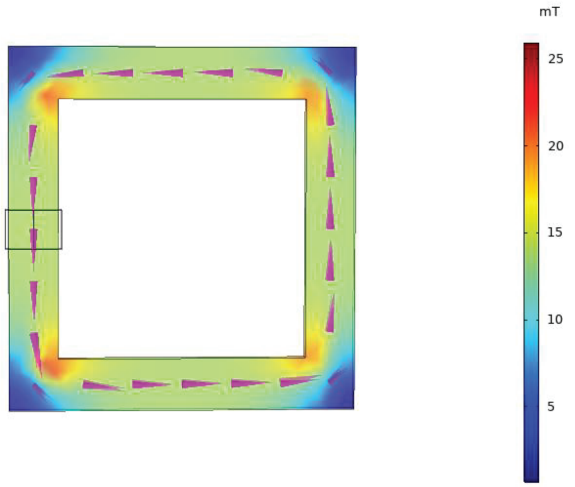

Fig. 8. Finite element calculation model for the square iron core.

It is essential to establish the relationship between B_r and core material properties to accurately simulate the core under different B_r in finite element calculations. By analyzing the magnetization process in the presence of B_r in the core, the flux density B and the magnetic field intensity H are processed linearly, and the relationship between B and H can be described by the following equation:

$$B(H)=\begin{cases}0.86\times10^{-3}H, & 0<H\le 0.45\\ kH-(k-0.86\times10^{-3})H, & H>0.45\end{cases}, \tag{9}$$

where k is related to the residual flux density.

B. The relationship between residual flux and equivalent resistance

For different cases of residual flux in the transformer core, a connection exists between the current and the equivalent resistance, as shown in Fig. 9.

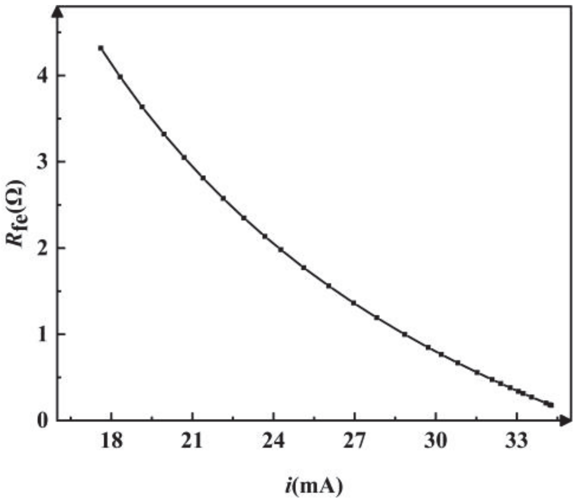

Fig. 9. Variation of equivalent resistance with the current.

The forward and reverse DC voltage excitation of 0.15 V is applied to the primary winding successively, and the direction of the residual flux can be determined by showing that the rate of change of the positive current is greater than that of the negative current, as shown in Fig. 10 (a). The forward current at different residual flux densities is selected, as shown in Fig. 10 (b), and the difference in transient currents exists due to different residual fluxes. The corresponding equivalent resistance is calculated from the forward current to facilitate further calculations of the residual flux, as shown in Fig. 11.

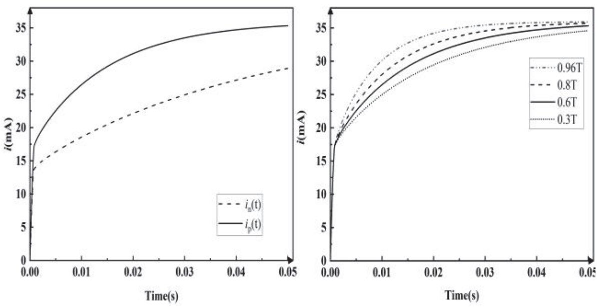

(a) (b)

Fig. 10. Calculation of current: (a) comparison of forward and reverse currents at a residual flux density of 0.6 T, (b) comparison of currents under different residual fluxes.

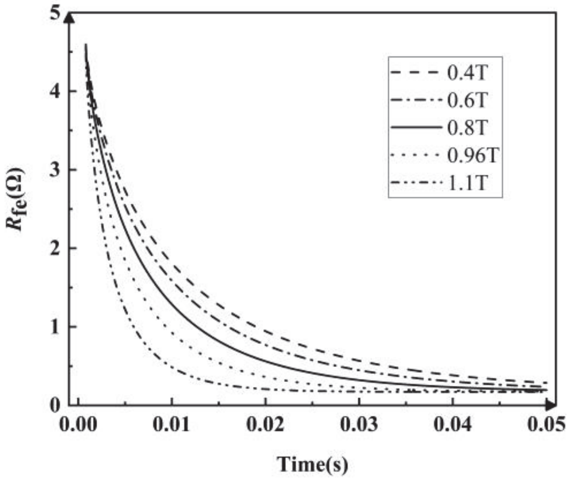

Fig. 11. Variation of equivalent resistance at different residual fluxes.

The direction of the residual flux can be obtained from the analysis of the forward and reverse currents; further, quantitative analysis of the residual flux value can be realized through the equivalent resistance. The equivalent resistance value varies significantly with the change in residual flux (see Fig. 11). Moreover, the polynomial interpolation method was chosen to fit the curve to the calculated discrete points at the inflection point of the equivalent resistance curve. Figure 12 shows that the discrete points were fitted better by three polynomial interpolations, with a residual sum of squares of 0.00075 and an adjusted R-squared of 0.99848, The empirical formula is fitted by

$$B_{\mathrm{r}} = -0.309 R_{\mathrm{fe}}{}^{3} + 0.494 R_{\mathrm{fe}}{}^{2} - 0.839 R_{\mathrm{fe}} + 1.319. \quad (10)$$

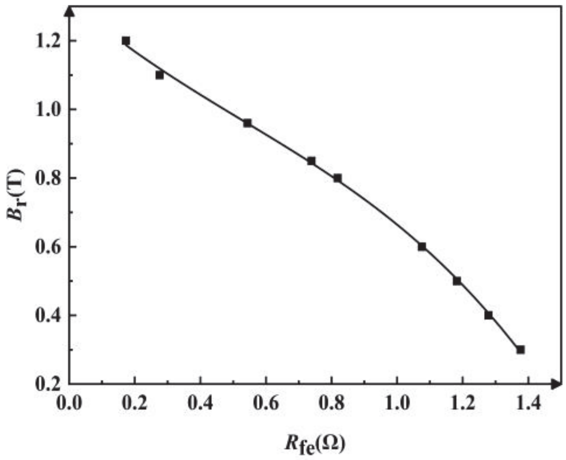

Fig. 12. Empirical formula curve fitting for discrete points.

IV. EXPERIMENTAL MEASUREMENTS AND ANALYSIS OF RESULTS

A. Residual flux preset

To simulate the case of unknown residual flux in engineering, the residual flux of the square core needs to be preset to facilitate comparison with the calculated residual flux. In addition, the core needs to be demagnetized before presetting the residual flux, considering the influence of external conditions to which the core is exposed. During the presetting process, the core is charged with different proportions of saturation flux as a residual flux by DC magnetization, and the applied DC voltage excitation is withdrawn. When the flux density in the core does not change with time, the stable value is recorded as the preset residual flux at this time.

An experimental measurement was performed to verify the feasibility and accuracy of the proposed method by using the experimental measurement platform, as shown in Fig. 13. A signal generator (WF1974) was used to generate the required DC voltage excitation during the experiments and was transmitted to the primary winding of the square core through a power amplifier, and data acquisition was performed using a current probe (N2782B). An oscilloscope (DSOX6004A) was

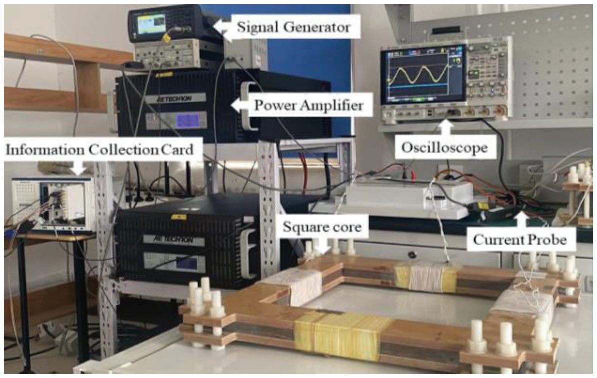

Fig. 13. Experimental measuring devices and square core.

used to record the transient current data, and a flux meter (Flux-meter480) was connected to the secondary winding during the experiments to facilitate the recording of the residual flux variation of the core.

B. Measurement results and analysis

The residual flux of the square core is measured by the experimental platform. The measurement system and the transmission system generate random errors and random noise, so noise effects are inevitable during the experiments. The measured transient currents are filtered using the moving average filter method. Figure 14 (a) compares the current finite element calculations of the residual flux of the core with the experimentally measured current values. It can be seen that the calculated values are similar to the experimentally measured values, so the calculated equivalent resistance values in Fig. 14 (b) are more accurate.

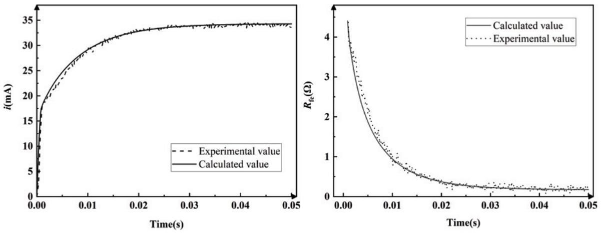

Fig. 14. Comparison of experimental measurements and calculations: (a) calculated and experimental transient current, (b) calculated with an experimental equivalent resistance.

The fitted empirical formula is employed for the residual flux calculation and compared with the presetting value. The error rate is defined as

$$\varepsilon = \left| \frac{B_{\mathrm{rc}} - B_{\mathrm{r}}}{B_{\mathrm{r}}} \right| \times 100\%, \tag{11}$$

where B_{rc} is the calculated residual flux value, and B_r is the experimental preset residual flux value. Therefore, the reliability of the measurement method is checked by the error rate.

Table 2: Relative error between experimental and calculated values

$B_{\mathbf{r}}$(mT)	$R_{\mathbf{fe}}(\Omega)$	$B_{\mathbf{rc}}$(mT)	ε(%)
489	1.22	467.89	4.32
624	1.08	598.61	4.07
714	0.98	679.44	4.84
791	0.89	745.01	5.81
915	0.57	943.78	3.10
954	0.51	978.41	2.56

Table 2 shows the residual flux value and the error based on the calculated and experimental values. The maximum error occurred at 791 mT and the error rate of 5.81%, while the minimum error of 2.56% occurred at 954 mT. Considering the influence of many factors such as measurement equipment, surrounding external environment, and data post-processing, the measurement error is less than 10%, which can meet the requirement.

V. CONCLUSION

This paper is based on the electromagnetic transient process of the core magnetic material after applying DC voltage excitation, by measuring the forward and reverse currents for different residual flux density cases. The forward current is selected as the target, and the corresponding equivalent resistance is calculated in the field-coupled equivalent circuit. Then, the relationship between the equivalent resistance and the residual flux is established, and the empirical equation for calculation is obtained. Finally, the method is verified by establishing an experimental test platform, and if the measurement results show that the relative error of the measured residual flux in the core is within 6%, the residual flux in the transformer core can be measured accurately. The advantage of the method is that it does not require the known state of the transformer before the power outage and has high measurement accuracy while meeting practical engineering requirements. Therefore, the method provides a reference for the estimation of residual flux.

REFERENCES

[1] C. Chuanjiang, F. Chun-en, X. Yang, L. Wei, Z. Bi-de, and R. Xiao, "Experimental study on controlled unloaded transformer switching considering residual flux"' *2017 4th International Conference on Electric Power Equipment - Switching Technology (ICEPE-ST)*, Xi'an, China, 2017.

[2] W. S. Fonseca, D. S. Lima, A. K. F. Lima, M. V. A. Nunes, U. H. Bezerra, and N. S. Soeiro, "Analysis of Structural Behavior of Transformer's Winding

Under Inrush Current Conditions," *IEEE Transactions on Industry Applications*, vol. 54, no. 3, pp. 2285-2294, May-June 2018.

[3] E. Cardelli, A. Faba, and F. Tissi, "Prediction and Control of Transformer Inrush Currents," *IEEE Transactions on Magnetics*, vol. 51, no. 3, pp. 1-4, March 2015.

[4] W. Yuan, H. Zhang, Y. Shangguan, J. Zou, and J. Yuan, "Analysis on method of calculating transformer residual flux by using the integration of port-voltage waveform and its implementation," *2017 20th International Conference on Electrical Machines and Systems (ICEMS)*, Sydney, NSW, Australia, 2017.

[5] K. Wang, G. Li, and S. Zhang, "Research on residual flux characteristics of transformer with single-phase four-limb core under different dc excitation current," *2020 IEEE International Conference on High Voltage Engineering and Application (ICHVE)*, Beijing, China, 2020.

[6] D. Cavallera, V. Oiring, J.-L. Coulomb, O. Chadebec, B. Caillault, and F. Zgainski, "A new method to evaluate residual flux thanks to leakage flux, application to a transformer," *IEEE Transactions on Magnetics*, vol. 50, no. 2, pp. 1005-1008, Feb. 2014.

[7] T. Peng, D. Wan, M. Zhao, H. Zhou, L. Mao, and X. Duan, "An indirect method for measuring transformer residual magnetism," *2019 IEEE 3rd Conference on Energy Internet and Energy System Integration (EI2)*, Changsha, China, pp. 1084-1087, 2019.

[8] D. Vulin, K. Milicevic, I. Biondic, and G. Petrovic, "Determining the residual magnetic flux value of a single-phase transformer using a minor hysteresis loop," *IEEE Transactions on Power Delivery*, vol. 36, no. 4, pp. 2066-2074, Aug. 2021.

[9] C. Huo, Y. Wang, S. Wu, and C. Liu, "Research on residual flux density measurement for single-phase transformer core based on energy changes," *IEEE Transactions on Instrumentation and Measuremen*t, vol. 70, pp. 1-9, 2021.

[10] W. Ge, Y. Wang, Z. Zhao, X. Yang, and Y. Li, "Residual flux in the closed magnetic core of a power transformer," *IEEE Transactions on Applied Superconductivity*, vol. 24, no. 3, pp. 1-4, June 2014.

[11] S. Wu, Y. Ren, Y. Wang, C. Huo, and C. Liu, "Residual flux measurement of power transformer based on transient current difference," *IEEE Transactions on Magnetics*, vol. 58, no. 2, pp. 1-5, Feb. 2022.

[12] Y. Wang, Z. Liu, and H. Chen, "Research on residual flux prediction of the transformer," *IEEE Transactions on Magnetics*, vol. 53, no. 6, pp. 1-4, June 2017.

[13] C. Huo, Y. Wang, C. Liu, and G. Lei, "Study on the residual flux density measurement method for power transformer cores based on magnetising inductance," *IET Electric Power Applications*, vol. 16, no. 2, pp. 224-235, 2022.

[14] M. Ouili, R. Mehasni, M. Feliachi, H. Allag, H. Bouchekara, G. Berthiau, and M. Latreche, "Coupling of 3D analytical calculation and PSO for the identification of magnet parameters used in magnetic separation," *Applied Computational Electromagnetics Society (ACES) Journal,* pp. 1607-1615, 2019.

[15] E. Gomez, A. Gabaldón, A. Molina, and J. Roger-Folch, "Coupling 2D finite element models and circuit equations using a bottom-up methodology," *The Applied Computational Electromagnetics Society (ACES) Journal,* pp. 225-231, 2002.

[16] M. Jafarifar, B. Rezaeealam, and A. Mir, "A new approach for improving the load current characteristic of cascaded magnetic flux compression generator," *Applied Computational Electromagnetics Society (ACES) Journal,* vol. 34, no. 8, pp. 1134-1142, 2019.

[17] F. G. Montoya, F. D. León, F. Arrabal-Campos, and A. Alcayde, "determination of instantaneous powers from a novel time-domain parameter identification method of non-linear single-phase circuits," *IEEE Transactions on Power Delivery*, vol. 37, no. 5, pp. 3608-3619, Oct. 2022.

[18] J. Ge, H. H. Eldeeb, K. Liu, J. Kang, H. Zhao, and O. Mohammed,, "Optimal range of coupling coefficient of loosely coupled transformer considering system resistance," *Applied Computational Electromagnetics Society (ACES) Journal*, vol. 35, no. 11, pp. 1368-1369, Nov. 2020.

Qingkun Wang was born in Jining, Shandong, China, in 1998. He received a B.E. degree in electrical engineering from Binzhou University, Binzhou, China, in 2021. He is currently pursuing an M.E. degree in electrical engineering at the Hebei University of Technology, Tianjin, China. His current research interest is the measurement of the residual flux of the power transformer core.

Yuzhan Ren was born in Anhui, China, in 1997. He received a B.E. degree in electrical engineering from Northeast Electric Power University, Jilin, China, in 2019. He is currently pursuing a Ph.D. degree in electrical engineering from the Hebei University of Technology, Tianjin, China. His current research interests include measurement of the residual flux of power transformer cores and research on the inrush current of large power transformers.

Youhua Wang was born in Jiujiang, Jiangxi, China, in 1964. He received a B.E. degree from Xian Jiaotong University, Xian, China, in 1987, an M.E. degree from the Hebei University of Technology, Tianjin, China, in 1990, and a Ph.D. from Fuzhou University, Fuzhou, China, in 1994, all in electrical apparatus. He is currently a professor at the College of Electrical Engineering. His current research interests include measurement and modeling of properties of magnetic materials, numerical analysis of the electromagnetic field, and electromagnetic device design, analysis, and optimization.

Chengcheng Liu was born in Jiangsu, China, in 1988. He received a B.E. degree in automation engineering from Yangzhou University, Yangzhou, China, in 2010, and a Ph.D. degree in electrical engineering from the Hebei University of Technology, Tianjin, China, in 2016. He was a joint Ph.D. student supported by the Chinese scholarship council with the University of Technology, Sydney, NSW, Australia. He is currently an IEEE member and an associate professor at the Hebei University of Technology. His research interests include the design, analysis, control, and optimization of electromagnetic devices.

Shipu Wu was born in Shijiazhuang, Hebei, China, in 1995. He received a B.E. degree in electrical engineering from the Hebei University of Technology, Tianjin, China, in 2017. He is currently pursuing a Ph.D. degree in electrical engineering at the Hebei University of Technology, Tianjin, China. His current research interests include measurement of the residual flux of power transformer cores and research on the inrush current of large power transformers.